LOW ENERGY MAGNETO-OPTICS OF FRUSTRATED MAGNETISM

by

Xinshu Zhang

A dissertation submitted to The Johns Hopkins University in conformity with the requirements for the degree of Doctor of Philosophy.

Baltimore, Maryland

April, 2021

Abstract

Frustrated magnets are magnetic materials with localized spins that interact strongly through competing exchange interactions that cannot be satisfied simultaneously. As a result, the ground states of such systems are highly degenerate and the ordering temperature is substantially suppressed compared to conventional magnets. One renowned example of a frustrated magnet is a quantum spin liquid, where spins are highly correlated but keep fluctuating even down to a temperature of absolute zero. Quantum spin liquids exhibit remarkable phenomena, such as hosting fractionalized quasiparticles and can be thought of a spin counterpart of fractionalized quantum Hall states. The long range entanglement in quantum spin liquids may pave the way to realize quantum computation.

Frustrated magnetism has become an extremely active field in recent years. We use time domain terahertz spectroscopy to study various frustrated magnets, including quantum spin liquids and quantum spin ice. We measured spin wave excitations in $YbMgGaO_4$ in the field polarized regime and determine

ABSTRACT

the exchange constants accurately. Based on obtained exchange constants, we place this material in close proximity to the spin liquid regime in the phase diagram. We observed a broad continuum at the Γ point of $BaCo_2(AsO_4)_2$ which is consistent with predictions of the Kitaev model. We also observed a possible field induced quantum spin liquid state in $BaCo_2(AsO_4)_2$. This new synthesized cobalt based Kitaev spin liquid candidate deserves further investigations. We studied the field evolution of the low energy crystal field excitations in $Tb_2Ti_2O_7$ and our results suggest strong spin-lattice coupling in $Tb_2Ti_2O_7$, which may be relevant to stabilize quantum spin liquid states. We measured the one magnon and two magnon states as function of magnetic field in $Yb_2Ti_2O_7$. We found that the magnon decay occurs at low field, indicating strong fluctuation in this material despite its ferromagnetic nature. We demonstrate that time domain terahertz spectroscopy is a powerful tool to study frustrated magnets. Furthermore, when combined with other techniques such as neutron scattering and dc susceptibility, we are able to provide much more comprehensive information that can not be obtained by other techniques alone.

Primary Reader and Advisor: N. Peter Armitage

Secondary Reader: Natalia Drichko

Acknowledgments

As I grew up, I have been told many times that I should be more independent and should learn to do things by myself. This is what I was taught and it is indeed what I am trying to do. However, receiving Ph.D degree is not an easy task and no one can finish the graduate school without the help from others. In the six years of graduate school life, I received countless helps and supports and I would like to take this opportunity to express my gratitude.

First and foremost I want to thank my advisor Peter Armitage for leading and guiding me on the road of science. Peter is very kind and patient to me. Six years ago I first met Peter and when Peter was introducing his lab to me, I encountered one of the most common problems for Chinese graduate students, the language barrier. It was a little embarrassing that I showed a perplexed expression while Peter was passionately explaining some ”simple” physics. I thought Peter would be disappointed, but instead Peter rephrased it with a more understandable word for me. I still remember the two words ”elliptical” and ”oval”. I was attracted by Peter's nice personality and the in-

teresting physics you talked about. Peter is always happy to discuss with me, sharing ideas and the discussion sometimes even extends beyond original focus. I really enjoy discussing with you and learn how to think as a scientist. As an experimentalist, I need to know physics and also need to do practical operation on instruments. Until I met with Peter, I can't imagine a professor can be so familiar with the instrument and sometimes Peter even join us to repair broken equipments. Peter sets a standard on how to become a good physicist. Peter really cares about me. Due to the uncertainty in postdoc position and unfinished experiments, I could not graduate at the expected date. Instead of blaming me, Peter offered a few months extension and gave me the priority to use the instrument so that I can finish my project. I made an excellent choice six years ago to be your student. Thank you Peter for everything!

I would like to thank all group members I have overlapped with in Armitage's lab. They are Liang Wu, Nicholas Laurita, Bing Cheng, Mintu Mondal, Fahad Mahmood, Anaëlle Legros, Youcheng Wang, Dipanjan Chaudhuri, Prashant Chauhan, David Barbalas, Rishi Bhandia, Zhenisbek Tagay, Ralph Romero and Sirak Mekonen. Particularly, I want to thank Nick and Bing for teaching me how to do THz experiments and tune the THz system. I still keep in touch with Bing even if he already graduated and consult him on various things. Fahad taught me how to think critically and how to write a nice paper. Dipanjan and I came to the lab in the same year and we shared the office for

six years. Dipanjan not only gives me tremendous helps in physics but also builds a relaxing working environment. I am not a person who likes to chat, but I enjoyed chatting with you. So thank all the group members for making the lab productive and harmonious.

I would like to thank my collaborators who make this thesis possible. I thank Martin Mourigal, Haidong Zhou and Zhiling Dun for providing $YbMgGaO_4$ samples and sharing neutron data. I thank Seyed Koohpayeh, Robert Cava and Ruidan Zhong for growing many high-quality single crystals. I thank Jonathan Gaudet, Yi Luo and Tom Halloran on analysis and experiments on $Tb_2Ti_2O_7$. Yi Luo made tremendous contributions to the crystal field calculations on the $Tb_2Ti_2O_7$ project. I thank Natalia Drichko and Yuanyuan Xu for helping me Raman scattering measurements. I thank Steffen Säubert and Christian Pfleiderer on dc susceptibility measurements. And special thanks to Collin Broholm for many helpful discussions on my projects. Thank Natalia for reading my thesis and giving helpful feedbacks.

I also want to thank department administrators Kelley Key and Pam Carmen. I thank Oleg Tchernyshyov, Yi Li and Chia-Ling Chien for teaching nice courses. I thank Reid Mumford for helping me on TA stuffs. I also want to thank my friend Youzhe Chen who enriches my daily life. We discuss physics at school and also play video games together in spare time.

Lastly, I want to thank my family. My mom Fei Yang always put me in

the first place among others. My mom got gastric carcinoma a few years ago and they didn't tell me this so that I could focus on study. It's a coincidence that I decided to go back to China and happened to catch up with her surgery. Luckily, the surgery was very successful and my mom has recovered pretty well. Your strong will and optimistic attitude inspired me and I wish I would not fear any problems in future. My dad Zhidong Zhang is a physicist as well. I admire your dedication and persistence. My dad likes to talk about physics with me and becomes even much happier than me when heard my progress on research. My girlfriend Chong Wang accompanied me on the other side of the world without regrets. Long distance relationship is hard, but we have confidence we can work this out. Hopefully the Covid-19 situation will turn better and she will come with me during my postdoc period. I love you all!

Dedication

This thesis is dedicated to my family for their unconditional love and support.

Contents

List of Tables

List of Figures

Chapter 1

Introduction to Frustrated Magnetism

1.1 Frustrated Magnetism

The first known description of magnetism can be traced back to 2500 years ago, when the mineral lodestone were discovered in ancient Greek and China, which are naturally magnetized pieces of iron ore. As one of the four great inventions in Chinese history, magnetic compass was first invented as early as the Chinese Han Dynasty and was later used in navigation. The 11th-century Chinese scientist Shen Kuo was the first person to record the magnetic needle compass in his “Dream Pool Essay” and showed it could improve the accuracy of navigation.

Ever since then, tremendous efforts have been devoted to studying magnetism. An understanding of the relationship between electricity and magnetism started in 1819 by Hans Christian Oersted, who discovered that an electric current could generate magnetic field. André Marie Ampère in 1820 related the integrated magnetic field around a closed loop to the electric current passing through the loop. Michael Faraday in 1831 found that a time-varying magnetic flux through a loop of wire induced a voltage. James Clerk Maxwell unified electricity, magnetism, and optics into the field of electromagnetism by Maxwell equation [36]. Now electromagnetism has continued to develop to quantum electrodynamics and finally the standard model.

Meanwhile, the magnetism in solids was also developed. The magnetic properties of materials are mainly due to the magnetic moments of the electrons (both orbit and intrinsic spin). If the electrons filled the sub-shell completely, there will be zero net magnetic moment because electrons are paired up with opposite magnetic moment as a result of Pauli exclusion principle. If there are unpaired electrons left over, in the presence of a magnetic field the magnetic moments align up to reinforce it, but the magnetic moment points to random direction once the magnetic field is removed, this is known as paramagnetism. On the other hand, in some materials the magnetic moments have tendency to align with their neighbors or anti-align with their neighbors below certain temperatures, known as ferromagnetism or anti-ferromagnetism,

respectively [37]. A quantitative way to describe magnetism is to use magnetic susceptibility, by definition $M = \chi H$ for linear materials, where M is magnetization, H is external magnetic field, χ is magnetic susceptibility. For paramagnets, Pierre Curie found $\chi = C/T$, where C is Curie constant and T is temperature. Curie's law says at high temperature, the magnetic susceptibility is inversely proportional to temperature and for a given temperature, the magnetization is proportional to external magnetic field. Later, Peter Weiss developed Curie Weise law for ferromagnets, $\chi = C/(T - \Theta_{CW})$, where Θ_{CW} is Curie temperature, at which the magnetic suscptibility diverges and below Θ_{CW} the ferromagnet has spontaneous symmetry breaking [38]. Θ_{CW} is related to the strength of interactions between magnetic moments. In ferromagnetic systems, Θ_{CW} is positive, while in antiferromagnetic systems, Θ_{CW} is negative, and a phase transition to an anti-ferromagnetically ordered state is expected at temperatures comparable to $|\Theta_{CW}|$ known as Néel tempeature T_N [39]. It seems most magnetic materials belong to previous categories. However, there exist some materials that break these rules and do not order even down to very low temperature due to frustration.

In real life, frustration makes people unhappy and frustration is a a little demon that everyone wishes to keep away. On the contrary, frustration makes the physics world colorful and vigorous. In physics, frustration refers to the presence of competing forces that cannot be simultaneously satisfied. This

concept can then be applied to magnetism and now frustrated magnetism has become one of the most active field in physics. Frustrated magnets are magnetic materials with localized spins interacting strongly through competing exchange interactions which cannot be satisfied simultaneously. As a result, the ground states of such systems are highly degenerate and the ordering temperature are substantially suppressed compared to unfrustrated case. Under certain conditions, this can lead to the formation of fluid-like states of matter, so-called spin liquids, in which the constituent spins are highly correlated but keep fluctuating even down to a temperature of absolute zero [4, 40].

Here, I will show a famous example on frustrated magnetism. Let's consider a 2 dimensional square lattice with anti-ferromagnetic interactions, which can only point up or down (Ising spins). To minimize the energy, the adjacent spins are aligned in opposite direction and all spins can satisfy this requirements, hence this system is unfrustrated. In contrast, the triangular lattice tells a totally different story. Suppose we have two spins aligned oppositely already, then the third spin does not know whether to point up or down since both configuration has the same energy, hence this system is frustrated. There are a few consequences of frustration. The ground state has a very large degeneracy and the ground state entropy is extensive. As shown by Wannier in 1950 that such system has ground-state entropy as large as $0.323 k_B N$, where k_B is the Boltzmann constant and N is the number of spins [41]. With such large

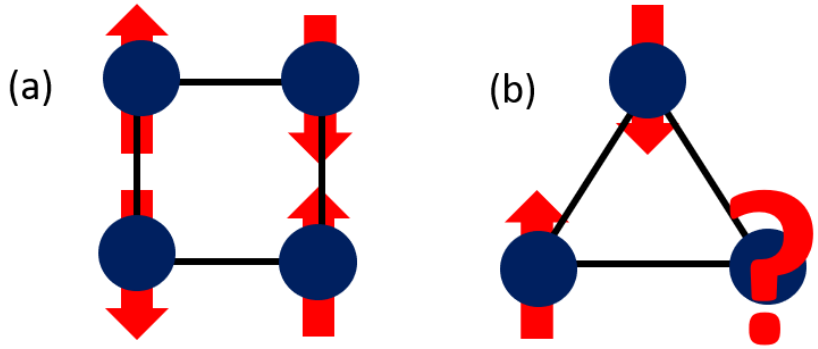

Figure 1.1: Example of geometric frustration. (a) 2 dimensional square lattice with anti-ferromagnetic interactions and (b) 2 dimensional triangular lattice with anti-ferromagnetic interactions.

degeneracy in ground state, the ordering temperature T_N is significantly reduced compared to $|\Theta_{CW}|$. A quantity $f = |\Theta_{CW}|/T_N$ is used to evaluate the frustration and by convention, a system is frustrated if f is greater than 10. Furthermore, with S = 1/2, the quantum mechanical uncertainty principle requires zero-point fluctuation persisting down to T = 0 K. Therefore, frustrated magnets are usually candidates to search for quantum spin liquids [42].

1.2 Quantum Spin Liquids

Matters can have different states, such as solid, liquid and gas. Understanding the states of matter is fundamentally important in condensed matter

physics. In 1940s, Lev Landau developed a general theory of phase transition, where phase transitions from one state to the other are associated with symmetry breaking and are characterized by order parameters [43, 44]. Landau theory is very successful and it seemed all phases of matter can be captured within this framework. However, this picture broke down in 1980s with the discovery of fractional quantum hall effect. With extremely low temperature and large magnetic field, the 2 dimensional electron gas condenses into a remarkable liquid state with exotic quasi-particles carrying a fractional elementary electron charge and it cannot be explained in terms of symmetry breaking, but instead it's characterized by topological order, which is properties of ground state wave function [45, 46]. Landau theory applies for system at finite temperatures where quantum effects can be ignored, therefore it's not surprising that Landau theory fails at zero temperature where quantum effects are dominating. Then it's natural to ask whether analogous phenomena can occur for spin system. The answer is YES! Actually, the concept of topological order was first introduced in the context of quantum spin liquid (QSL) by Xiaogang Wen [47].

Quantum spin liquids are exotic states where spins are highly correlated but remain dynamic even down to a temperature of absolute zero due to strong quantum fluctuation. In contrast to conventional magnetically ordered states, which break spin rotational symmetry, QSLs cannot be described by order parameter. Instead QSLs are characterized by topological order of a complex

ground state wave function with long-range quantum entanglement. Under smooth deformations, such wave function cannot transform to a product state wave function as in a magnetically ordered ground state. The fact that each spin degrees of freedom in the ordered state can be specified independently manifests the absence of essential quantum entanglement. Therefore, one of the key ingredients in QSLs is the long range entanglement [40, 48].

The consequences of long range entanglement in QSLs are fractionalized quasi-particles and emergent gauge field. A typical fractional quasi-particle is a spinon with spin 1/2 in contrast to conventional magnons with integer spin. Spinons are deconfined and can propagate freely under the emergent gauge field. Low energy effective theories with emergent gauge fields are prototypical framework to study and classify QSLs. There are many kinds of QSLs based on the gauge theory [49, 50]. However, for simplicity in this thesis I will introduce a few typical QSLs based on the lattice structures.

1.2.1 Quantum Spin Liquids in Triangular Lattice

Quantum spin liquids were first proposed by Philip Anderson in 1973 that the ground state of the spin 1/2 triangular lattice Heisenberg antiferromagnet might be a spin liquid [51]. It was later shown by Anderson the intimate

relationship between spin liquid and superconductor. It's possible to achieve superconductivity by doping a spin liquid, which is the parent compound of superconductor in the Mott insulator [52]. So in this section, I will start with the prototype spin liquid proposed by Anderson.

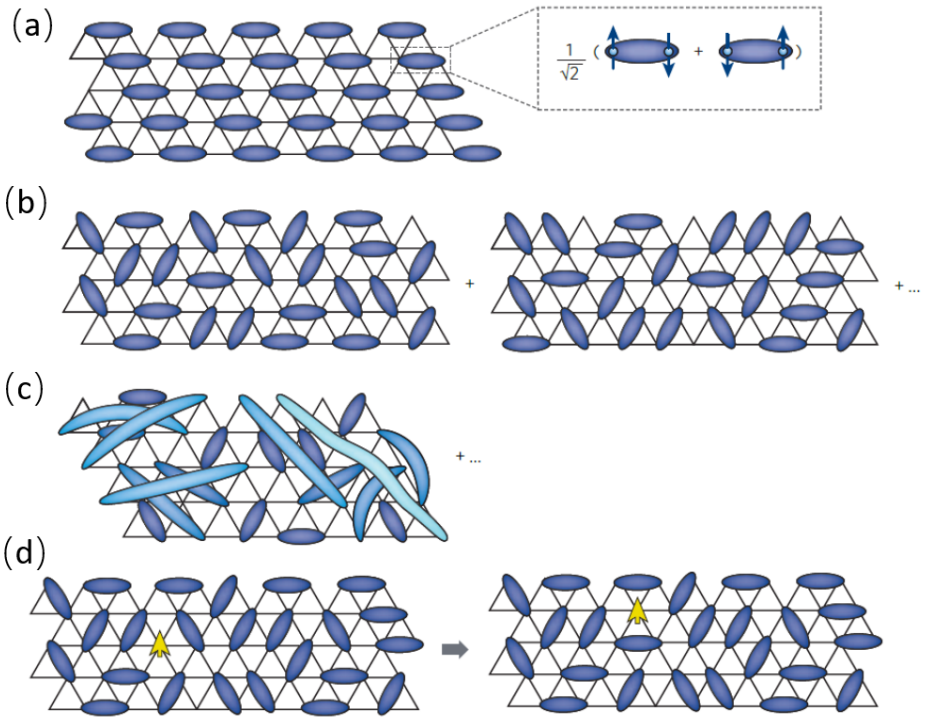

Figure 1.2: Example of geometric frustration. (a) Valence bond solid with spin singlet represented by blue oval. (b) Resonating valence bond spin liquid as superposition of various singlet arrangements. (c) Short range or long range singlet. (d) The spinon can be created and move freely. The figures are adopted from [4].

Since one feature of spin liquid is a lack of long range magnetic order, it's natural to consider a state, where two spins pair up to a singlet forming a static pattern. The ground state is a product of valence bonds and it is known

as valence bond solid as shown in Fig. 2.6 (a). Although the ground state is non-magnetic, it's not a spin liquid state as it lacks long range entanglement and it breaks lattice symmetry due to the fixed arrangement of valence bonds. To build a quantum spin liquid, the valence bonds need to resonate and the ground state should be a superposition of different configurations of different patterns as shown in Fig. 2.6 (b). Such state is known as resonating valence bond (RVB) state. There is no preference for any specific valence bond and this state can be regarded as a valence bond 'liquid' rather than a solid. The RVB spin liquid hosts exotic quaisi-particles called spinon, which can be created by breaking the signlet pairs. In most condensed matter systems, excitations can be constructed by elementary excitations that are either electron-like with spin 1/2 and charge e or magnon-like with spin 1 and charge neutral. Spinons are fractional neutral quasi-particles carrying spin 1/2. One way to understand spinons is to consider it as a fraction of electrons as a result of spin-charge separation. Alternatively, you can make an excitation in valence bond solid by breaking one of singlets to make a triplet, known as triplon, a gapped bosonic spin-one excitation. As this triplon are pulled apart, we will get two spinons. But the spinons are confined in valence bond solid because more energy is required if they are pulled further. In contrast, in the RVB spin liquid, once the spinons are created, they can move freely because the RVB spin liquid state is a superposition of infinite configurations and it can rearrange the configura-

tion at liberty. In addition, it turns out that the spins can pair up not only with nearest neighbours but also with spins far away. When the singlets are formed by two spins at long distances, the energy to break the singlets are extremely small compared to short ranged singlets and the excitations may be gapless.

1.2.2 Quantum Spin Liquids in Hexagonal Lattice

Although impressive progress has been made on RVB spin liquid state, research has been impeded by the fact that it can not be solved as an exact solution of any realistic model. A theoretical breakthrough in spin liquids was made in 2006 by Alexei Kitaev. Kitaev proposed a simple but novel model that is exactly solvable. Kitaev model shows a QSL ground state, where the spins fractionalize into emergent quasi-particles, well known as Majorana fermions [53].

The Kitaev model consists of S=1/2 spins on a honeycomb lattice with nearest neighbor ferromagnetic Ising interactions, which have bond dependence with easy axis along the x,y,z direction. The Kitaev spin Hamiltonian reads:

$$H_K = -J_K^x \sum_{<ij>_x} \sigma_i^x \sigma_j^x - J_K^y \sum_{<ij>_y} \sigma_i^y \sigma_j^y - J_K^z \sum_{<ij>_z} \sigma_i^z \sigma_j^z \tag{1.1}$$

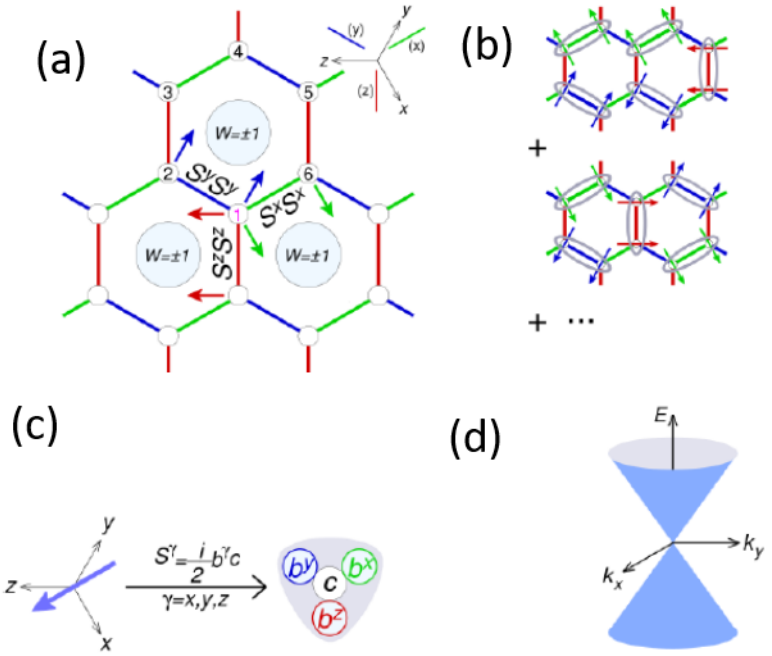

Figure 1.3: (a) The S=1/2 spins on a honeycomb lattice with bond dependent Ising interactions. Product of six spins around each hexagonal loop is W_p, corresponding to Z_2 flux. (b) The Kitaev spin liquid as superposition of various spin configurations. (c) A fractionalization of spin into localized and itinerant Majorana fermions. (d) Dirac dispersion of the itinerant Majorana fermion. Figures are adopted from [5].

where σ are Pauli matrices, and $< ij >_{x,y,z}$ denotes x, y, z bonds accordingly as shown in Fig.1.3. The orthogonal anisotropy of the three nearest-neighbor bonds at one site conflicts with each other, leading to strong magnetic frustrations and large ground state degeneracy. So it is already a good spin liquid candidate at the first glance.

Majoranas are fermions that are their own antiparticle that are hypothe-

sised by Ettore Majorana in 1937. Kitaev showed by introducing Majorana fermions, the Kitaev model can be solved exactly. By mathematically replacing the spin operator σ^α (α=x, y, z) with two types of Majorana operators b^α and c as σ^α=$ib^\alpha c$, the fractionalization of spins are employed, where b^α (α=x, y, z) presents the three localized Majorana fermions and c represents the one itinerant Majorana fermion with the constraint $b^x b^y b^z c$=1.Then the spin Hamiltonian can be simplified to

$$H_K = iJ_K^x \sum_{<ij>_x} u_{ij}^x c_i c_j + iJ_K^y \sum_{<ij>_y} u_{ij}^y c_i c_j + iJ_K^z \sum_{<ij>_z} u_{ij}^z c_i c_j \tag{1.2}$$

where u_{ij}^α=$ib_i^\alpha b_j^\alpha$ with eigenvalues ± 1 is called bond operator and it commutes with each other and with the Hamiltonian. In the Majorana representation, the Kitaev model can be transformed into a fermionic form with conservation law of the flux (loop) operator, which can be expressed by the bond operators through $W_p = u_{12}u_{23}u_{34}u_{45}u_{56}u_{61}$. Each plaquette therefore has a so called flux degree of freedom. These fluxes are similar to artificial magnetic field through the plaquette. A particle that moves in a loop around the plaquette picks up a phase ± 1 similar to Aharonov-Bohm effect with 0 or π. Because of commutation and conservation, b^α Majoranas are constrained to the corresponding bond and thus immobile, while c fermion can move through the honeycomb lattice coherently. The ground state can be shown to be a QSL and is described as

an ensemble of localized and itinerant Majorana fermions. The dispersion of the itinerant Majorana can be obtained by diagonalizing the quadratic (non-interacting) fermionic Hamiltonian. Depending on the coupling constants J_K, the excitations are either gapped or gapless as shown in Fig. 1.3. The gapped phase hosts abelian anyons, while the gapless phase acquires a gap in the presence of magnetic field and may host non-abelian anyons. Anyons have non-trivial statistics. As we all know, exchanging two indistinguishable particles, the observable remains the same, but the wave-function is changed up to a phase factor $e^{i\theta}$ with 1 for boson and -1 for fermion. However, in 2 dimension, the phase factor of exchanging particles can be other values than ± 1. Such particles are known as anyons. It was shown by Kitaev that braiding of non-abelian anyons can be used to realized quantum computation [54], hence the study of Kitaev spin liquid is on the subject of intense interests.

1.2.3 Quantum Spin Liquid in Pyrochlore Lattice

Having discussed the spin liquid in two dimension, it is time to extend dimensionality into 3 dimensions, particularly with pyrochlore lattice $A_2B_2O_7$, consisting of two interpenetrating lattices of corner sharing tetrahedra. A is usually a rare earth element with large magnetic moment and B is a non-

magnetic element, such as $Ho_2Ti_2O_7$ and $Dy_2Ti_2O_7$. With strong anisotropy due to crystal field, the magnetic moment on the corner is restricted to point either in or out of the tetrahedra. Such system is highly frustrated with ferromagnetic interactions and the spins fulfill a so called two-in-two-out ice rule [6,55]. Under the requirement of ice rule, each tetrahedron has six configurations with same minimal energy, leading to a large degeneracy in the ground state. Such a system is called spin ice given that this is analogous to common water ice. In water ice for each oxygen atom, two of the neighboring hydrogen atoms are close and they form the traditional O-H valence bond. On the other hand, two hydrogen atoms from neighboring water molecules are far away and they form the hydrogen bond. In 1935 Pauling pointed out that the number of configurations satisfying this "two-near, two-far" ice rule increases exponentially with the system size and the entropy at zero temperature was extensive. The residual entropy in both water ice and spin ice were later confirmed by specific heat measurements [56–58].

The two-in-two-out ice rules is an effective essential in spin ice and it has important consequences. In theory,spin ice is related to an effective Coulomb phases because spin vectors can be mapped to a divergence free artificial magnetic field with no sink or source in the tetrahedra. The spins do not order due to fluctuations and these fluctuations include long loops of flux that have spin correlations over long distances. This implies a power-law dipolar corre-

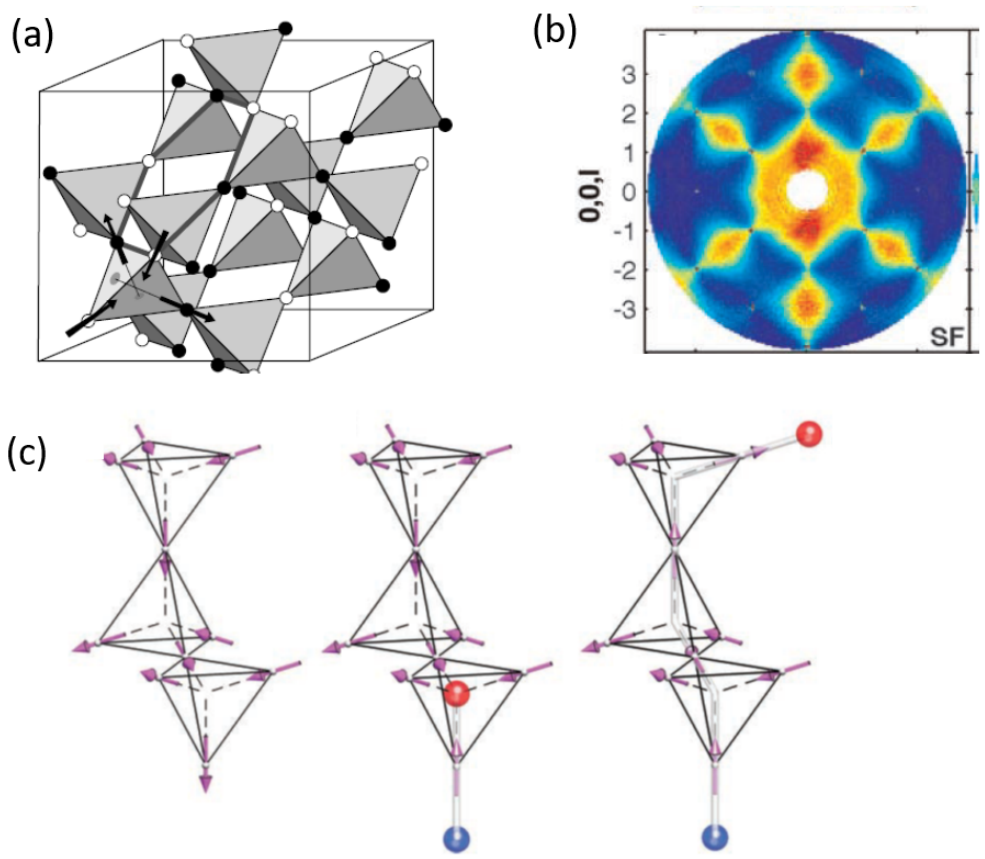

Figure 1.4: (a) Pyrochlore lattice of corner sharing tetrahedra along with 2 in 2 out ice rule (b) Pinch point signature of spin ice measured by neutron scattering (c) Magnetic monopole is created by flipping spin and can move apart further without energy cost. Figures are adopted from [6, 7].

lations that are anisotropic in spin space and decay as a power law$\sim 1/r^3$ in real space. Correlations in a paramagnet decay exponetially therefore, having power-law correlations without any broken symmetry is remarkable. After Fourier transformation of the spin correlation, the structure factor showing the so-called pinch points are obtained and can be visualized by neutron scattering in momentum space as shown in Fig. 1.4 (b) [7].

The analogy between spin ice and electromagnetism goes beyond the equilibrium spin correlations. One of the most remarkable aspects of spin ices is that of magnetic monopoles [59]. If the two-in-two-out ice rule is broken , there's either three-in-one-out or three out-one-in in one tetrahedron, as result the center of tetrahedron becomes a source or sink of flux. That is a magnetic monopole. Magnetic monopoles are non-local quasi-particles, which can move freely by flipping spins. Two magnetic monopoles are connected by a Dirac string as shown in Fig. 1.4 (c).

Typical spin ices possess very large magnetic moment with Ising interactions, but if the spin ice has S=1/2 with weak transverse interaction component, such system is called quantum spin ice, where the fluctuation and quantum effects are enhanced and it is a good candidate for quantum spin liquid.

1.3 Terahertz in frustrated magnets

In this thesis, I use time domain terahertz spectroscopy (TDTS) to study frustrated magnets, particularly quantum spin liquid. As a rising techniques employed in frustrated magnetism recently, TDTS showed its power and versatility in this field. I will show TDTS is a powerful tool for studying frustrated magnetism and is complementary to other techniques. Furthermore, combining TDTS and other technique enables us to understand this field these

materials in a novel fashion.

TDTS can detect the transition between magnetic states with different energy levels just like electron spin resonance (ESR). A free electron has a magnetic moment and spin 1/2 with magnetic components $m_s = \pm 1/2$. In the presence of an external magnetic field B, the spin aligns either parellel or antiparallel to the field, each alignment corresponding to a specific energy. The separation between the two energy levels is proportional to the magnetic field B, known as Zeeman effect: $E = g_e \mu_B B$, where $g_e = 2.0023$ is electron g factor and μ_B is Bohr magneton. The transition from lower energy level to higher energy level may be induced by a electromagnetic radiation if the photon energy $E = \hbar\nu$ is equal to the Zeeman energy.

Experimentally, ESR spectra can be generated by either varying the photon frequency (microwave range) on a sample while fixing the magnetic field as a constant or vice versa. In practice, the frequency is fixed with sweeping the magnetic field. By sweeping the external magnetic field, once the Zeeman energy gap is matching the photon energy as shown in Fig. 1.5, the unpaired electrons can hop from the low energy state to high energy state.Then the absorption of energy is monitored and converted into a spectrum. The absorption appears as a resonance peak in ESR or a dip in THz transmission measurements.

The above paragraph discussed the simplest case, where only the single spin

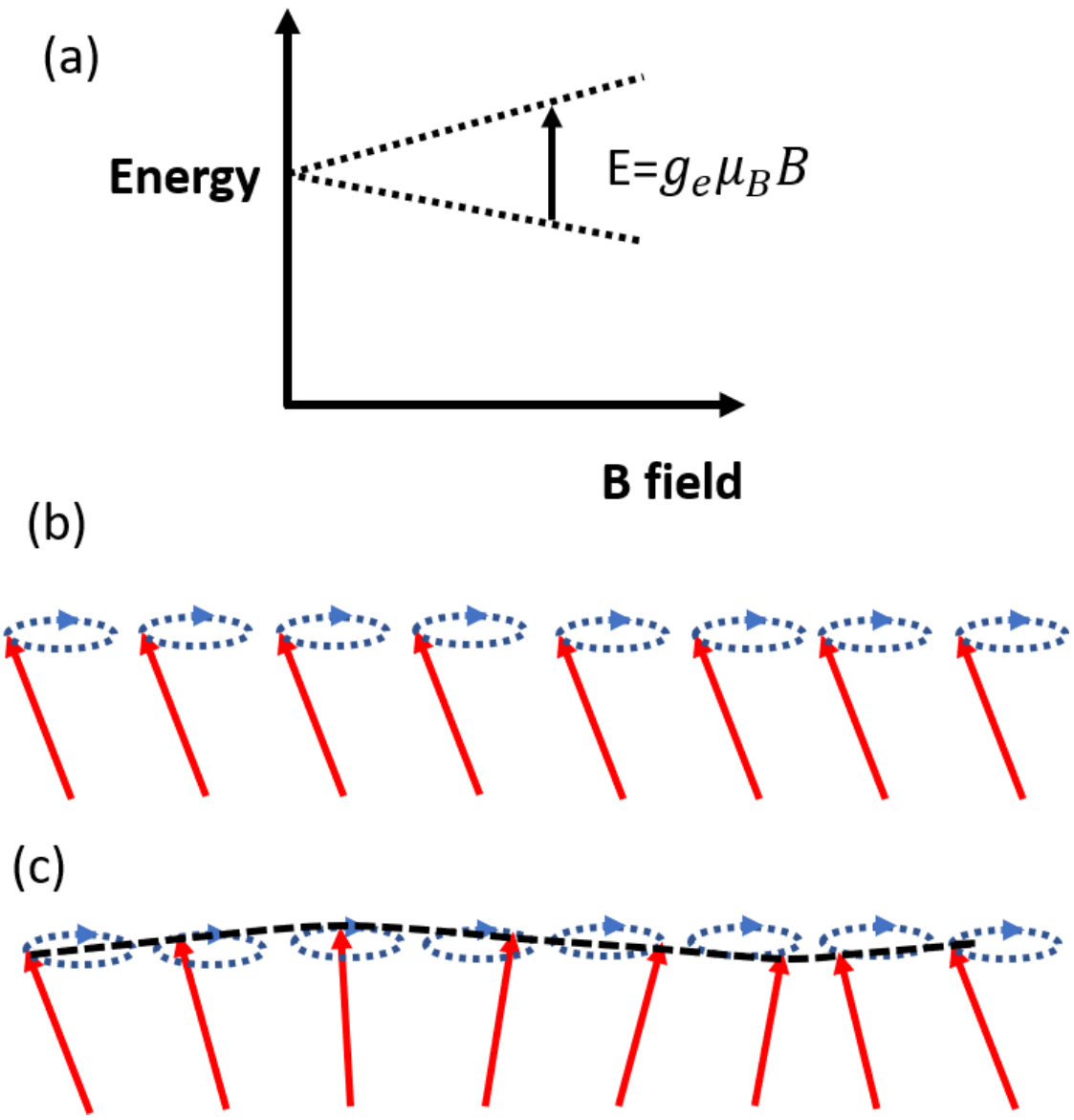

Figure 1.5: (a) Zeeman splitting in the presence of magnetic field and the transition may occur if the Zeeman energy falls in the energy range of the electromagnetic field. (b) Coherent spin wave with k=0 that may be excited by light. (c) Propagating spin wave with finite moment that can be transferred from neutron scattering.

of a single electron is considered. For most materials, the situation is much more complicated and using TDTS we can obtain useful information. First,

each atom contains more than a single electron and each single electron has spin-orbit coupling effect. The magnetic moment of an atom is associated with its total angular momentum J which is a sum of the orbital angular momentum L and the spin angular momentum S. In 1927 Friedrich Hund developed Hund's rule to determine the ground state of multiple electrons in terms of L, S and J. The ground state may still be highly degenerate within the total angular momentum J manifold and the degeneracy may be lifted due to a static electric field produced by surrounding charge distribution (anion neighbours). For transition metal, the crystal field effect is stronger than spin-orbit coupling, while for heavy elements such as rare earths the crystal field should be considered after spin-orbit coupling.The transition between different crystal field levels can also be induced by THz radiation under certain optical selection rules. This will provide useful information to the frustrated magnetism community. Second, the magnetic moment for one atom is not isolated and it interacts with magnetic moment from adjacent atoms. For magnets having long range order, the excitations are spin-waves or magnons, whose dispersion can be derived from spin Hamiltonian and detected by neutron scattering. The wavelength of THz light is much longer than the lattice and can excite coherent long wavelength spin wave. In reciprocal space, it corresponds to magnons with nearly q=0. Therefore, TDTS is able to provide high-quality data at the zone center, which is usually difficult to access by neutron scattering because neutron can

not transfer zero momentum with finite energy required by momentum and energy conservation. Furthermore, ac magnetic susceptibility can be calculated from the THz transmission spectrum and can be compared to dc susceptibility from Physical Property Measurement System (PPMS). Combining TDTS and other techniques, such as neutron scattering or dc susceptibility measurements thus opens up a new avenue in studying frustrated magnetism.

1.4 Thesis Overview

In this thesis, I investigate frustrated magnetism using time domain terahertz spectroscopy (TDTS). In Chapter 2, I will give a brief introduction to time domain terahertz spectroscopy and the data analysis. In Chapter 3, we study a triangular lattice spin liquid candidate $YbMgGaO_4$ by combining TDTS and neutron scattering. the exchange constant in this compound is determined accurately in magnetic field polarized regime and we find this compound lies close to the spin liquid regime in phase diagram. In Chapter 4, we focuses on $Tb_2Ti_2O_7$ that has a pyrochlore lattice. We observed several crystal field anomalies as a function of magnetic field. Based on single ion calculations we can explain the crystal field anomalies by low energy crystal field hybridyzation. In addition, we found the magnetic field can change the crystal field environment significantly due to strong spin-lattice coupling. In Chapter 5, we

measured a Co based Kitaev spin liquid candidate $Ba(Co)_2(AsO_4)_2$ with hexagonal lattice. We found this materials orders at low temperature due to non-Kitaev terms. However, by applying magnetic field, the order is suppressed and it reaches a field induced spin liquid regime with very small magnetic field. In chapter 6, I show our results on $Yb_2Ti_2O_7$ using TDTS and dc susceptibility measurements and revealing the spectral weights in this compound.

Chapter 2

Time Domain Terahertz Spectroscopy

2.1 Introduction to Time Domain Terahertz Spectroscopy

Terahertz (THz) region refers to a very special frequency range from 0.1 to 3 THz between the microwave and infrared regions of the electromagnetic spectrum. It turns out that many interesting and characteristic energy scales of collective modes fall in this special range, such as the vibrational frequencies of molecular crystals, the superconducting energy gap, the resonant frequency of magnon, the relaxation rates of electrons in metals, etc. Therefore, develop-

ing a spectrometer that can cover this frequency range is suitable to research investigations. However, it is unfortunate that this spectral range lies in the so-called "THz Gap", below which are accessible with traditional electronics and above which are accessible with typical optical instrumentation [60]. I will introduce the methods to generate and detect THz in following section.

2.1.1 Terahertz Generation

Decades ago, it was really challenging to obtain a spectrum that covers the "THz Gap". Nowadays, THz spectroscopy develops very fast due to its capability to study various interesting phenomena and potential applications. Currently, there are multiple ways to generate THz. The first way is to use optical rectification, which is a non-linear optical process consisting of difference frequency generation between spectral components of a femto-second laser in nonlinear crystals. Zinc telluride and lithium niobate are popular nonlinear crystals and have good THz generation efficiency from 0.2 to 2 THz. The second way is using the spin Hall effect and inverse spin Hall effect. The spin Hall effect is the phenomenon where the spin current is generated from a charge current. The inverse spin Hall effect on the other hand, is the generation of charge imbalance as a result of a spin current. A near infrared femtosecond pump pulse drives the electronic systems of a ferromagnetic and a non-magnetic layer out of equilibrium. Due to different transport properties for majority and minority

spin channels in the ferromagnetic material, an ultrafast spin current is generated and injected into the non-magnetic layer. The spin current is converted into a transverse charge current by the inverse spin Hall effect, which then emits a THz electromagnetic pulse.

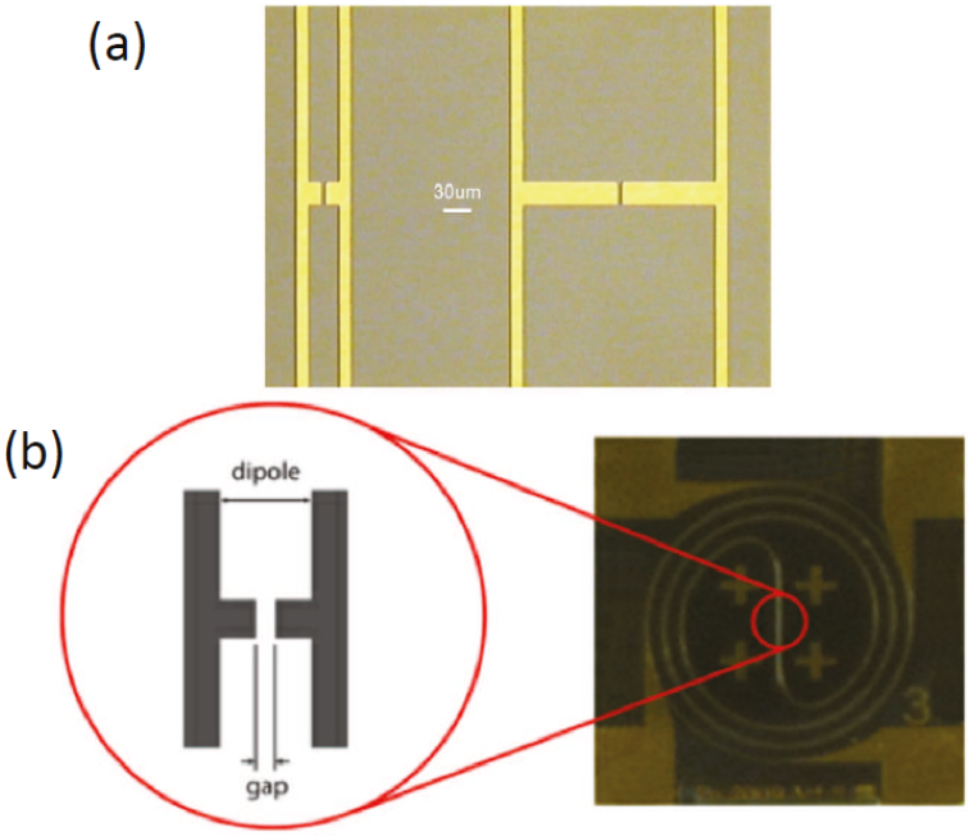

Figure 2.1: Auston switches. (a) Micro-structure of photoconductive switches made by L. Bilbro [8]. (b) Auston switch purchased from Menlosystems. At the center there is a dipole consisting of two parallel stripes just like the homemade Auston switches. Figures are from [8]

Another way to generate THz, which is adopted by our lab, is based on accelerating electrons in a biased photoconductive antennae, so called "Auston

switch" [61]. As shown in Fig. 2.1, an Auston switch consists of a semiconductor (LT-GaAs) substrate and two parallel metallic stripes (gold) deposited on the substrate. There is a small gap between the two stripes around 5 μm. Before illumination by the femtosecond laser pulse, the switch is inactive and applying voltage can not generate THz radiation as there are no free carries in semiconductor. After illumination by an infrared femtosecond laser, which will excite the electrons across the band gap, the switch becomes active and an applied voltage can accelerate free carries, leading to a transient photocurrent and associated dipole moment $\vec{p}(t)$. According to Maxwell's equations, a time dependent dipole moment can generate electromagnetic waves in far field limit by

$$\vec{E}(\vec{r},t) = \frac{1}{4\pi\epsilon_0 c^2 \vec{r}}[\vec{r} \times (\vec{r} \times \frac{d^2\vec{p}(t)}{dt^2})]. \tag{2.1}$$

The radiation stops once the excited free carriers are recombined and the switch is back to inactive mode. The generated pulse lasts in the order of picosecond, thus the corresponding frequency range of the radiation is in THz. By repeating the above process, a sequence of THz pulses can be generated. The obtained frequency content is mainly determined by the structure of the antenna and the intrinsic time scale of the generation process. The peak power of the THz pulse occurs near the resonant frequency of the antenna, which is $f_0 = c/2L$, where L is the spacing between the two parallel stripes. The shorter spacing, the more efficiency for high frequency THz generation, while the larger spac-

ing, the more efficiency for low frequency generation. The upper frequency limit is set by a combination of laser pulse width τ_L, the carriers relaxation time τ_c, and the carriers recombination time τ_r. In L. Bilbro's thesis [8], he performed a simulation by varying those parameters and find that with typical time scale τ_L=50 fs, τ_c=200 fs, and τ_r=1 ps, τ_L has the largest impact, then τ_c and τ_r. Therefore, it's very important to use a laser with short τ_L.

2.1.2 Terahertz Free Space Coupling and Propagation

The index of refraction of LT-GaAs n$\sim$3.3 is much larger than air, so most of the THz radiation generated in the GaAs will be internally reflected. We can minimize the internal reflection by placing a silicon lens that has similar index of refraction on the substrate. Using a hemispherical silicon lens can couple THz to free space efficiently, but the THz radiation has a large solid angle and less efficient for THz propagation. Using a hyper-hemispherical lens can collimate the beam and gives a perfect collimation if the the height of hyper-hemispherical lens h satisfies $h = rn_s/(n_s - 1) - d$, where r is the spherical radius, n_s is the index of refraction of the substrate and d is the thickness of the substrate. Fig. 2.2 (a)-(d) shows the THz radiation with no silicon lens, hemispherical silicon lens, slightly hyper-hemispherical lens and ideal hyper-

hemispherical lens, respectively.

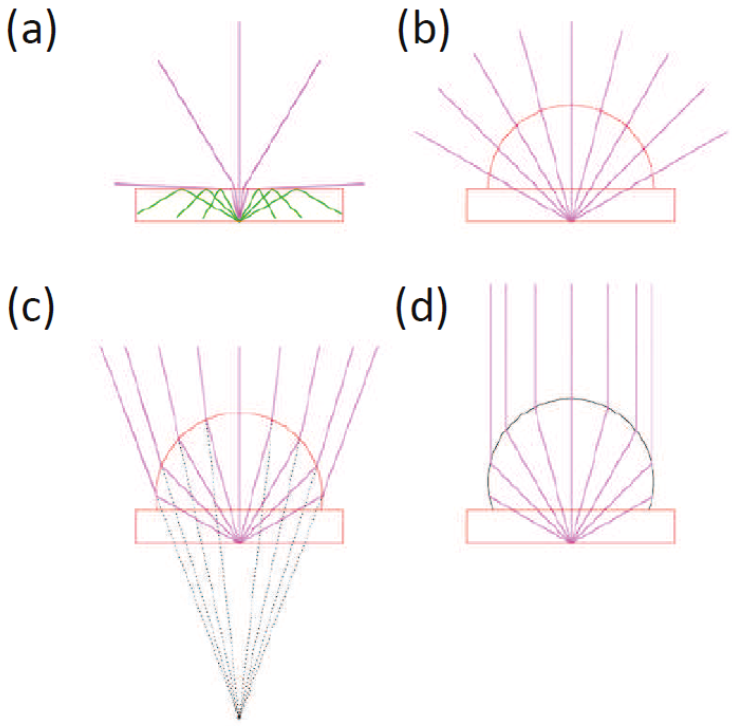

Figure 2.2: (a) Auston switch without silicon lens and most of the THz radiation is reflected back (b) Auston switch with hemispherical silicon lens and the radiation can couple to the free space but not collimated. (c) With a slightly hyper-hemispherical lens, the THz radiation is collimated better. (d) With ideal hyper-hemispherical lens, the radiation is collimated perfectly. Figures are from [8]

After the THz is emitted from the Auston switch, we need to guide THz radiation and focus into sample space. We use off axis parabolic (OAP) mirrors to collimate and focus the beam instead of lens, thereby no obstruction of the beam. Nevertheless, OAPs will introduce optical abberations (coma and astigmatism). In our lab, we use a so-called "8f configuration" scheme, which

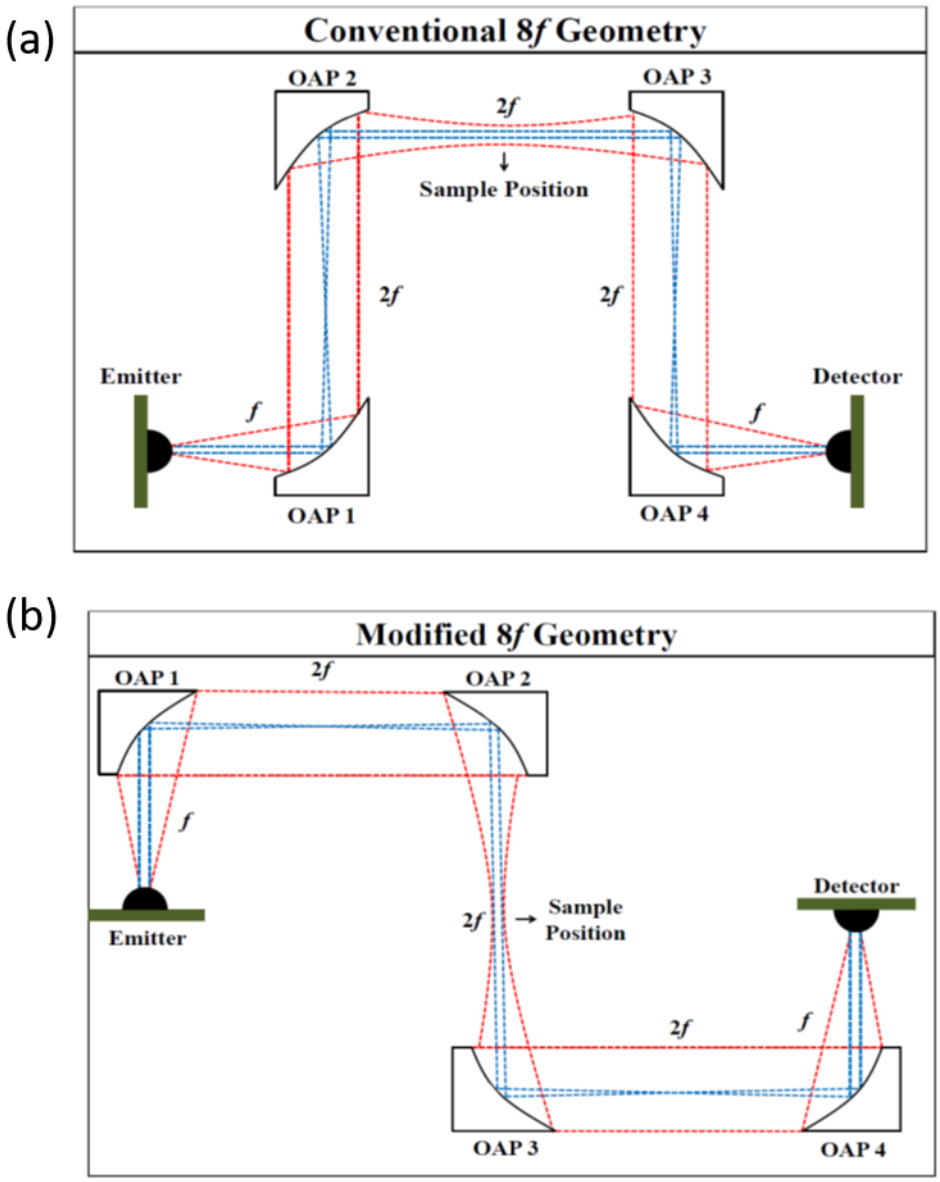

Figure 2.3: (a) conventional $8f$ configuration. Red and blue dashes lines represent low and high frequency contain in THz pulse. OAP 2 is 180 degree rotation of OPA 1, which leads to large optical aberrations. OAP 3 and 4 are inverse process of OAP 1 and 2.(b) Modified $8f$ configuration. OAP 2 is mirror image of OPA 1, which leads to reduced optical aberrations. Again OAP 3 and 4 are inverse process of OAP 1 and 2. Figures are from [9].

the total THz beam path is 8 times the focal length of one OAP. As shown in Fig. 2.3, there are two geometries, one is conventional $8f$ configuration and the other is modified $8f$ configuration. It has been shown by Nick Laurita with simulation that the conventional $8f$ configuration has an enhanced optical abberations with distorted image, larger focus spot and lower intensity [9]. In contrast, the modified $8f$ configuration can compensate the optical aberrations significantly, leading to undistorted image and smaller focus spot.

2.1.3 Terahertz Detection

If the THz is generated with nonlinear crystals, electro-optical sampling method is usually used to detect the THz signal. It uses a material which has the property which changes its optical characteristics when an electric field is applied to it. In the case of THz spectroscopy, the incident THz pulse induces a birefringence in an electro-optic medium (ZnTe), which is proportional to the electric field of the pulse. This varying birefringence can be measured with a infrared probe laser, whose polarization status is also changing correspondingly. After the detection crystal, the probe laser passes through a 1/4 wave plate and then is split into two branches with orthogonal polarization by a Wollaston prism and finally were focused onto a pair of balanced photodiodes. The output signal was recorded by a data acquisition card. In the absence of terahertz, the difference of the balanced photodiodes is zero, while in the presence of THz a

difference reflects the THz electric field [62].

If we use Auston switch as emitter to generate THz, we can use another Auston switch as receiver to detect THz signal. The difference is that the emitter is biased by an externally applied voltage, while the receiver is biased by the electric field of the THz pulse. Similarly, the switch is only active when it's illuminated by an infrared laser and a photocurrent is generated and measured, which is proportional to the electric field of the THz pulse. We use a linear delay state with maximum scanning length of 10 cm as an optical delay. By scanning the delay stage, we can vary the difference of optical path between the emitter and receiver arms of the experiment so that we can map out the electric field of the THz pulse in time domain. This way allows us to obtain both the magnitude and phase information of the THz pulse, which can be converted to the frequency domain by Fourier transformation. Therefore, we are able to obtain complex transmission without using Kramers-Kronig (KK) relations. This is a great advantage for THz spectroscopy over intensity measurements like Fourier transform infrared spectroscopy (FTIR), which requires to measure over a large frequency range to apply KK transformation.

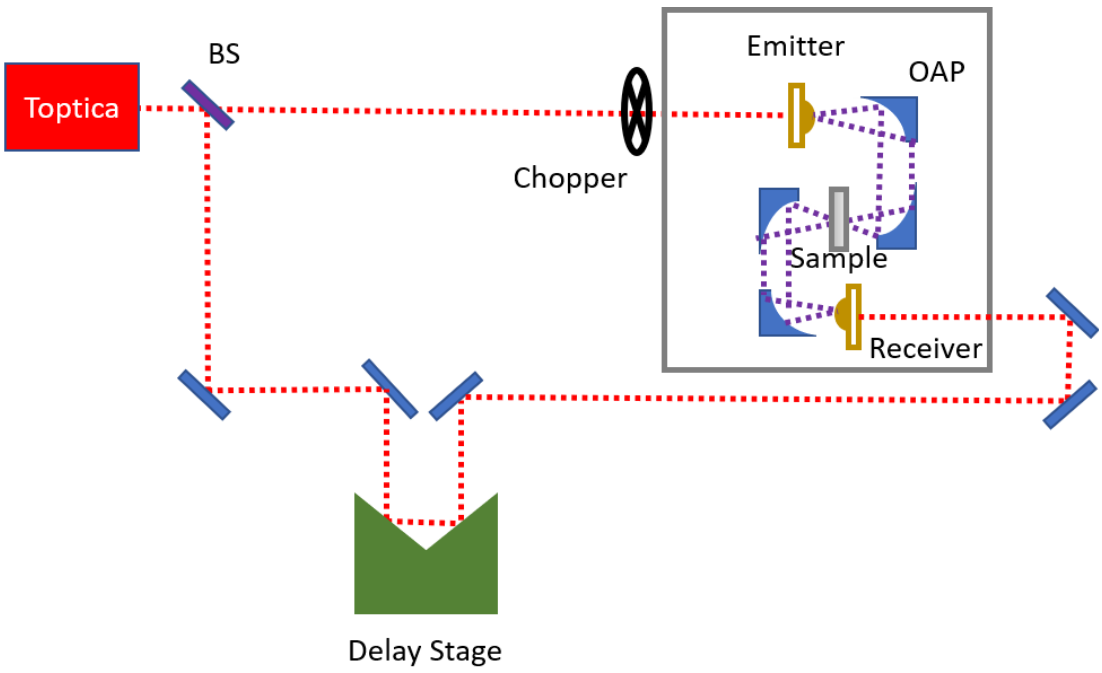

Figure 2.4: (a) The scheme of THz setup in BLC. Red dashed line and purple dashed line represent laser and THz pulses, respectively. Red box is Toptica ultrafast infrared laser, beamsplitter (BS) is in purple, protected silver mirrors and OAPs are in blue, emitter and receiver are in yellow, chopper is in black, delay stage is in green and sample is in grey. The grey box is purged with dry air to reduce the water absorption in THz range. Electronic devices are not shown in the figure.

2.2 Terahertz setups in our lab

In Armitage's lab, we currently have two TDTS setups. One is called "BLC", which is named after three previous graduate students (Luke Bilbro, Nick Laurita, Bing Cheng) who built the system. The other one is equipped with a magnet and can do field dependent measurement. Fig. 2.4 is the scheme of the BLC system.

As mentioned earlier THz generation requires ultrafast infrared laser and

we used Integral model Ti:Sapphire solid state laser purchased from Femtolasers before, but recently it has retired and been replaced by an ultrafast fiber laser from Toptica. Both lasers generate 800 nm infrared laser with 80 MHz repetition rate, but the fiber laser has better stability and lower price (but unfortunately longer pulse lengths). Therefore, now we are using the fiber laser for both BLC and the magnet system.

The laser is split by a beamsplitter. One beam illuminates the Auston switch on emitter side and the other goes to receiver side. The emitter is biased by a DC power supply (HP Agilent model 6633) with 24 V. The voltage should be applied before laser illumination to avoid spikes on emitter (otherwise the Auston switch may be damaged easily). We also use ND filter (NDC-50S-3M) from Thorlabs to reduce the laser power before illuminating the Auston switch (around 10 mW). Once the THz is generated from the emitter, we use the $8f$ configuration of 4 OAPs to collimate and focus the THz radiation to the sample place and then to the receiver. If the infrared laser arrives the receiver at the same time as the THz pulse, a photocurrent will be detected. Then the receiver is connected to a current preamplifier (model SR570), which measures and amplifies the photocurrent and converts it to a voltage, recorded by a lock-in amplifier (SR830) from Standard Research System. An optical chopper (model MC2000) is used to modulate the laser pulses and feeds into a lock-in amplifier as a reference frequency (around 800Hz).

It is essential that the two optical paths on the emitter and receiver sides should be equal. Furthermore, by moving the delay stage with a retro-reflector (Physik Instrumente M-511.DD) we can map out the THz electric field in time domain with both magnitude and phase. It can be converted to the frequency domain by Fourier transformation. By measuring both the sample and an aperture as reference and taking their ratio we can obtain complex transmission.

As for the magnet system, most parts are similar, but there are a few changes. We use AC bias (from Zomega Terahertz) with maximal 40 V (around 28 V on average) instead of DC voltage. The AC bias was synchronized with a synthesized function generator (Instek SFG-2004) with a frequency of 14 kHz and no need to use a chopper. Since we have magnetic field in this setup, certain materials may have Faraday rotation effects in the presence of magnetic field, therefore it's necessary to measure THz signal in both x and y directions. This can be achieved by a so-called "fast rotator" (a fast rotating polarizer). It can measure the vertical (x) and horizontal (y) components of the THz electric field simultaneously using the in-phase and out-of-phase channels of a lock-in amplifier. Using a fast rotator has many advantages over measuring x and y individually. Time dependent noise can be referenced out and many detrimental effects such as the finite extinction ratio of the analyzing polarizers can be cancelled out as well, improving the accuracy of the measurement.

As shown in Fig. 2.5, a static wire grid polarizer (WGP) is placed before

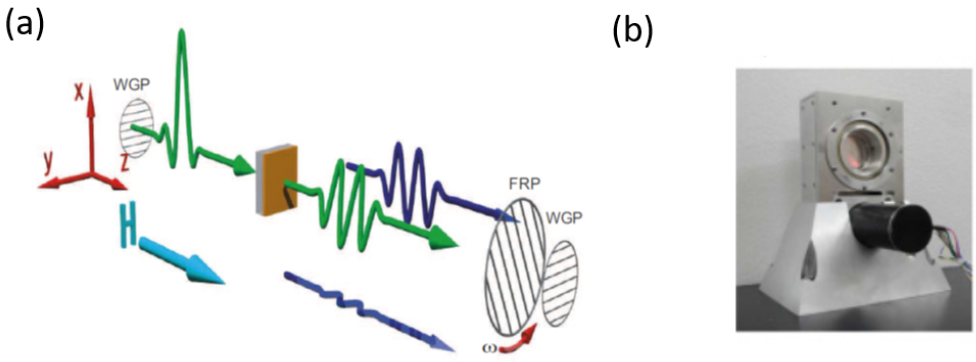

Figure 2.5: (a) A scheme of the application of the fast rotator. The two wire grip polarizers only transmit vertical THz. (b) It's a photo of the fast rotator. Figures are from [10, 11]

the sample and the fast rotator and another static WGP are placed after the sample but before the receiver. The principle can be understood by the Jones matrix formalism. The initial THz electric field can be represented as

$$\vec{E}_i = \begin{bmatrix} E_i^x \\ \\ E_i^y \end{bmatrix}. \tag{2.2}$$

The static WGP that passes only vertical component THz pulse can be represented as

$$P_y = \begin{bmatrix} 0 & 0 \\ \\ 0 & 1 \end{bmatrix}. \tag{2.3}$$

. Linear polarizer with axis of transmission angle θ from the horizontal direc-

tion is

$$\begin{bmatrix} \cos^2(\theta) & \cos(\theta)\sin(\theta) \\ \cos(\theta)\sin(\theta) & \sin^2(\theta) \end{bmatrix}. \tag{2.4}$$

Applying this to the fast rotator (P_F), we have θ replaced by Ωt, where Ω is the angular momentum of the fast rotator.

$$P_F = \begin{bmatrix} \cos^2(\Omega t) & \cos(\Omega t)\sin(\Omega t) \\ \cos(\Omega t)\sin(\Omega t) & \sin^2(\Omega t) \end{bmatrix}. \tag{2.5}$$

The sample transmission matrix is

$$T = \begin{bmatrix} T_{xx} & T_{xy} \\ T_{yx} & T_{yy} \end{bmatrix}. \tag{2.6}$$

Therefore the final THz electric field can be represented by

$$\vec{E_f} = \begin{bmatrix} E_f^x \\ E_f^y \end{bmatrix} = P_y P_F T \begin{bmatrix} E_i^x \\ E_i^y \end{bmatrix} = \begin{bmatrix} 0 \\ \frac{E_i^y}{2}(T_{xy}\sin(2\Omega t) + T_{yy}(1+\cos(2\Omega t))) \end{bmatrix}. \tag{2.7}$$

The electric field generates photocurrent in receiver and converted to voltage by a preamplifier (Keithley 428), which are connected to the first lock-in amplifier with modulation of 14 kHz. The signal is then send to a second lock-in amplifier. The signal which contains information about T_{yy} is modulated with $\cos(2\Omega t)$ ($2\Omega \sim 45$Hz) and integrated for an amount of time determined by the

lock-in time constant (100 ms), and appears in the in-phase channel of the second lock-in amplifier. Likewise, the signal containing information of T_{xy} is modulated by $\sin(2\Omega t)$ and appears in the out-phase channel [11]. In Faraday geometry, for a material with C_4 or C_3 symmetry, we have $T_{xy} = -T_{yx}$ and $T_{yy} = T_{xx}$ [63]. Finally by dividing the signal of sample by an aperture to get rid of prefactors, we can get complex transmissions T_{xy} and T_{xx}. Note that photoconductive antenna has polarization sensitivity and it is close to vertical, hence we use static WGP passing only the vertical THz P_y. Alternatively, using a WGP that passes horizontal THz also works but will obtain smaller signals.

2.3 Cryogenic Experimental Setups

2.3.1 Continuous flow He^4 Cryostat

In the BLC setup, we use continuous flow He^4 optical cryostat from Janis, allowing us to measure from 1.5 K to 300 K. In order to reach 1.5 K, we need to open the needle valve completely and pump with a roughing pump for 15 minutes. We should be able to see the signal peak shifts for around 400 um, indicating the sample and aperture are submerged with liquid helium. After 15 minutes accumulation of liquid helium in cryostat, we need to close the needle valve to reduce the vapor pressure of the liquid He^4 in the system, thereby

cooling the system down to 1.5 K. It is hard to stabilize the temperature around 2.2 K due to the boiling of liquid helium at Lambda point. We use temperature controller (Lakeshore 332) to stabilize the temperature above 4 K. Sometimes the helium quality is not very good and we need to adjust the needle valve frequently to keep continuous helium flow.

2.3.2 Closed-Cycle Cryostat with 7 T Superconducting Magnet

Since I studied frustrated magnetism, I used the magnet setup for most of my experiments. We use a closed-cycle cryostat with a 7 T superconducting magnet. The magnet is from Sumitomo and the cryostat is from Janis. The initial cooling from room temperature to 100 K is cooled by the cold head with constant pumping on the sample space. Further cooling requires to introduce ultra pure He^4 gas into the sample chamber. The ultra pure He^4 gas acts as exchange gas to conduct heat between the sample and the cold head. Above 100 K, the helium may leak through the window into outer vacuum jacket, so we should introduce helium gas only below 100 K. We can get as low as 4 K by this method. If we need lower temperature as 1.5 K, we also need to do similar thing as in BLC, filling and pumping liquid helium with a new designed insert.

2.3.3 Rotating the Magnet

We have two configurations for the magnet. One is the Faraday geometry, where the wavevector of THz is along the external magnetic field, and the other is the Voigt geometry, where wavevector of the THz is perpendicular to the magnetic field. We can perform experiments with these two configurations by rotating the magnet. It usually takes one week to switch between these two configurations. We need to warm up the magnet first, then use a crane to lift the cryostat and rotate it by 90 degrees. We also need to change the windows/blocks/radiation shields correspondingly. After putting it back, we have to pump the outer vacuum jacket with turbo pump from Pfeiffer Vacuum. After reaching a pressure below 10^{-4} mbar, we can cool down the system again. Since it takes tremendous efforts and time, we do this once a year.

2.4 Data Analysis

As mentioned earlier, we measured electric field of both sample and aperture in time domain by moving a delay stage. In principle, a smaller step size and long scanning length will lead to higher quality data with a trade off of time. We usually use 10 μm as step size and 3000 μm scan length for aperture and longer for sample. We can add zero padding to interpolate the frequency domain date thereby artificially increasing the resolution even for short scan

length. In addition, we can window the signal such as multiplying a cosine function to remove the sudden jumps at the end of signals, therefore preventing false frequency contents in the spectrum, that produce the discontinuity at the period's boundary as doing Fourier transform.This phenomenon is known as spectral leakage. After we obtain the spectra $\tilde{E}_{sam}(\omega)$ and $\tilde{E}_{ap}(\omega)$ in frequency domain by Fourier transform, the complex transmission is obtained by $\tilde{T}(\omega) = \tilde{E}_{sam}(\omega)/\tilde{E}_{ap}(\omega)$. Once we obtain the complex transmission, we can extract index of refraction and magnetic susceptibility for magnetic materials or conductivity for metallic materials.

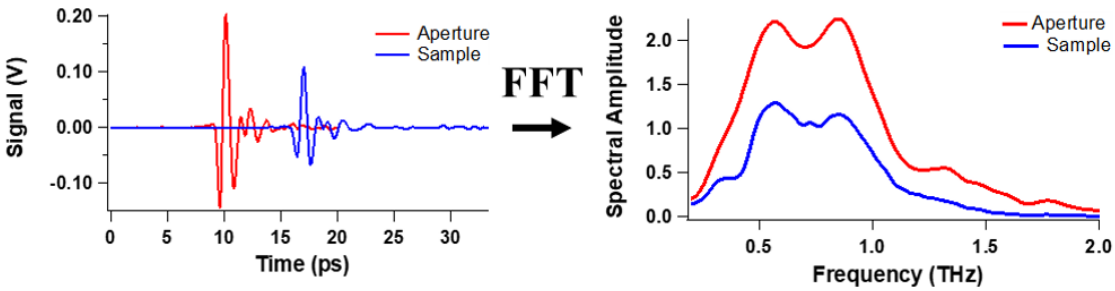

Figure 2.6: Typical THz pulses of an aperture and a sample in time domain (left) and spectrum of aperture and sample in frequency domain after Fourier transformation (right).

2.4.1 Index of Refraction

The formula to extract the index of refraction of our sample depends on whether the sample is a thin film or a single crystal. In this thesis, all the samples are single crystal and I will follow the same procedure as in Ref. [9]. When

the THz passes through a sample, it first reaches the interface between the sample and the air. The transmission coefficient is given by Fresnel equation $t = \frac{2Z_s}{Z_0+Z_s}$, where $Z_0 \sim 377\Omega$ and $Z_s = \sqrt{\mu/\epsilon}$ are impedance for air and sample, respectively. The transmitted wave will accumulate a phase while traveling through the sample given by $exp(i\frac{\omega d}{c}n_s)$, where c is speed of light, d is the thickness of sample and $n_s = \sqrt{\mu\epsilon}$ is the index of refraction. The THz then will reach the second interface between the sample and air again. Therefore, the total transmission for the sample is given by

$$\tilde{t}_{sam}(\omega) = \frac{4Z_s}{(Z_0 + Z_s)^2} exp(i\frac{\omega d}{c}n_s) \tag{2.8}$$

Similarly, the total transmission for the air (through an aperture) is given by

$$\tilde{t}_{ap}(\omega) = exp(i\frac{\omega d}{c}) \tag{2.9}$$

Therefore, we get the complex transmission by dividing them

$$\tilde{T}(\omega) = \frac{4Z_s}{(Z_0 + Z_s)^2} exp(i\frac{\omega d}{c}(n_s - 1)) \tag{2.10}$$

Since the exponential term has the most contribution compared to the prefactor and the magnetic susceptibility χ is much smaller than 1 (i.e. $\mu \sim 1$), we can replace the impedance by index of refraction for the prefactor, so the

complex transmission is given by

$$\tilde{T}(\omega) = \frac{4n_s}{(1+n_s)^2} exp(i\frac{\omega d}{c}(n_s - 1)) \tag{2.11}$$

Here we are pursuing for the real and imaginary parts of the index of refraction with the experimentally measured complex transmission of the sample. We can use a so-called Newton-Raphson method to numerically calculate the index of refraction for each frequency at given temperature [9].

2.4.2 Magnetic Susceptibility

Once we obtain the index of refraction, we may further obtain the magnetic susceptibility. We need to obtain the index of refraction at both low temperature (the desired temperature) and high temperature (reference temperature), above which the magnetic susceptibility is 0. We also need to make an assumption that the dielectric constant doesn't change too much between these two temperatures, which can be a reasonable assumption. Therefore, with the relation $\mu = 1 + \chi$, the index of refraction at reference temperature is given by

$$n_{ref} = \sqrt{\epsilon} \tag{2.12}$$

The index of refraction at desired temperature is

$$n = \sqrt{\epsilon(1+\chi)} \tag{2.13}$$

Then we can obtain the magnetic susceptibility

$$\chi = (\frac{n}{n_{ref}})^2 - 1 \tag{2.14}$$

The obtained real and imaginary magnetic susceptibility are related by Kramer-Kronig transformation. The way to choose reference temperature is empirical. We don't want to see any magnetic features at this temperature and also don't want to choose a temperature that is too high (100 K is usually good enough).

2.4.3 Converting Linear Basis to Circular Basis

Here, we show how to convert the transmission in linear basis to circular basis. The complex transmission of a sample in linear basis can be represented by Jones matrix

$$T_{linear} = \begin{bmatrix} T_{xx} & T_{xy} \\ T_{yx} & T_{yy} \end{bmatrix} \tag{2.15}$$

In general, these four elements are independent. However, if the sample is cubic or hexagonal, possessing certain symmetry such as C_3 or C_4 symmetry, the

matrix becomes anti-symmetric $T_{xy} = -T_{yx}$ and $T_{yy} = T_{xx}$ in Faraday geometry ($k_{THz} \parallel B_{dc}$) [63]. A matrix in linear basis can be converted into circular basis by

$$T_{cir} = \Lambda^{-1} T_{linear} \Lambda \tag{2.16}$$

with

$$\Lambda = \frac{1}{\sqrt{2}} \begin{bmatrix} 1 & 1 \\ -i & i \end{bmatrix} \tag{2.17}$$

As a result, the fully anti-symmetric matrix is diagonalized in circular basis

$$\begin{bmatrix} T_r & 0 \\ 0 & T_l \end{bmatrix} = \begin{bmatrix} T_{xx} + iT_{xy} & 0 \\ 0 & T_{xx} - iT_{xy} \end{bmatrix} \tag{2.18}$$

suggesting the circular basis is the eigenpolariztion in Faraday geometry.

It's important to represent data in correct basis. For instance, THz can be rotated out of the x axis into the y direction, but this can be misconstrued as an absorption of light in the x direction. There is an intuitive way to understand the circular basis as eigenbasis. Photons possess angular momentum $\pm\hbar$ for left and right polarized light. For magnetic materials in Faraday geometry, exciting spin waves or transitions between different crystal field levels also requires changing angular momentum $\pm\hbar$, therefore the spin wave excitations or crystal field excitations can only appear in either left or right circular basis. Converting to circular basis is not only important for magnetic system, but also

important for other non-magnetic system, such as studying cyclotron resonance [64].

Chapter 3

Hierarchy of Exchange Interactions in the Triangular Lattice Spin Liquid Candidate $YbMgGaO_4$

$YbMgGaO_4$ has attracted attention recently as a quantum spin liquid candidate. There are many works that show evidences of spin liquid, but the experimental features may be obscured by site mixing disorder between Mg and Ga. Several groups have tried to determine the exchange interactions. It has been both proposed that $YbMgGaO_4$ is an excellent example of a spin liquid or based on theoretically calculated phase diagram of exchange interactions that

it is in fact a disorder induced mimicry of spin liquid [1, 17, 65, 66]. However, previously determined exchange interactions were not very accurate due to certain limitations of experimental techniques. In this chapter, I combine time domain terahertz spectroscopy (TDTS) and neutron scattering to determine the exchange interactions accurately in the field polarized state of $YbMgGaO_4$. Our results place $YbMgGaO_4$ closer to the spin liquid regime than previously thought.

3.1 Introduction to $YbMgGaO_4$

3.1.1 Spin 1/2 Triangular Heisenberg Antiferromagnet

The most celebrated prototype of a QSL is the resonating valence-bond (RVB) state first proposed by Anderson in 1973 [51] for the spin-1/2 triangular-lattice Heisenberg antiferromagnet (TLHAF) and later extended to the square-lattice in the context of cuprate superconductors [52]. However, precise numerical calculations for the spin-1/2 TLHAF, which take into account nearest neighbor interactions only [67–69], indicate that quantum fluctuations are not enough to suppress magnetic ordering and the actual ground-state is a non-collinear 120 degree long-range ordered spin structure. Experiments on

various spin-S triangular-lattice antiferromagnets have overwhelmingly confirmed this picture [70–73], with a few noteworthy exceptions [74–76]. Several perturbations from the pure TLHAF have been proposed to enhance quantum fluctuations and hence destablize the long range ordered state, including next-nearest neighbor interactions (NNN) [12, 77–80], ring-exchange terms [81, 82] and anisotropic exchange [2, 13, 83, 84]. As shown in Fig. 3.1 (a), by adjusting the ratio of NNN interactions over nearest interaction, it is believed to be possible to realize a spin liquid state. Fig. 3.1 (b) is the phase diagram in terms of the anisotropic exchange interactions. At the boundary of two regions, the quantum fluctuations are strong enough to destablize the long range order.

3.1.2 Evidence for Spin Liquid

The newly discovered rare-earth triangular-lattice antiferromagnet $YbMgGaO_4$ [14, 16] has attracted a lot of attention recently. The magnetic Yb^{3+} ions carry effective spin-$1/2$ moments in a symmetric environment and forbid antisymmetric (Dzyaloshinsky-Moriya) terms and magnetic defects, both of which are present in other two-dimensional QSL candidates such as Herbertsmithite [85–87]. But $YbMgGaO_4$ allows both the NNN interactions and anisotropic exchange interactions to be present, as a result, the long range ordered state may be destablized and a spin liquid state may form [31, 35, 65, 88–91]. The crystal structure of $YbMgGaO_4$ is shown in Fig. 3.2. The single crystals [16] uncov-

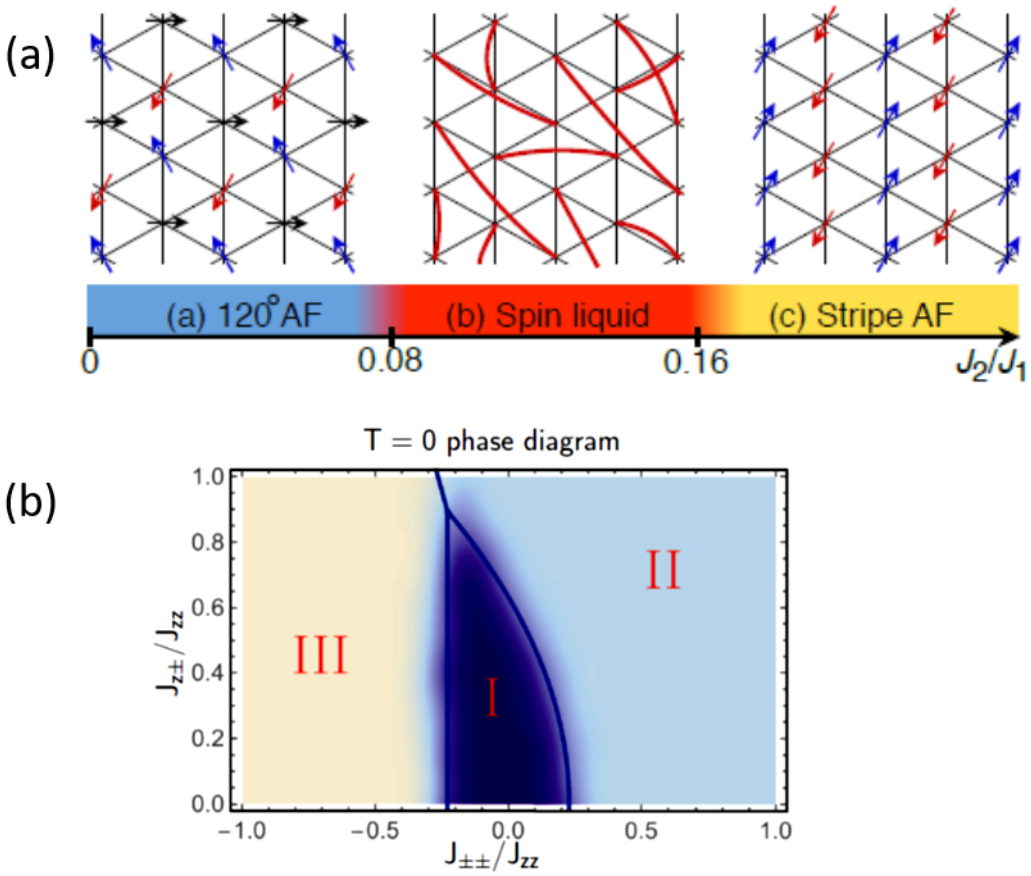

Figure 3.1: (a) The phase diagram of Spin 1/2 triangular Heisenberg Antiferromagnet with next nearest neighbor interactions. As the $J_2/J_1 < 0.08$, the ground state is a 120 degree long range ordered state. As the $0.08 < J_2/J_1 < 0.16$, the ground state is a spin liquid state. As the $J_2/J_1 > 0.16$, the ground state is a stripe antiferromagnetic state. (b) Phase diagram of Spin 1/2 triangular Heisenberg Antiferromagnet with off-diagonal anti-symmetric term ($J_1^{\pm\pm}$ and $J_1^{z\pm}$). At the boundary of two regions, the fluctuation is very strong and may realize a spin liquid state. Figures are from Ref. [12, 13]

ered a QSL phenomenology in $YbMgGaO_4$ characterized by the absence of spin ordering or freezing down to $T = 100$ mK in muon spin relaxation measurements [92], much lower than the Curie-Weiss temperature $\theta_W \approx -4$ K, and a

power-law behavior for the magnetic specific heat at low temperatures [16, 93]. Perhaps the strongest evidence for a QSL in $YbMgGaO_4$ came from inelastic neutron scattering measurements in zero field that unraveled a broad continuum of magnetic excitations across the entire Brillouin-zone [1, 15, 94]. This continuum has been interpreted as fractional excitations from a QSL state with spinon Fermi surface [15, 83, 84] or from a RVB-like state [94].

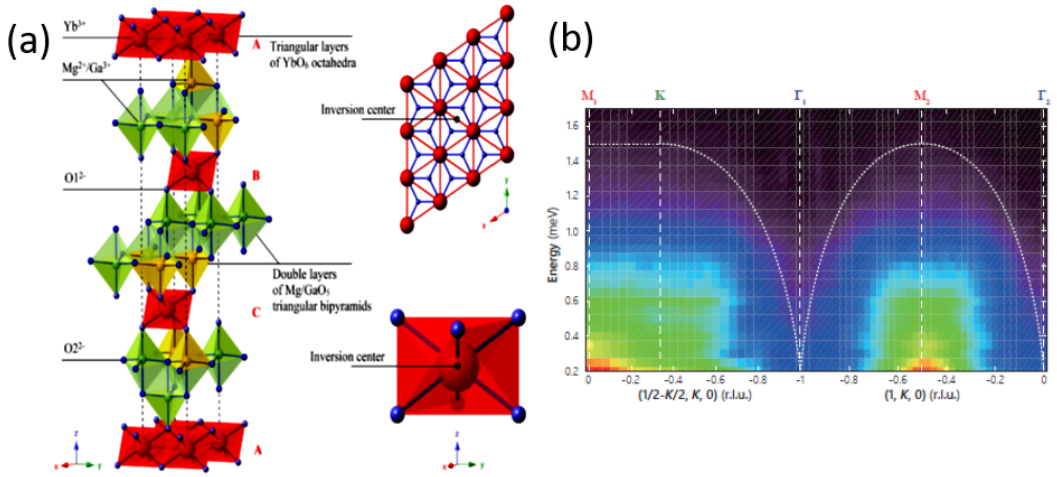

Figure 3.2: (a) The crystal structure of $YbMgGaO_4$. The magnetic Yb ions form 2 dimensional triangular lattice layers separated by non-magnetic Mg^{2+}/Ga^{3+} ions. The crystal has inversion symmetry so the DM interaction is forbidden. (b) Intensity of magnetic excitations along high symmetry direction measured by neutron scattering, showing continuum spectrum as evidence of spin liquid with spinon fermion surface. Figures are from Ref. [14, 15]

3.1.3 Disorder Induced Mimicry of Spin Liquid

While there are substantial evidences to support a spin liquid state, the absence of a magnetic contribution to the thermal conductivity [93], however, appears difficult to reconcile with the spinon Fermi surface interpretation. Additionally, the existence of disordered occupancy of Mg^{2+} and Ga^{3+} ions has been reported [14]. This site mixing of non-magnetic ions appears to affect profoundly the Yb^{3+} ions as evidenced by broadened crystal electric-field (CEF) levels [1, 95], a distribution of g-tensors [95], and a broadened magnetic excitation spectrum at high fields [1]. Moreover, the observed continuum in neutron scattering may also originate from disorder instead of fractionalized quasi-particles. The impact of disorder on the $YbMgGaO_4$ exchange Hamiltonian and whether the ground state is a QSL or not remains an outstanding issue [17, 65, 66].

3.1.4 Exchange Interactions from Previous Works

In fact, the nature of the dominant exchange interactions in $YbMgGaO_4$ is also controversial. While the overall planar anisotropy is clear from magnetic susceptibility measurements [15,16], both antiferromagnetic next-nearest-neighbor terms (J_2) [1] and nearest-neighbor anisotropic off-diagonal exchanges (so-called $J_1^{\pm\pm}$ and $J_1^{z\pm}$) [2, 96] have been proposed as extensions from the XXZ model.

Comprehensively determining the exchange interactions in $YbMgGaO_4$ is of fundamental importance in deciphering the nature of its ground state.

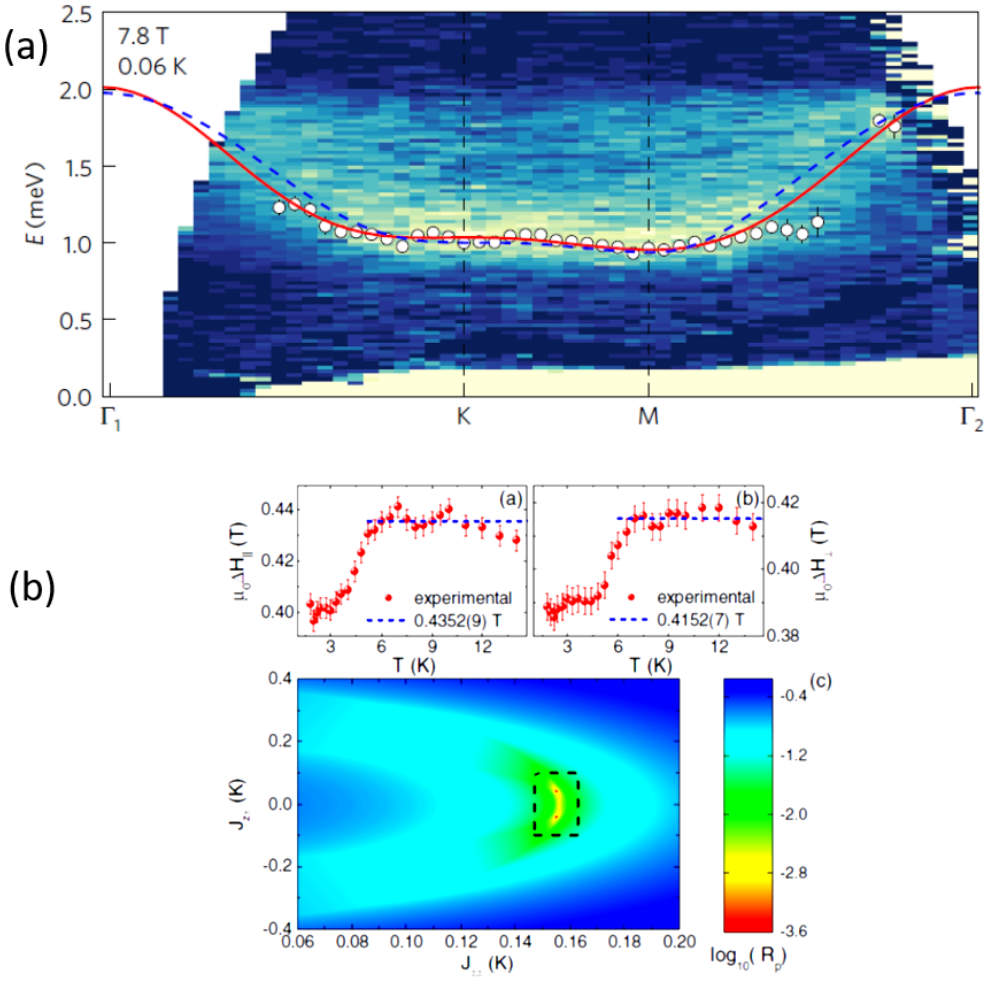

Figure 3.3: (a) Neutron scattering measurements in the field polarized regime, which shows the limitation to Γ point. (b) ESR measurements with the limitation to high magnetic fields. Figures are from Ref. [1, 16]

Neutron scattering has been used to determine the exchange interactions in field polarized regime [1] , but as shown in Fig. 3.3, the neutron scattering has difficulty in obtaining data near the Γ point and the dispersion away

from the zone center is almost flat and featureless. As a result, the previously obtained exchange interactions were not very accurate and have large uncertainty. Previous X-band electron spin resonance (ESR) measurements can probe excitations at the Γ point, but were intrinsically limited to small fields (0.4 T) below the field-polarized regime [16]. In contrast, high-resolution TDTS functioning as high-field ESR on magnetic insulators allows an accurate determination of magnetic excitations in fields comparable to the saturation field in $YbMgGaO_4$. Since the wavelength of THz radiation is much greater than the lattice constants, TDTS measures excitations in the first Brillouin zone with zero-momentum transfer (i.e., the q=0 response), which is impossible by neutron scattering. By combining TDTS and neutron scattering, we can nail down the exchange interactions precisely. The neutron scattering work was performed by Martin Mourigal and his students and postdocs at Georgia Institute of Technology.

3.2 Experimental method

The $YbMgGaO_4$ crystal (space group $R\bar{3}m$) used in this work was grown by the floating-zone technique as reported in Ref. [1] and cut with a diamond blade to present a c-axis facet, where the c-axis is orthogonal to the triangular ab plane of Yb^{3+} ions.

Inelastic neutron scattering (INS) experiments were performed by Mourigal's group using the cold neutron chopper spectrometer [97] (CNCS) at the Spallation Neutron Source (SNS), and on the cold triple-axis spectrometer (CTAX) at the High Flux Isotope Reactor (HFIR), both at Oak Ridge National Laboratory. The magnetic field of 7.8 T along the crystal c-axis and temperature around 60 mK were used on CNCS, and the magnetic field is round 10.8 T along the crystal a-axis and temperature is around 0.32 K on CTAX. The INS data taken at CNCS is the same as published in Ref. [1] but is now analyzed together with the TDTS data.

The complex THz transmission was measured down to 1.6 K with external fields up to 6.8 T in both the Faraday ($\mathbf{k} \parallel \mathbf{H}$) and Voigt ($\mathbf{k} \perp \mathbf{H}$) geometries, where k is the direction of light propagation. The $\mathbf{H} \parallel \mathrm{c}$ and $\mathbf{H} \parallel \mathrm{a}$ orientations were probed in Faraday and Voigt geometries, respectively. In both cases, the THz pulse ac magnetic field, h, was applied along a^* with $\mathrm{h} \perp \mathbf{H}$.

3.3 Experimental results

3.3.1 Spin Wave in Circular Basis

In the field-polarized state in the Faraday geometry, the linearly polarized THz pulse becomes elliptically polarized as it passes through the sample due to

spins precessing around the applied field direction. The complex transmission is represented by a 2×2 Jones matrix. Due to the three-fold rotational symmetry of the lattice, this reduces to an anti-symmetric matrix for the transmission of a linearly polarized pulse [98]. By diagonalizing this antisymmetric matrix, we can convert the transmission matrix from the linear basis into a circular basis, which naturally corresponds to eigenstates of the transmission in the Faraday geometry [35]. Fig. 3.4 (a) and (b) show such transmission magnitudes for

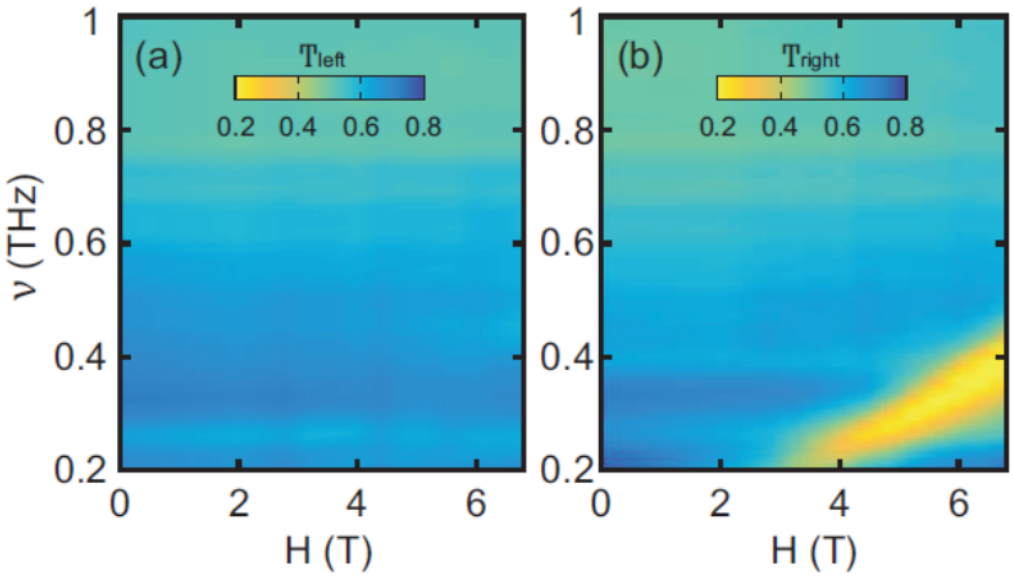

Figure 3.4: Transmission amplitude for (a) left and (b) right circularly polarized THz light as a function of frequency ν and field H_{dc} in the Faraday geometry, *i.e.* $H_{dc} \parallel c$ at 5 K. The bright yellow feature in (b) indicates the absorption due to the spin wave excitations at $\mathbf{q}=0$.

left (LCP) and right (RCP) circularly polarized THz light as a function of frequency and magnetic field, respectively. The bright yellow feature in Fig. 3.4 (b)

shows that only one particular helicity of the light (RCP) is strongly absorbed. This indicates the presence of well defined spin-wave excitations with energy linearly dependent on the applied field. In a field polarized regime in the Faraday geometry, the direction of spin precession is determined by the orientation of the applied H_{dc} field and it is therefore natural to expect an absorption for only one helicity and not the other. Indeed, our experiments confirm that when the polarity of the H_{dc} field is reversed, only LCP light is absorbed . This confirms that the absorption line observed in Fig. 3.4 (b) originates from spin-wave excitations in the field-polarized regime of $YbMgGaO_4$ [99].

3.3.2 Magnetic Susceptibility

Next, we can extract the magnetic susceptibility at 5 K for the RCP using the method described in previous section with a referencing temperature 100 K. Fig. 3.5 (a) and (b) show the real and imaginary parts of $\tilde{\chi}(\nu)$, respectively, at different fields in the Faraday geometry. Peaks in $\mathrm{Im}\tilde{\chi}(\nu)$ correspond to the spin wave excitations in the $\mathbf{q} = 0$ limit. By fitting the data at each field with Lorentzian functions, we can extract the resonant energy (E) of the spin-wave absorption. Similar analysis can be done for TDTS in the Voigt geometry to extract the spin-wave energies for field H_{dc} along the a-axis. This TDTS data will then be combined with neutron data to extract the exchange interactions in a global fit, as discussed below.

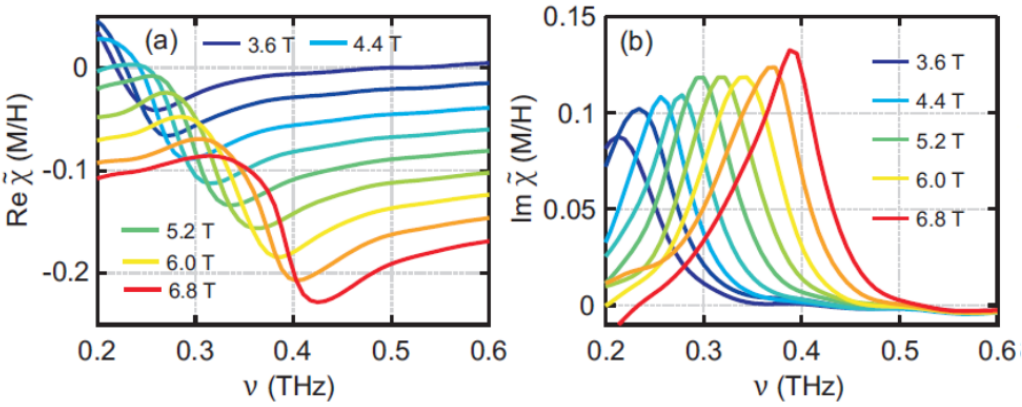

Figure 3.5: Real (a) and imaginary (b) parts of the magnetic susceptibility $\tilde{\chi}(\nu)$ for right-circularly polarized light at different fields $H_{dc} \parallel c$ at 5 K. $\tilde{\chi}(\nu)$ is obtained by referencing the TDTS data to the spectra at 100 K. Spectra in (a) are offset vertically by 0.02 for clarity.

3.3.3 Spin Wave Analysis

An effective spin-1/2 Hamiltonian relevant for $YbMgGaO_4$ has been given by [1, 13, 16, 83]:

$$\begin{aligned} H = \sum_{<i,j>} [\quad & J_1^{zz} S_i^z S_j^z + J_1^{\pm}(S_i^+ S_j^- + S_i^- S_j^+) \\ & + J_1^{\pm\pm}(\gamma_{ij} S_i^+ S_j^+ + \gamma_{ij}^* S_i^- S_j^-) \\ & - \frac{i J_1^{z\pm}}{2}(\gamma_{ij}^* S_i^+ S_j^z - \gamma_{ij} S_i^- S_j^z + \langle i \leftrightarrow j \rangle)] \\ + \sum_{\ll i,j \gg} [\quad & J_2^{zz} S_i^z S_j^z + J_2^{\pm}(S_i^+ S_j^- + S_i^- S_j^+)] \\ -\mu_0 \mu_B \sum [\quad & g_\perp (H^x S_i^x + H^y S_i^y) + g_\parallel H^z S_i^z] \end{aligned} \tag{3.1}$$

where $S^{\pm} = S^x \pm iS^y$, $g_{\parallel}$ and $g_{\perp}$ are components of the g-tensor parallel and perpendicular to the c-axis, complex numbers γ_{ij} are phase factors defined in [16] and brackets $<>$ and $\ll\gg$ represent nearest and next-nearest neighbor pairs respectively. The exchange interactions J^{zz} and $J^{\pm}$ originate from the standard XXZ model, with subscripts 1 and 2 indicating the nearest and next-nearest neighbor interactions respectively. We also include symmetry allowed bond-dependent interactions $J^{\pm\pm}$ and $J^{z\pm}$ (also known as pseudo-dipolar interactions), which have a spin-orbit origin. The pseudo-dipolar interactions between next-nearest neighbors are neglected since they are supposed to be small [100, 101] . Given the interactions are on the order of Kelvins, with moderate applied fields (>4T) in field-polarized state, the above Hamiltonian can be solved by linear spin wave theory to yield the spin wave dispersions for external fields along the c- and a-axis.

$$\begin{aligned} E_c(\mathbf{q}) &= \big\{[\mu_0\mu_B g_{\parallel} H^z - 3(J_1^{zz} + J_2^{zz}) \\ &+ 2\sum_{i=1}^{3} J_1^{\pm}\cos(\mathbf{q}\cdot\mathbf{a}_{1,i}) + 2\sum_{i=1}^{3} J_2^{\pm}\cos(\mathbf{q}\cdot\mathbf{a}_{2,i})]^2 \\ &- |\, 2J_1^{\pm\pm}\sum_{i=1}^{3}\gamma_{1,i}^{*}\cos(\mathbf{q}\cdot\mathbf{a}_{1,i})\,|^2\,\big\}^{1/2} \end{aligned} \tag{3.2}$$

$$
\begin{aligned}
E_a(\mathbf{q}) &= \big\{[\mu_0\mu_B g_\perp H^x - 6(J_1^\pm + J_2^\pm) \\
&+ \cos(\mathbf{q}\cdot\mathbf{a}_{1,1})(J_1^\pm + J_1^{zz}/2 - J_1^{\pm\pm}) \\
&+ \cos(\mathbf{q}\cdot\mathbf{a}_{1,2})(J_1^\pm + J_1^{zz}/2 + J_1^{\pm\pm}/2) \\
&+ \cos(\mathbf{q}\cdot\mathbf{a}_{1,3})(J_1^\pm + J_1^{zz}/2 + J_1^{\pm\pm}/2) \\
&+ \sum_{i=1}^{3}\cos(\mathbf{q}\cdot\mathbf{a}_{2,i})(J_2^\pm + J_2^{zz}/2)]^2 \\
&- |\cos(\mathbf{q}\cdot\mathbf{a}_{1,1})(J_1^\pm - J_1^{zz}/2 - J_1^{\pm\pm} + iJ_1^{z\pm}) \\
&\quad + \cos(\mathbf{q}\cdot\mathbf{a}_{1,2})(J_1^\pm - J_1^{zz}/2 + J_1^{\pm\pm}/2 - iJ_1^{z\pm}/2) \\
&\quad + \cos(\mathbf{q}\cdot\mathbf{a}_{1,3})(J_1^\pm - J_1^{zz}/2 + J_1^{\pm\pm}/2 - iJ_1^{z\pm}/2) \\
&\quad + \sum_{i=1}^{3}\cos(\mathbf{q}\cdot\mathbf{a}_{2,i})(J_2^\pm - J_2^{zz}/2)\,|^2\,\big\}^{1/2}
\end{aligned}
\tag{3.3}
$$

By setting $\mathbf{q} = 0$, we can obtain the spin wave excitations for the Faraday and Voigt geometry:

$$E(H^z) = \mu_0\mu_B g_\parallel H^z - 3(J_1^{zz} + J_2^{zz}) + 6(J_1^\pm + J_2^\pm) \tag{3.4}$$

$$
\begin{aligned}
E(H^x) &= \{[\mu_0\mu_B g_\perp H^x + \frac{3}{2}(J_1^{zz} + J_2^{zz}) - 3(J_1^\pm + J_2^\pm)]^2 \\
&- |\,\frac{3}{2}(J_1^{zz} + J_2^{zz}) - 3(J_1^\pm + J_2^\pm)\,|^2\}^{\frac{1}{2}}.
\end{aligned}
\tag{3.5}
$$

According to Eq. 3.4, the field dependence in the Faraday geometry is particularly simple and depends only on $g_\parallel$. From a simple linear fit to the data in Fig. 3.6 (a) we obtain $g_\parallel = 3.81(4)$. Note that the effective g-tensor here is a property of a single Yb^{3+} ion and as such is independent of the exchange inter-

actions [90]. This allows us to treat $g_{\parallel}$ as a fixed parameter in the subsequent global fit. In contrast, $E(H^x)$ is not linearly related to $g_{\perp}$ (Eq. 3.5) and so $g_{\perp}$ must be extracted simultaneously with the exchange constants. One expects the present measurements of the *g*-factor to be considerably more accurate than previous X-band ESR results [16] due to greater than a ten-fold increase in the magnitude of the magnetic fields.

3.3.4 Global Fit

Now we perform a global fit to determine the exchange interactions accurately. We have the spin wave excitations data with field along a-axis (Fig. 3.6 (f)) and c-axis (Fig. 3.6 (c)-(e)) obtained through INS as well as the TDTS data in Faraday (Fig. 3.6 (a)) and Voigt (Fig. 3.6 (b)) geometry. The entire dataset is fit simultaneously to the spin-wave dispersions Eq. 3.2-3.5 in the field-polarized state obtained from the spin Hamiltonian in Eq. 3.1. There are six target parameters for this global fit, which are J_1^{zz}, $J_1^{\pm}$, $J_1^{\pm\pm}$, $|J_1^{z\pm}|$, the ratio J_2/J_1 and $g_{\perp}$ with a fixed $g_{\parallel} = 3.81$. As spin-space anisotropy is primarily a property of the effective spin-1/2 doublet of Yb^{3+}, we adopt the same overall XXZ exchange anisotropy for both nearest neighbor and next-nearest neighbor interactions, *i.e.* $J_2^{zz}/J_2^{\pm} = J_1^{zz}/J_1^{\pm}$. This reasonable assumption helps in reducing the size of the parameter space for the global fit.

We obtain an excellent fit to the data as shown in Fig. 3.6. Fig. 3.7 (a)

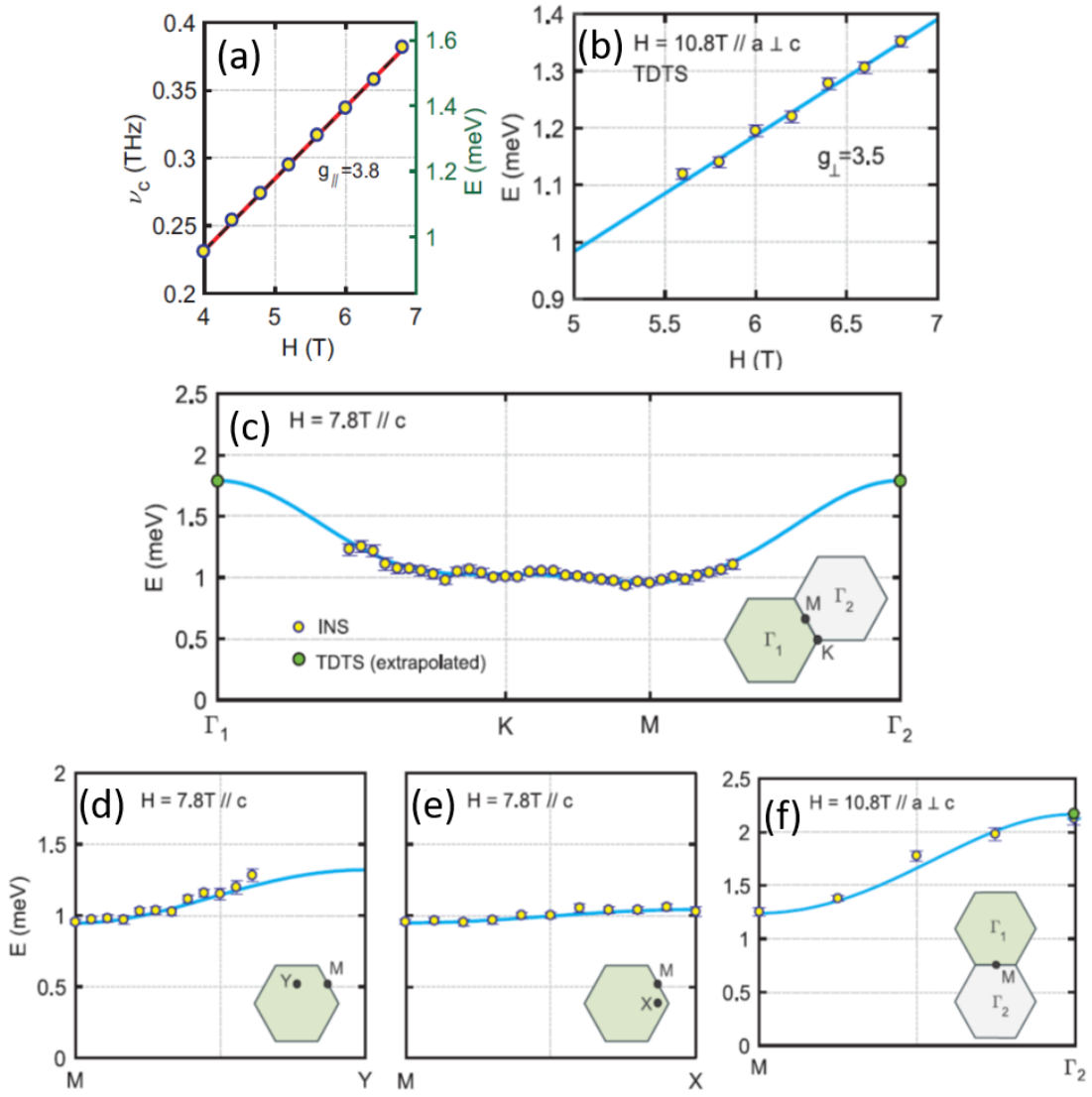

Figure 3.6: (a)) Resonant frequency of spin wave versus magnetic field in Faraday geometry. (b) Resonant frequency of spin wave versus magnetic field in Voigt geometry. (c)-(e) Energy dependence of spin-wave excitations in the field-saturated state from INS data along high symmetry directions of the triangular Brillouin zone with external field along c-axis. (f) Energy dependence of spin-wave excitations along high symmetry direction with field along a-axis. The solid lines are fitting curve.

with the data and calculation lying on top of each other also indicates the good agreement between the fitting and the data. Our global fitting parameters are

shown in Tab. 3.1 (Model C). We note that the above fit is performed with some physical constraint, e.g., $|J_1^{zz}| > |J_1^{z\pm}|$. Without this, we obtain $|J_1^{z\pm}| = 0.45$ which we regard as unphysical as it is nearly three times larger than J_1^{zz}.

In previous works, two different sets of parameters have been proposed for the exchange interactions of $YbMgGaO_4$. The first set [1], model A in Tab. 3.1, includes both nearest and next-nearest neighbor interactions but sets $J_1^{z\pm} = 0$ based on previous X-band ESR results [16]. The second set [2], model B in Tab. 3.1, includes only nearest-neighbor interactions, with the $J_2 = 0$ constraint argued as a consequence of the localized nature of Yb^{3+} $4f$ electrons [2, 96]. Both models used the *g*-factors determined from low frequency X-band ESR. Model C is the new best fit from our spin-wave analysis. The experimental *vs.* calculated spin-wave energies for each of model A, B and C are shown in Fig. 3.7 (a) for comparison. Clearly, the points obtained for our model C lie significantly closer to the $E_{exp} = E_{calc}$ line than models A and B, highlighting the advantage of our enriched datasets over previous works.

Our global analysis yields finite NNN interactions with $J_2/J_1 = 0.18(7)$ and a slightly sub-dominant pseudo-dipolar $J_1^{\pm\pm} \approx 0.07meV$ interaction. The large fitting error bars on some parameters of the model reveal the high degree of correlation between J_2 and $J_1^{\pm\pm}$ and the very weak sensitivity of our fit to $|J_1^{z\pm}|$. As shown in Fig. 3.7 (b) and (c), this is apparent in the χ^2 goodness of fit 2D plots in the parameter spaces of $J_1^{\pm\pm}$ versus $|J_1^{z\pm}|$, and $J_1^{\pm\pm}$ versus J_2/J_1, respec-

Model	A	B	B*	C
J_1^{zz} (meV)	0.126	0.164	0.151(5)	0.149(5)
$J_1^{\pm}$ (meV)	0.109	0.108	0.088(3)	0.085(3)
$J_1^{\pm\pm}$ (meV)	0.013	0.056	0.13(2)	0.07(6)
$\lvert J_1^{z\pm}\rvert$ (meV)	0	0.098	0.1(1)	0.1(1)
J_2/J_1	0.22	0	0	0.18(7)
$g_{\parallel}$	3.72	3.72	3.81(4)	3.81(4)
$g_{\perp}$	3.06	3.06	3.53(5)	3.53(5)

Table 3.1: Exchange parameters for different models derived from fitting the spin-wave dispersions. Models A and B are from [1] and [2], respectively. Model C is from our global fit to the TDTS and INS data. Model B* is from a global fit to the data by ignoring NNN interactions, *i.e.* $J_2 = 0$. Uncertainties in the values represent the 99.7% confidence interval (3 s.d.) in extracting the fitting parameters. Note that we think that the best fits are in fact given with a refined model C* given later in the chapter.

tively.

Given the correlation between $J_1^{\pm\pm}$ and J_2, it is natural to analyze how our results change by enforcing the constraint $J_2 = 0$ while leaving all other parameters free. This leads to model B*, which resembles model C except for a larger $J_1^{\pm\pm} = 0.13(2)$ which is now comparable to the dominant J_1^{zz} exchange (see Tab. 3.1). This model gives only a slightly worse fit to the spin-wave data than model C as shown in Fig. 3.7 (a). While a unique set of exchange parameters cannot be obtained from the above analysis, a definitive hierarchy of interactions nevertheless emerges. It yields easy-plane XXZ terms for $YbMgGaO_4$ with $J_1^{zz} = 0.15(1)meV$, $\Delta = J_1^{zz}/2J_1^{\pm} = 0.9(1)$, a subleading pseudo-dipolar term $J_1^{\pm\pm}/J_1^{zz} \leq 1$ and a small NNN exchange $J_2^{zz} = 0.03(1)meV$.

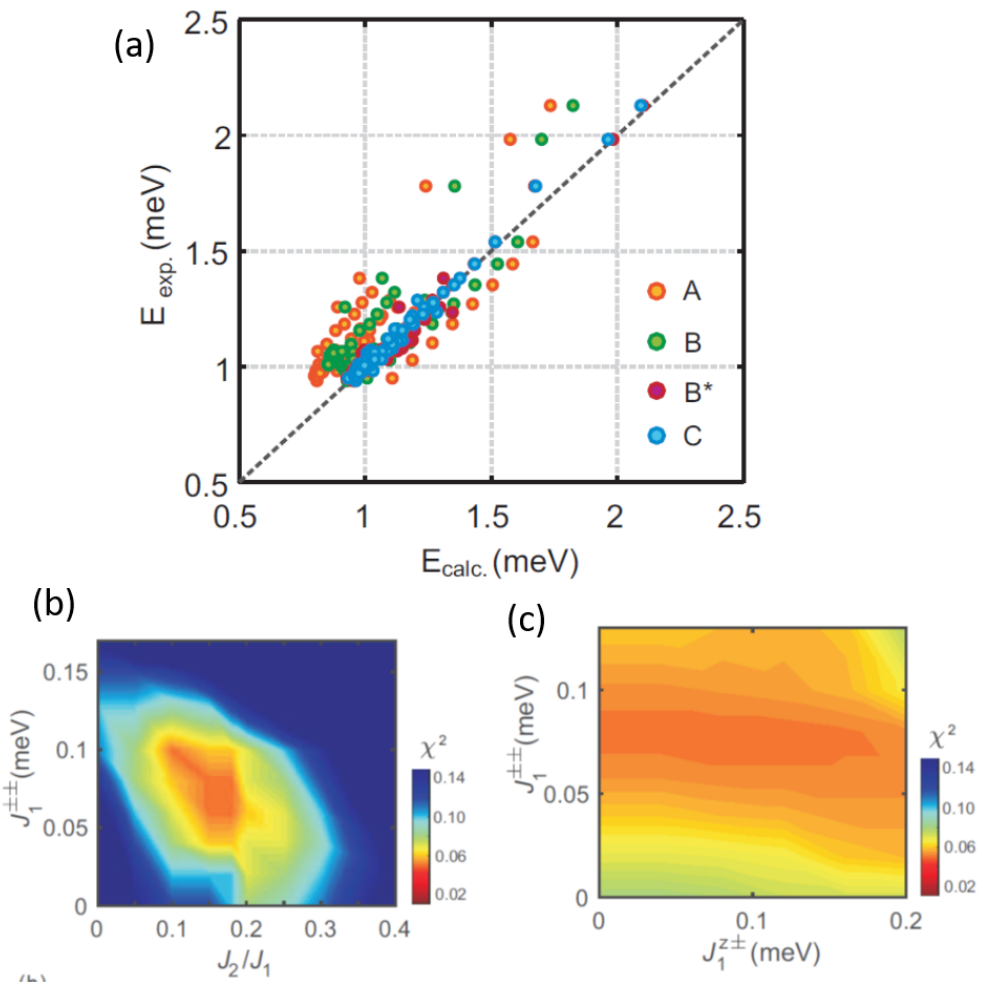

Figure 3.7: (a) Experimental *vs.* calculated spin-wave energies, where the dashed line denotes $E_{exp} = E_{calc}$. Fitted exchange parameters for models A, B, and C are listed in Tab. 3.1. Model A (Ref. [1]), B (Ref. [2]), and C (global fit to the TDTS and INS data) are represented by orange, green and blue symbols, respectively. Model B* (global fit to data under the $J_2 = 0$ constraint) is represented by pink symbols. (b) χ^2 goodness of fit 2D plots of $J_1^{\pm\pm}$ versus $|J_1^{z\pm}|$ and (c) $J_1^{\pm\pm}$ versus J_2/J_1.

3.3.5 Further constraints: TDTS lineshapes

To further constrain the pseudo-dipolar interactions, we analyzed the linewidths of the spin-wave peaks in the TDTS data of Fig. 3.5 (b). As noted above,

TDTS functions here as high-field ESR [86]. ESR linewidths are strongly sensitive to the magnitude of the off-diagonal anisotropic interactions $J_1^{\pm\pm}$ and $J_1^{z\pm}$ of our model. The analysis proceeds using the formalism of Kubo-Tomita [16, 102, 103] which relates the width of the ESR absorption line to commutators that depend only on the anisotropic exchange interactions. This perturbative result is valid for small anisotropic exchanges when temperature and magnetic field are larger than the dominant exchange, conditions that are realized in our high-field TDTS experiments. The Lorentzian width can be expressed by $\Delta_{cal} = \sqrt{2\pi M_2^3/M_4}$, where M_2 and M_4 are the second and fourth moment of the anisotropic part of the Hamiltonian with full expression in [16].

Here we use this formalism to show that the observed spin-wave linewidths cannot be reconciled with the large anisotropic exchange terms suggested by model B* and therefore J_2 must be non-zero. In Fig. 3.8, we plot the deviation between the calculated and the experimental spin-wave resonance linewidths in both the Faraday Δ_f and Voigt Δ_v geometry as a function of $|J_1^{z\pm}|$ and $|J_1^{\pm\pm}|$ defined by $R_p = \frac{1}{2}[|\ \frac{\Delta_f - \Delta_{cal}}{\Delta_f}\ | + |\ \frac{\Delta_v - \Delta_{cal}}{\Delta_v}\ |]$. We analyze the case of $J_2 = 0$ that is relevant for model B*. Fig. 3.8 shows the deviation is minimal along the yellow contour, so that $\sqrt{|J_1^{z\pm}|^2 + |J_1^{\pm\pm}|^2} \approx 0.04(1)$. This calculation assumes that all the broadening of the THz data comes from exchange anisotropy with no other contributions. But a distribution of g-factors or disorder may also broaden the linewidths. In fact a broad distribution of g factor $\Delta g_{\|}/\bar{g_{\|}} \approx 0.3$ and $\Delta g_{\perp}/\bar{g_{\perp}} \approx 0.1$,

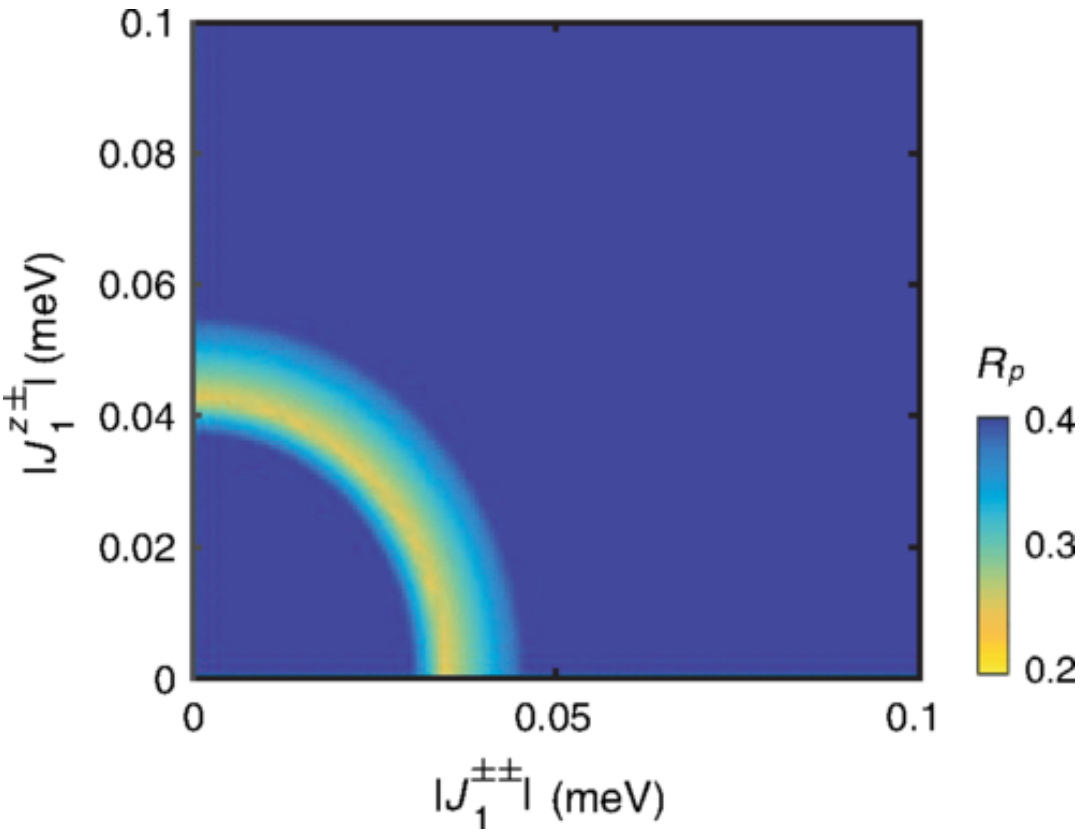

Figure 3.8: Deviation R_p of the experimental TDTS spin-wave resonance linewidths from the theoretically calculated ones as a function of the pseudo-dipolar interactions $|J_1^{z\pm}|$ and $|J_1^{\pm\pm}|$. This sets an upper bound on the pseudo-dipolar interactions in a model with $J_2 = 0$.

has been demonstrated by a neutron analysis of CEF excitations linewidths [95], so it must also play a role in the lineshapes observed here. Our analysis of the high-field TDTS lineshapes therefore provides an upper bound on any off-diagonal anisotropic exchanges $|J_1^{z\pm}|$ and $|J_1^{\pm\pm}|$. The parameters determined in model B* are incompatible with this bound and so model B* is ruled out as a realistic description of the exchange parameters of $YbMgGaO_4$, hence J_2 must be considered to account for our data.

Taken together, our results strongly favor an easy-plane XXZ scenario for $YbMgGaO_4$ with the combination of finite J_2 and relatively small pseudo-dipolar exchanges. Thus, the refinement of model C with a range of best possible parameter values we found for $YbMgGaO_4$ can be summarized as a model C*:

$$J_1^{zz} = 0.149(5)\ \text{meV}, \quad J_1^{\pm} = 0.085(3)\ \text{meV},$$
$$J_2/J_1 = 0.18(7), \quad \sqrt{|J_1^{\pm\pm}|^2 + |J_1^{z\pm}|^2} < 0.05\ \text{meV}.$$

3.4 Conclusion

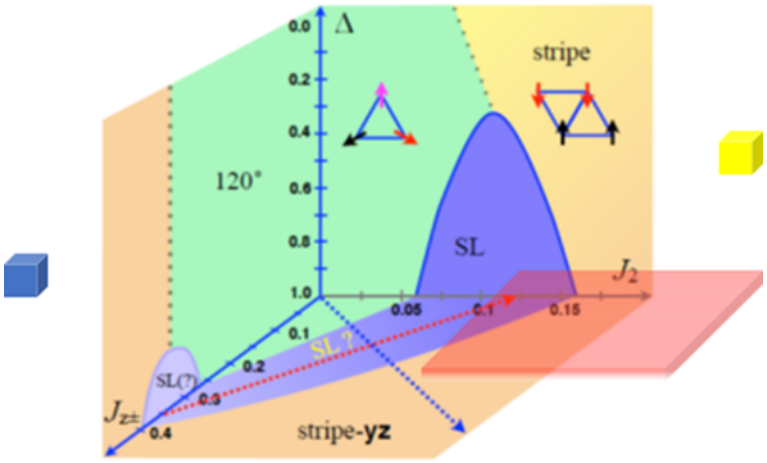

Figure 3.9: Diagram illustrating theoretically predicted magnetic phases in $YbMgGaO_4$ as a function of various exchange interactions. Yellow and blue cubes represent the models A and B, respectively. The red region indicates our current parameters i.e., $YbMgGaO_4$ is closer to the spin liquid phase than previously believed. The Figure is adapted from Ref. [17].

In summary, we combined THz spectroscopy and neutron scattering and

perform a global fit to determine the exchange interactions as well as g-factors. With further THz linewidth analysis, we are able to constrain the anisotropic terms $|J_1^{z\pm}|$ and $|J_1^{\pm\pm}|$ and provide a set of most accurate exchange parameters so far. With the less accurate parameters obtained in previous works [1, 2], it seemed $YbMgGaO_4$ should lie in the ordered state far away from spin liquid regime in the phase diagram [17]. However, our results place the $YbMgGaO_4$ much closer to the spin liquid regime in the phase diagram as shown in Fig. 3.9. Despite the existence of the site mixing disorder between Mg^{2+} and Ga^{3+} ions, $YbMgGaO_4$ is still a good quantum spin liquid candidate due to competition between the various exchange interactions. It would be interesting if less disordered versions of this material could be prepared.

Chapter 4

Low Energy Magneto-optics of $Tb_2Ti_2O_7$ in [111] Magnetic Field

The pyrochlore magnet $Tb_2Ti_2O_7$ attracts attention for decades and is considered to be a quantum spin liquid candidate. We perform time-domain THz spectroscopy on high quality $Tb_2Ti_2O_7$ crystals and study the low energy crystal field excitations as a function of [111] magnetic field with high energy resolution.We observed several crystal field anomalies at 3 T. Despite several sharp field dependent features, we show that the material's spectrum can be described by field dependent hybridization between the low energy crystal field levels instead of a structural phase transition. A field independent crystal field calculation cannot reproduce the data quantitatively, indicating a field dependent crystal field environment. We highlight the strong coupling between spin

and lattice degrees of freedom in $Tb_2Ti_2O_7$ as evidenced by the magnetic field tunable crystal field environment. The theoretical work in this chapter was done in close collaboration with Yi Luo.

4.1 Introduction to $Tb_2Ti_2O_7$

4.1.1 Spin Liquid Candidate

Rare earth pyrochlores with corner sharing tetrahedra of magnetic ions have strong geometric frustrations. They have been subjects of intense interest for years [58, 104]. Famous examples include canonical spin ice compound $Dy_2Ti_2O_7$ and $Ho_2Ti_2O_7$, where at low temperature spins follow a two-in-two-out "ice rule" on the tetrahedra and the low energy magnetic excitations are magnetic monopoles connected by a Dirac string [6, 7, 59, 105]. It was believed that $Tb_2Ti_2O_7$ and $Yb_2Ti_2O_7$ may be a quantum spin ice (QSI) with transverse Ising component to enhance quantum fluctuations, thereby a QSL candidate [19, 32, 91, 106]. However, recently experiments on high quality single crystals $Yb_2Ti_2O_7$ suggest the ground state is ferromagnetic long range order with short range anti-ferromagnetic correlation [33, 34, 107]. Unlike $Yb_2Ti_2O_7$ that orders at 270 mK, $Tb_2Ti_2O_7$ shows no magnetic order down to 50 mK despite an anti-ferromagnetic Curie-Weiss temperature $\theta_{CW} \approx 19$ K [18, 108].

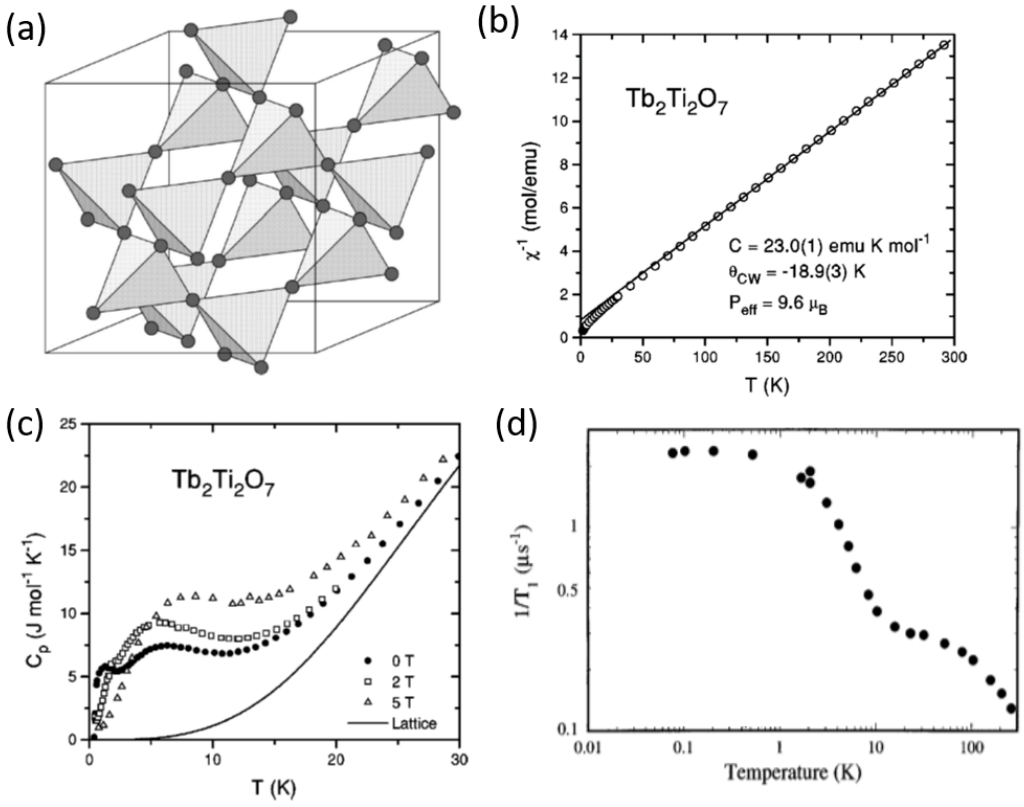

Figure 4.1: (a) Pyrochlore structure composed of corner sharing tetrahedra. (b) Magnetic susceptibility measurements show no magnetic order down to 50 mK despite an anti-ferromagnetic Curie-Weiss temperature $\theta_{CW} \approx 19$ K. (c) Specific heat measurements show no signatures for phase transition. (d) μSR shows persistent spin fluctuations down to 70 mK. Figures are from Ref. [18,19]

Neutron scattering shows power law correlations [109], that bear resemblance to the pinch points found in classical spin ice. μSR shows persistent spin fluctuations down to 70 mK with a relaxation rate 0.04 THz, supporting spin liquid behavior [19].

$Tb_2Ti_2O_7$ is unique among the pyrochlore titanate family for two reasons. One is that there are particularly low energy crystal electric field levels (CEF)

and the other is the existence of a strong spin-lattice coupling, both of which may be important for the spin liquid physics.

4.1.2 Low Energy Electric Crystal Field

Tb^{3+} is a rare earth element. Its spin-orbit coupling is stronger than crystal electric field effects. There are 8 f (f^8) electrons in each Tb^{3+} and based on Hund's rule we have L=3 S=3 J=6, which is represented by ${}^7F_6$. Therefore, by considering the spin-orbit coupling, the ground state has 13 fold degeneracy within the J=6 manifold. The trigonal symmetry CEF acting on the Tb^{3+} ion will further split the 13 fold degenerate state, leading to a low energy first excited doublet that is separated from the ground state doublet only by $\Delta \sim 0.4$ THz (1.6 meV) [3,18,110–112]. This is in contrast to other pyrochlore titanates, where the lowest excited CEF level is well isolated from the ground state [18].

The low energy crystal field may have important consequences. It is proposed that the virtual CFE renormalize the anti-ferromagnetic exchange interactions to ferromagnetic interactions and give rise to transverse component as a route to quantum spin ice [113]. Due to the low energy crystal field, theory based on ground state is insufficient to explain the magnetic properties in $Tb_2Ti_2O_7$. An upper branch magnetism including the hybridization between ground state and first excited states have been proposed for $Tb_2Ti_2O_7$ to account for spin liquid physics [114].

4.1.3 Spin Lattice Coupling

The second unique feature in $Tb_2Ti_2O_7$ is the strong spin-lattice coupling. Because Tb^{3+} is a non-Kramers ion, $Tb_2Ti_2O_7$ is susceptible to distortions. Although the presence of static distortions have been debated [115–118], many experiments have demonstrated the strong coupling between spin and lattice degrees of freedom as shown in Fig. 4.2. Here, x-ray scattering in zero magnetic field shows substantial broadening and peak intensity reduction of structual Bragg peaks below 20 K, indicating dynamic structural fluctuations [20]. X-ray experiments with pulsed magnetic field observed a structural phase transition from cubic to tetragonal or orthorhombic symmetry at 29 T [21]. A giant magnetostriction has also been reported [22]. Neutron scattering discovered the excited crystal field level is coupled to a transverse acoustic phonon, forming a hybrid excitation between the CEF levels and the transverse phonon [23, 119, 120]. All of above experiments suggest the important role of the lattice in the magnetic behaviors of $Tb_2Ti_2O_7$ and imply a strong coupling between spin and lattice degree of freedom.

4.1.4 A Potential Structure Phase Transition

Recently, Raman scattering measurements have reported anomalous CEF excitations with [111] magnetic field, including a splitting of CEF, non-linear

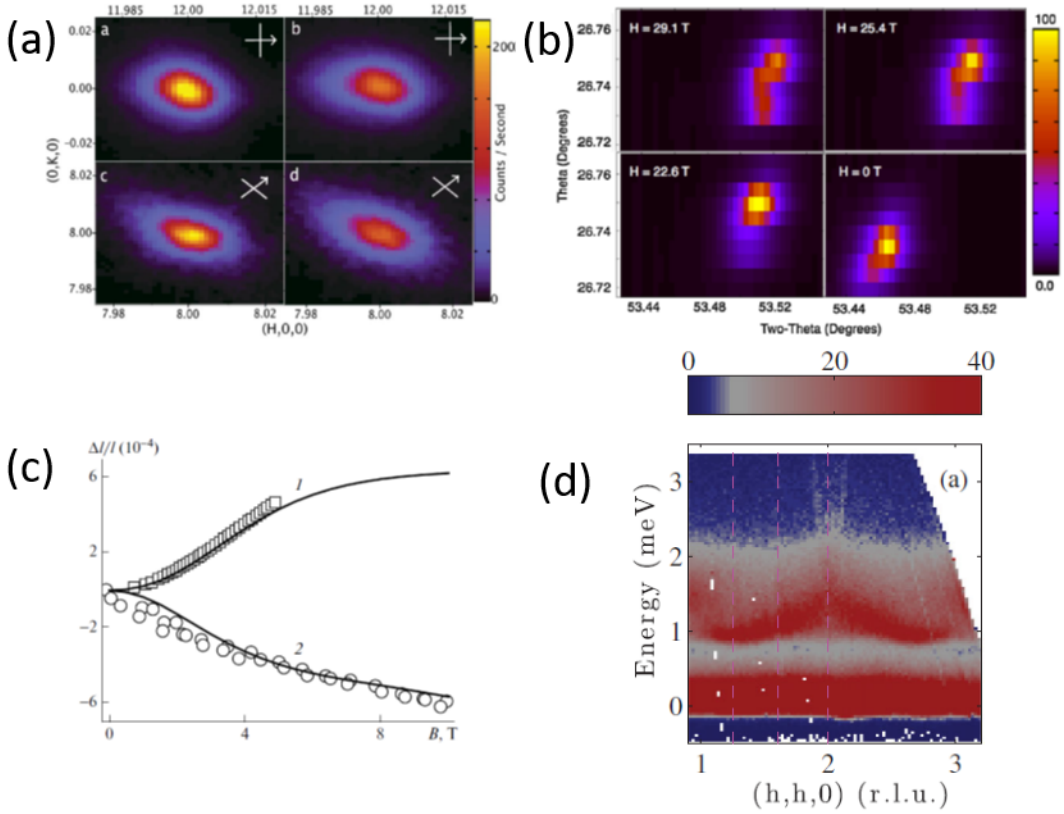

Figure 4.2: (a) Dynamic structural fluctuations are visualized by x-ray scattering in zero field with cooling down to low temperature. (b) X-ray experiments with pulsed magnetic field observed a structural phase transition from cubic to tetragonal or orthorhombic symmetry at 29 T. (c) Giant magnetostriction with magnetic field applied along [111] for squares and [110] for circles. (d) Magnetoelastic modes, which are hybridization between CEF and a transverse phonon, are observed by neutron scattering. Figures are from Ref. [20–23]

field dependence and the emergence of a new excitation, which have been interpreted as a structural phase transition at ∼2.5 T originated from a oxygen displacement as shown in Fig. 4.3. They proposed that the magnetic field in [111] direction brings out the "3 in 1 out" magnetic monopole configuration and induced the structural phase transition and electric dipoles [24]. However, the

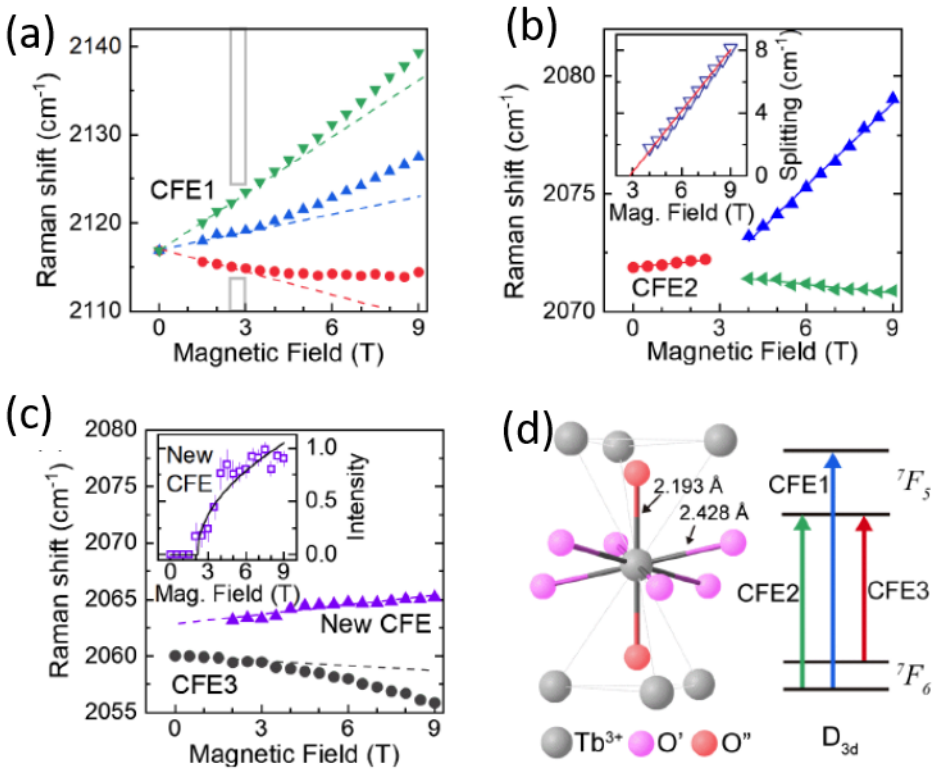

Figure 4.3: A few CEF anomalies observed by Raman scattering. (a) Raman scattering shows non-linear field dependence of CEF. (b) A splitting of CEF at 3 T. (c) Emergence of a new CEF at 3 T. (d) Local geometry around the Tb ions along with the transitions between different crystal-field energy levels. Figures are from Ref. [24].

Raman scattering focused on high energy and it was difficult to assign the observed CEF excitations to specific CEF transitions, therefore it is not possible to do a comparison between experiment and theory [24]. In contrast, TDTS can measure low energy CEF precisely and we will show the observed CEF anomalies can be explained by low energy CEF hybridization instead of a structural phase transition.

4.2 Results

4.2.1 Crystal Field Excitations in Circular Basis

TDTS measurements were performed on high quality single crystals $Tb_2Ti_2O_7$ grown by traveling solvent floating zone method. $Tb_2Ti_2O_7$ was measured down to 1.6 K with external fields up to 6.9 T in the Faraday ($\mathbf{k} \parallel \mathbf{H_{dc}}$) geometry, where k is the direction of light propagation. The circular basis are eigenpolarization for transmission in a cubic lattice under magnetic field. The complex transmission in the Faraday geometry in the linear basis can be converted to the circular basis via the expression $T_{R,L} = T_{xx} \pm iT_{xy}$ as described in the preceding chapter. Fig 4.4 show transmission magnitudes as a function of frequency and magnetic field for left and right circularly polarized THz light. It is amazing to see a number of excitations appearing in both left and right channels. The excitations are seen as bright yellow features, which correspond to CEF excitations and follows optical selection rules.

The observed excitations are expected to originate from transitions from the ground state doublet (G_1 and G_2) to the first excited state doublet (E_1 and E_2), as higher excited states are at much larger energies [3, 110–112]. In zero magnetic field, in the basis of $|m\rangle$=$|J$=6; J_z=$m\rangle$ the wavefunction of the ground state doublet is approximately $\psi_{G_{1,2}} \approx a_G|\pm 4\rangle \pm b_G|\mp 5\rangle$ and the first excited state is approximately $\psi_{E_{1,2}} \approx a_E|\pm 5\rangle \pm b_E|\mp 4\rangle$. Applying magnetic field along [111],

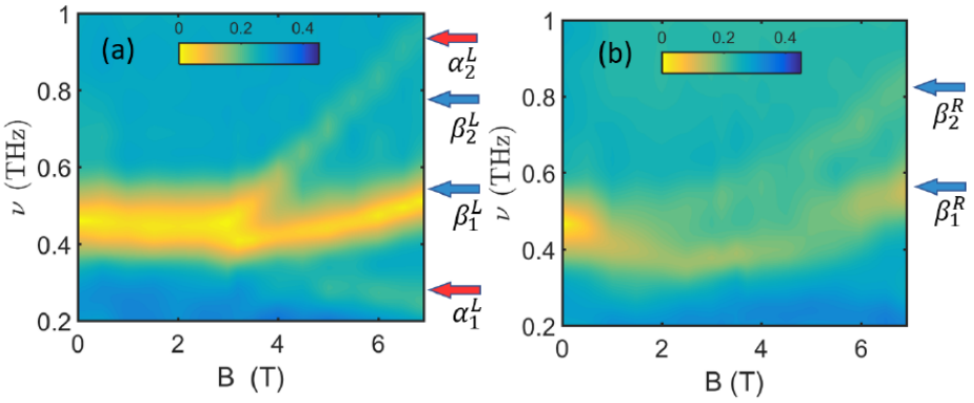

Figure 4.4: Transmission amplitude for (a) left and (b) right circularly polarized THz light as a function of frequency and magnetic field up to 6.9 T at 1.6 K. Four excitations are observed in left channel indicated by α_1^L, β_1^L,β_2^L, α_2^L and two excitations in right channel indicated by β_1^R and β_2^R.

the ground and first excited state doublets split. Because the experiments were performed at 1.6 K ($\approx$ 0.03 THz and 0.13 meV) the thermal population of all higher levels in high field are negligible and hence only the transitions starting from the ground state G_1 are important. There are two distinct Tb sites (α and β) differentiated by their alignment to the [111] field as shown in Fig. 4.5. Hence, there are 6 different transitions expected, but in experiment not all of them can be seen due to optical selection rules, experimental resolution and limited THz range, etc. We observed four features in the left channel Fig. 4.4 (a) labelled as (α_1^L, β_1^L, β_2^L, α_2^L) and two in the right channel Fig 4.4 (b) labelled as (β_1^R, β_2^R).

There are a number interesting features in the spectrum. As discussed

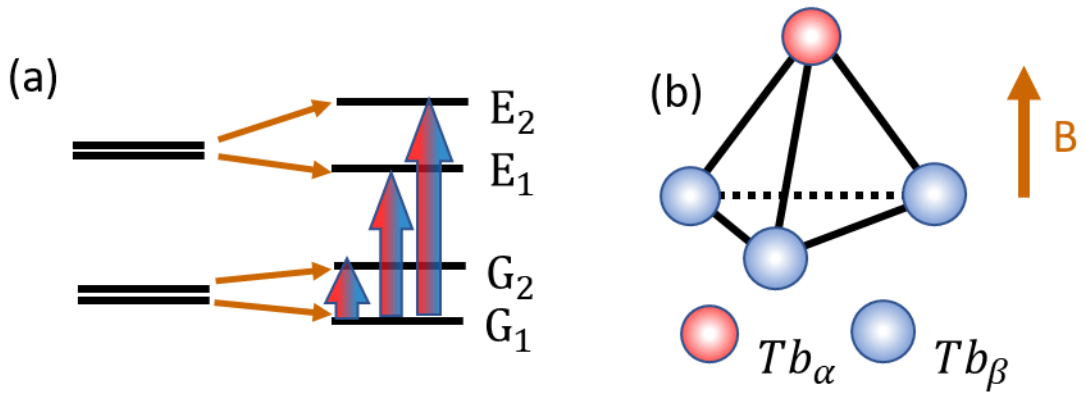

Figure 4.5: (a) The schematic of CEF splitting in magnetic field labelled as G_1, G_2, E_1 and E_2. The red and blue arrows indicate transitions at two different sites α and β. (b) A tetrahedron with red and blue spheres represent the two different Tb ions under [111] magnetic field.

below, features β_1^L/ β_1^R and β_2^L/β_2^R correspond to the same transitions, which appears in both channels, while α_1^L and α_2^L only appear in the L channel. This is because of selection rules for Tb_α and Tb_β individually. Other notable aspects of the data include an almost constant CEF excitation α_2^L up to 3 T, which then changes its behavior abruptly near 3 T, a behavior that is in stark contrast to the common Zeeman splitting; and a seemingly "new" excitation α_1^L that shows increasing intensity with magnetic field.

4.2.2 Field Independent Crystal Field Calculation

To gain further insight on this data, we performed crystal field calculations based on single ion physics for D_{3d} point symmetry for Tb^{3+}. The effective Hamiltonian in terms of Stevens operators O_k^q, which applies for a basis comprised of a single J level (J=6 for Tb^{3+}) in the LS coupling scheme, is

$$H_{CEF} = \theta_2 D_2^0 O_2^0 + \theta_4 D_4^0 O_4^0 + \theta_4 D_4^3 O_4^3 + \theta_6 D_6^0 O_6^0 + \theta_6 D_6^3 O_6^3 + \theta_6 D_6^6 O_6^6, \quad (4.1)$$

where O_k^q are the Stevens operators and θ_k are the reduced matrix elements: θ_2 = -1/99, θ_4 = 2/16335 and θ_6 = -1/891891. D_k^q and B_q^k are related by $D_k^q = \lambda_k^q B_q^k$, where $\lambda_2^0 = 1/2$, $\lambda_4^0 = 1/8$, $\lambda_4^3 = -\sqrt{35}/2$, $\lambda_6^0 = 1/16$, $\lambda_6^3 = -\sqrt{105}/8$, $\lambda_6^6 = \sqrt{231}/16$ [111]. Crystal field parameters B_q^k can then be obtained by fitting to lowest 13 neutron crystal field energies at zero field [3]. The lowest 13 CEF energy levels we used are the following: 0, 0, 1.9, 1.9, 10.4, 16.2, 44.1, 45.3, 45.7, 45.7, 62.9, 62.9, 69.8 meV. Note there are slight modifications of these numbers from the accepted values: the k averaged lowest excitation 1.6 meV was replaced by 1.9 meV at Γ point as observed in THz spectroscopy; the doublet at 44.1 meV is corrected by a doublet at 45.7 meV as confirmed by the

	B_0^2	B_0^4	B_3^4	B_0^6	B_3^6	B_6^6
This work	52.2	302.0	129.3	65.6	-31.5	149.8
From LS refined data [3]	55.9	310	114	64.6	-84.5	129

Table 4.1: Steven operators parameters (meV) B_q^k obtained in this work and [3] in LS coupling scheme.

authors in Ref. [3]. The obtained B_q^k are listed in Tab. 4.1 and are close to previous works. B_q^k from Ref. [3] are also listed in Tab. 4.1 for comparison.

In order to account for the evolution of crystal field excitations as function of magnetic field, we include a Zeeman term

$$H_{Zeeman} = -\mu_B g_J \vec{B} \cdot \vec{J}, \tag{4.2}$$

where μ_B is Bohr magneton and Landé $g_J = 1.5$ for $Tb_2Ti_2O_7$. By diagonalizing the Hamiltonian $H = H_{CEF} + H_{Zeeman}$, we obtain the eigenenergies and eigenfunctions at each magnetic field.

Since the magnetic field needs to be projected along local [111] direction, we need to do the calculation for Tb_α and Tb_β separately because the Zeeman term is different for each due to relative orientation of the field with respect to local [111] axis. We have $H^\alpha_{Zeeman} = -\mu_B g_J B J_z$ and $H^\beta_{Zeeman} = -\mu_B g_J (B J_x \sin\theta - B J_z \cos\theta)$, where θ is the bond angle $\sim 109.5°$.

We plot the field evolution of the four lowest energy levels for Tb_α and Tb_β as shown in Fig. 4.6 (a) and (b), respectively. The transitions between different

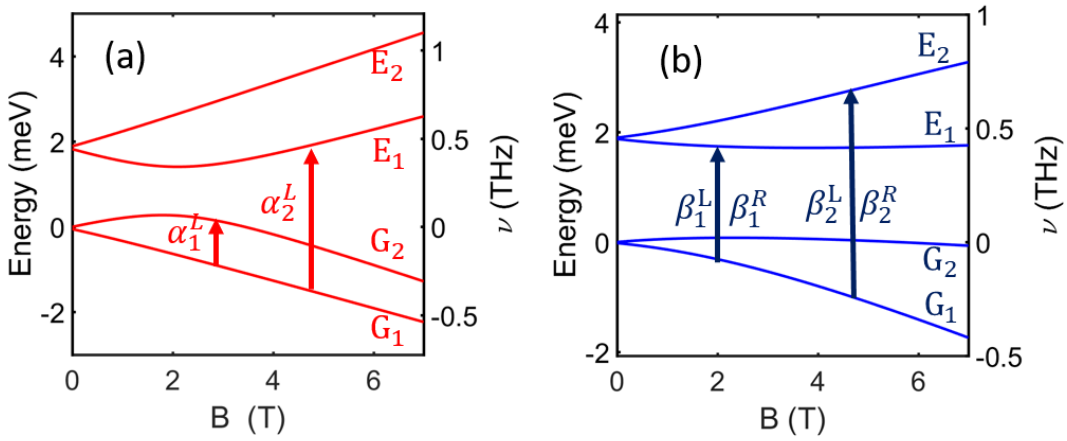

Figure 4.6: (a) Calculated energy of four lowest crystal field as a function of field for Tb$_\alpha$. The observed excitations α_1^L and α_2^L correspond to transition $G_1 \rightarrow G_2$ and $G_1 \rightarrow E_1$ of Tb$_\alpha$. (b) Calculated energy of four lowest crystal field as a function of field for Tb$_\beta$. The observed excitations β_1^L,β_1^R and β_2^L,β_2^R correspond to transition $G_1 \rightarrow E_1$ and $G_1 \rightarrow E_2$ of Tb$_\beta$, respectively.

states correspond closely to experimentally observed excitations. We can relate the observed excitations to calculation based on optical selection rules and calculated wave-functions. The CEF excitations couple to the magnetic field of the THz pulse. The general selection rule for magnetic dipole excitations is $\Delta m = 0, \pm 1$ and $\Delta J = 0, \pm 1$ with no parity change. Since both the ground and first excited doublets have E_g, the requirement of no parity change is already satisfied. In the Faraday geometry with J=6 for Tb^{3+}, because of the conservation of angular momentum, excitations with $\Delta m = +1, -1$ should be seen in left and right channels, respectively. $\Delta m = 0$ is forbidden in the Faraday geometry. Based on selection rules, the transition $G_1 \rightarrow G_2$ and $G_1 \rightarrow E_1$ for Tb$_\alpha$ have $\Delta m = +1$ and should only be seen in the left channel as α_1^L and α_2^L. $G_1 \rightarrow$

E_2 has $\Delta m = 0$, thus cannot be seen in either left or right channels for Tb_α. On the contrary, for Tb_β where the field is not along the local [111] direction and transverse components of the field makes the wavefunction a mix of $|\pm 4\rangle$ and $|\pm 5\rangle$. As a result, transitions at the β sites composed of $\Delta m = \pm 1$ can be seen in both left and right channel. As shown in Fig. 4.4, $G_1 \rightarrow E_1$ are observed as β_1^L and β_1^R in left and right channel with similar energies but different intensities. $G_1 \rightarrow E_2$ are observed as β_2^L and β_2^R.

The transition intensity can also be calculated. According to Fermi's golden rule, the intensity should be proportional to the transition amplitude given by $I_{i\rightarrow j} \sim \frac{2\pi}{\hbar}\langle i|H^{'}|j\rangle^2$. Here $H^{'} = \vec{B_{ac}} \cdot \vec{J}$ is the time dependent perturbation from coupling between the ac magnetic field of THz pulses and magnetic dipole in $Tb_2Ti_2O_7$. In the Faraday geometry ($k \parallel H$) along [111] direction, where k is the direction of light propagation, the transition matrix element $\langle i|H^{'}|j\rangle$ becomes $\langle i|B_{ac}J_x|j\rangle$ with $J_x = (J_+ + J_-)/2$, hence, the optical selection rule is $\Delta m = +1$ for left and $\Delta m = -1$ for the right circular basis. Considering that we are at finite temperatures (1.6 K), the transition amplitude needs to be modified by the Boltzmann distribution. Therefore, we have

$$I_{i\rightarrow j} \sim |\langle i|J_\pm|j\rangle|^2 \frac{exp[-E_i/k_BT]}{\sum_j exp[-E_j/k_BT]}. \tag{4.3}$$

J_+ and J_- are used for left and right circular transition, respectively.

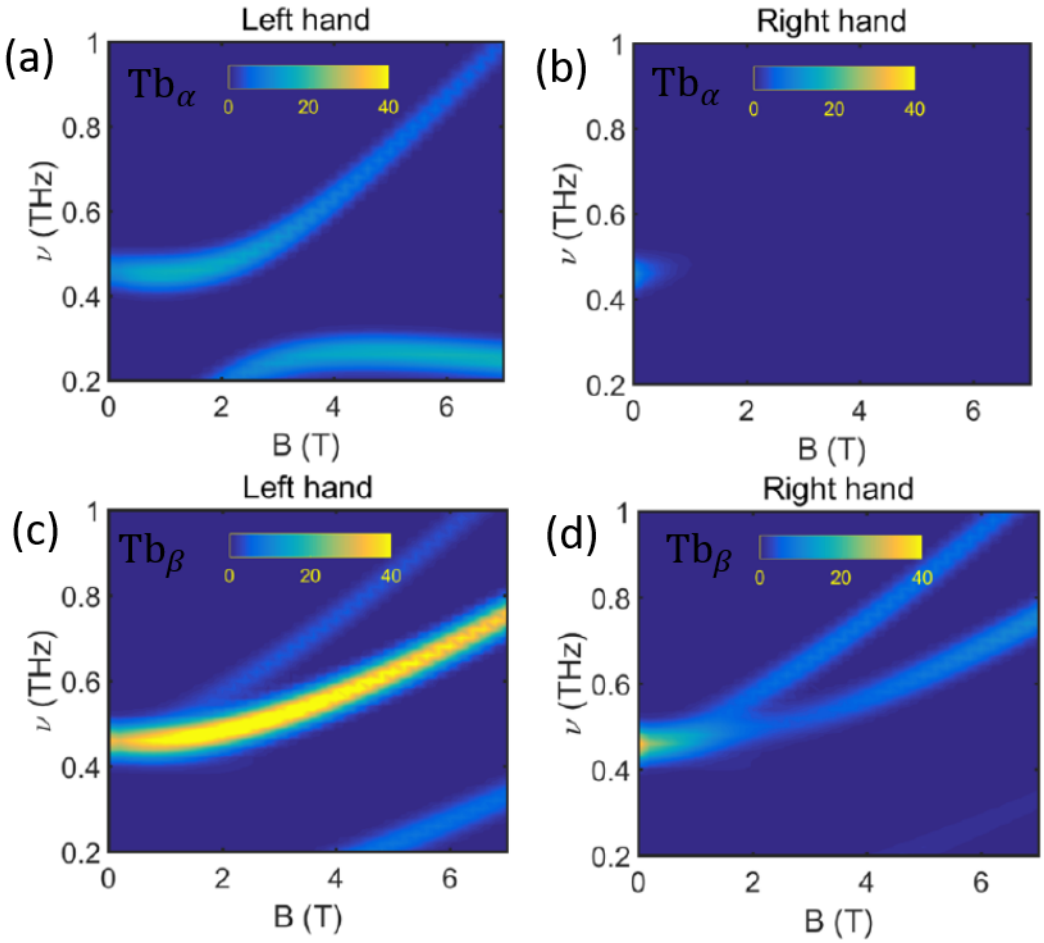

Figure 4.7: Colour plots of calculated intensity as a function of energy and field for Tb_α in left (a) and right (b) channel. The weak intensity at low field in (b) is the transition from thermally populated $G_2 \rightarrow E_2$. (c) and (d) are colour plots of calculated intensity as a function of energy and field for Tb_β in left and right, respectively.

Therefore, we can have 2D color plot of calculated intensity as function of energy and field for Tb_α and Tb_β in left and right circular basis as shown in Fig. 4.7. From the Fig. 4.7, we can see the transitions occurred for Tb_α indeed can only appear in left channel, while the transitions for Tb_β can appear in

both left and right channel. Using this simple field independent crystal field calculation, we can reproduce most of the features observed in experiments, the number of observed transitions, their intensities, their rough field dependence. Next we try to explain the observed CEF anomalies by this low energy CEF hybridization from our calculation.

4.2.3 Structural Phase Transition at 3 T?

Ref. [24] observed the CEF anomalies under magnetic fields using Raman scattering and proposed a structural phase transition in a 2.3 T [111] field due to displacement of O″. We observed similar features using TDTS, including a sharp up-turn of α_2^L at 3 T and the emergence of a "new" excitation just appearing at 3 T. However, we show here the the CEF anomalies can be understood from energy hybridization within the four lowest crystal energy levels, e.g., Fig. 4.6 (a) shows level repulsion between G_2 and E_1 for Tb_α, which causes a sharp up-turn of α_2^L at 3 T as shown in Fig. 4.7 (a). With increasing magnetic field, the intensity of α_1^L increases due to an enhanced transition amplitude based on Fermi's golden rule, which looks like a "new" excitation just appearing at 3 T. In addition, we performed specific heat measurements at 1.6 K from 0 to 6 T in a Quantum Design PPMS and found only a broad hump around 0.7 T, which is expected for low energy CEF, but no sharp peak at 2-3 T as expected for a structural phase transition. Therefore, we believe those sharp features,

which can be naively considered as phase transitions, in fact come from low energy CEF hybridization.

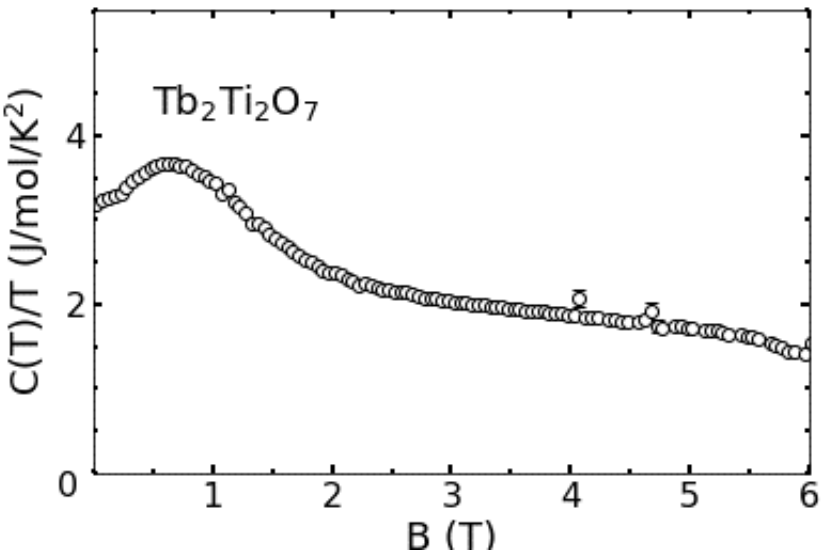

Figure 4.8: Specific heat was measured at 1.6 K from 0 to 6 T in a Quantum Design PPMS. There is a single peak at 0.7 T, which is related to low energy CEF, and no sharp peak around 3 T. No signature of structural phase transition was observed.

4.2.4 Inconsistency between Experiments and Calculations

In the above calculation, with only single ion CEF (field independent) and Zeeman terms involved, one can already explain the experiment reasonably well, but there remains some quantitative inconsistencies, particularly for the Tb_β contribution. For Tb_β, the transition $G_1 \to G_2$ should be visible in the THz

range but we do not observe it. In addition, both of the calculated transitions G_1 $\rightarrow E_1$ and $G_1 \rightarrow E_2$ are predicted to be much higher than the experimental data as shown in Fig. 4.9. The discrepancies between experiments and calculations are more clear in phase sensitive techniques than with interferometer [121].

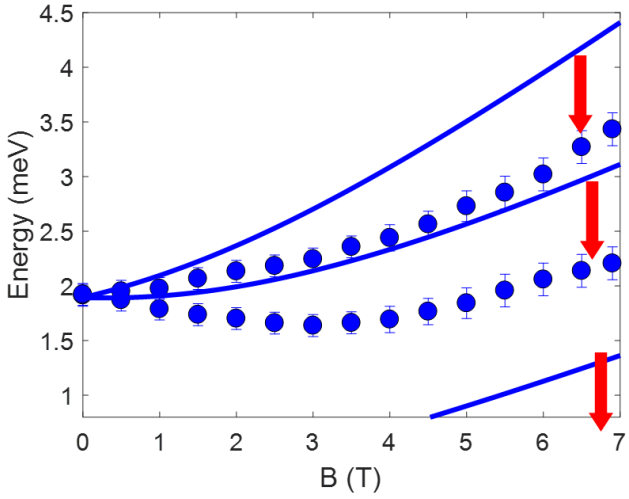

Figure 4.9: Comparison between experiments and calculations with independent CEF of external field for Tb_β, showing huge discrepancy.

Clearly, there are higher order effects we have not considered, which cause the inconsistency. We believe that magnetoelastic coupling or exchange interactions are not large effects.

Magnetoelastic coupling has been shown to exist in $Tb_2Ti_2O_7$ by many groups [23, 119, 120]. We also find a shift of energy around 0.1-0.2 meV from the ground state to the first excited state potentially due to magnetoelastic coupling. The magnetoelastic coupling Hamiltonian has a form $H_{ME} = \sum_{u,m} g_u \hat{U}_u \hat{O}_n^m$, where $\hat{U}_u = (\hat{a}_u + \hat{a}_u^\dagger)$ is the phonon annihilation and creation operator with a phonon

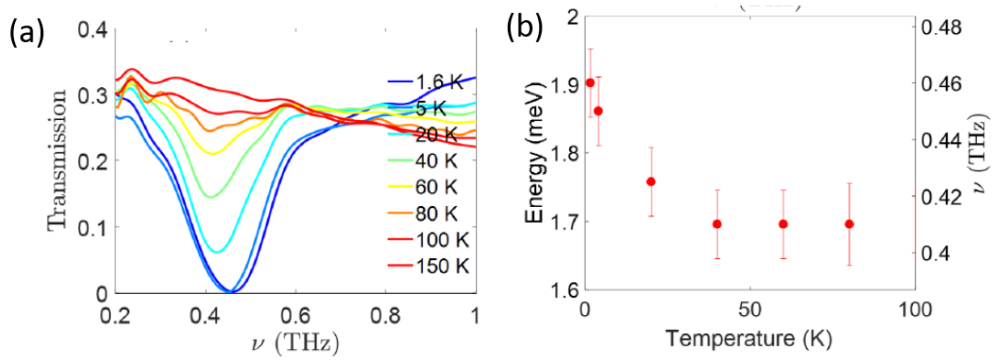

Figure 4.10: Transmission amplitude as a function of frequency in zero field measured from 1.6 K to 150 K. (b) The central frequency shifts slightly as a function of temperature.

displacement u, g_u is the magnetoelastic constant and $\hat{O}_n^m$ represents quadrupole operator. There are four quadrupole operators allowed to couple between E_u transverse phonon and E_g crystal field here, $\hat{O}_2^2 = J_x^2 - J_y^2, \hat{O}_2^{-2} = J_x J_y + J_y J_x, \hat{O}_2^1 = J_z J_x + J_x J_z, \hat{O}_2^{-1} = J_z J_y + J_y J_z$. Therefore, we can calculate the matrix elements within the 4 lowest CEF levels by using $J_z|j,m\rangle = m\hbar|j,m\rangle$ and $J_\pm|j,m\rangle = \sqrt{(j \mp m)(j \pm m + 1)}\hbar|j, m \pm 1\rangle$, where $J_\pm = J_x \pm iJ_y$. With a magnetoelastic coupling $g_u = 0.006(2)$, our calculation shows the splitting of doublets is around 0.1-0.2 meV and may result in the shift of the energy as function of temperature as shown in Fig. 4.10. At low temperature, we have the splitting due to magnetoelastic coupling, while at high temperature magnetoelastic coupling is suppressed and no splitting is present, hence the excitation energy (from ground state G to first excited state E) shifts to lower energy as increasing temperature. Although we find indirect evidence for magnetoelastic coupling,

a small energy $\sim$ 0.1-0.2 meV shift for the transition from the ground doublet G to first excited doublet E, the magnetoelastic coupling constant is limited by such small energy scale and has little contribution to the calculation, thus it is not a central ingredient to explain our data.

Now we show the influence of including antiferromagnetic interaction between the Tb spins. The calculation was done by my collaborator Yi Luo in the Broholm's group. Following Ref. [113], we consider isotropic antiferromagnetic interaction, namely

$$H_{\text{int}} = J_{\text{AF}} \sum_{\langle i,j \rangle} \mathbf{S}_i \cdot \mathbf{S}_j \tag{4.4}$$

besides H_{CEF} and H_{Zeeman}. The summation of pairs $\langle i, j \rangle$ runs over Tb spins within a single tetrahedron, as the correlation length of $Tb_2Ti_2O_7$ at 1.6 K is estimated to be of the size of one tetrahedron [18]. We keep the Hilbert space within only the four lowest CEF levels for each Tb ion, so each spin operator is 4 by 4 matrix. Considering 4 spins in one tetrahedron, the matrix of Hamiltonian has a dimension of $4^4 = 256$, which can be diagonalized to obtain eigenenergies. With J_{AF} gradually increased from 0 to 0.05 meV (Ref. [113] estimates $J_{\text{AF}} \approx 0.167\text{K} \approx 0.014$ meV), the simulated transmission amplitude evolves from Fig. 4.13 (a)-(d) for left channel and (e)-(h) for right channel. Compared to the observed transmission amplitude as shown in Fig. 4.4, the simulation shows

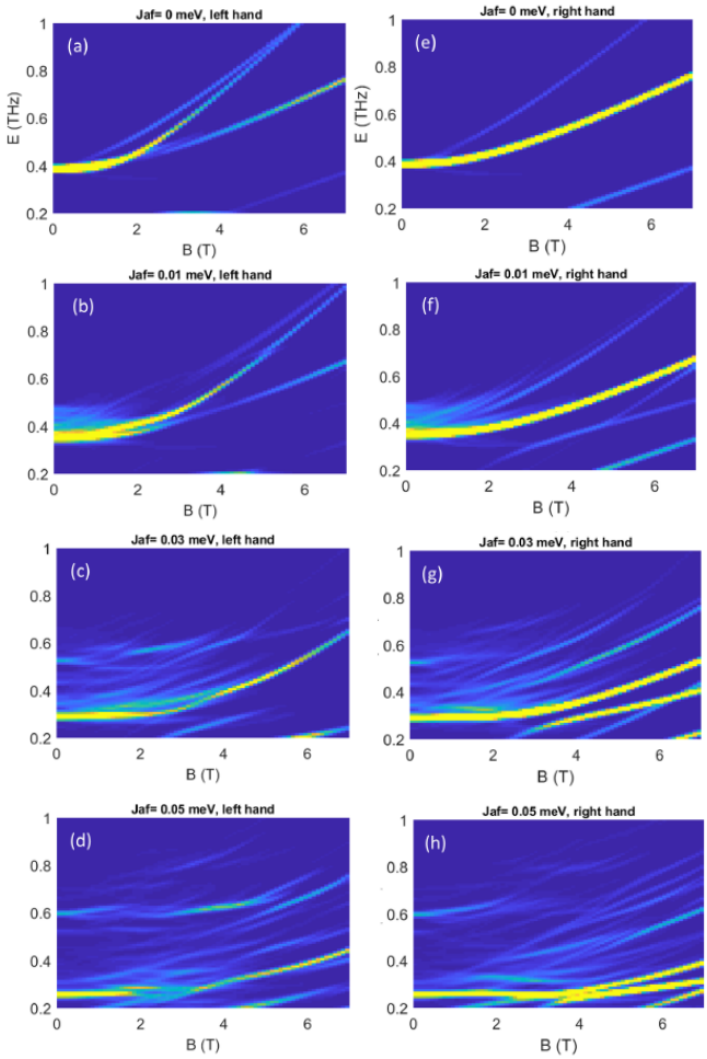

Figure 4.11: Simulated transmission amplitude for the full Hamiltonian $H_{\text{int}} + H_{\text{CEF}} + H_{\text{Zeeman}}$. The simulation gives a gap opening of the first CEF doublets (≈ 1.8meV ≈ 0.4THz) and more complicated splittings of modes than the observed spectra for $J_{\text{AF}} > 0.02$ meV.

the opening of a gap between the first excited CEF doublets (≈1.8 meV) at zero field and more complicated splittings of modes at finite field for $J_{\text{AF}} > 0.02$ meV, while for smaller J_{AF} the change from the result of $J_{\text{AF}} = 0$ (no interaction)

is not significant enough for a better agreement with the observation. Notice for this calculation we omit the dipolar interactions, which is estimated to be even smaller ($\approx$0.0315 K [113]), and other interaction anisotropy. Despite the simplified model, we show the qualitative disagreement between the simulation and the observed data. We conclude that the inclusion of a large exchange interactions are incompatible with the experimental result and unhelpful for a better fitting.

Of course the exchange interaction is necessary to reproduce the dispersion of the CEFs, but it does not improve agreement as function of field at the Γ point. Both moderate magnetoelastic couplings and exchange interactions can lead to finite splitting of the zero field doublets, which is inconsistent with an almost invisible splitting in the experiment. This gives an upper bound on their significance. Then the question is what is the real reason that leads to the inconsistency between experiments and the CEF calculations.

4.2.5 Field Dependent Crystal Field Calculation

The preceding analysis treats the CEF Hamiltonian as independent of external magnetic field. However, the magnetic field can influence the crystal field environment as follows. The orbital angular momentum results from the spatially anisotropic $4f$ wave functions that can be envisioned as oblate electron charge cloud. Applying magnetic field along the [111] direction aligns the

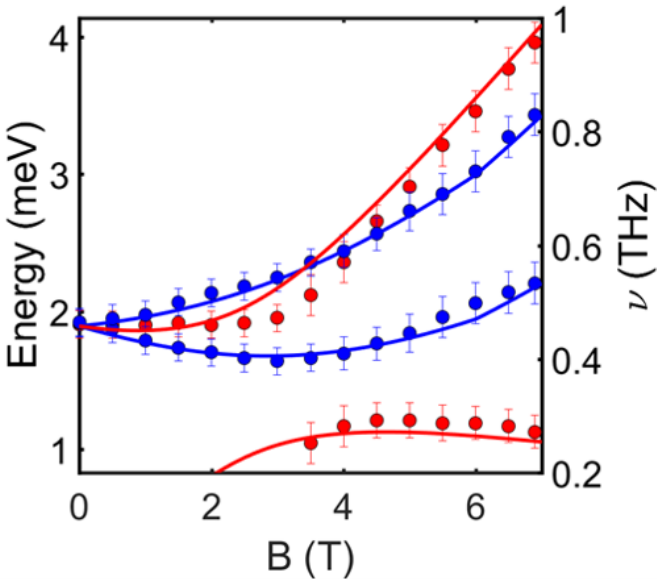

Figure 4.12: Comparison between experiment and calculated energy with consideration of field induced crystal field environment changes. Red and blue represent Tb_α and Tb_β.

spin of Tb and also the electron cloud because of spin-orbital coupling. This modifies the interaction between valence electrons of Tb and its neighbour ligands (O″) via Coulomb repulsion, which results in field induced crystal environment changes. This should be a ubiquitous effect although the influence is generally negligible. Here, such effect may be amplified due to the dynamic vibration of atoms, which makes the overlap between electrons clouds possibly larger. Therefore we incorporate magnetic field induced crystal field changes in our calculations as follows.

Applying a field reduces the symmetry for Tb_β from D_{3d} to C_1, which allows additional Stevens operators to appear in H_{CEF}. It is sufficient to fit the data by including six of them: O_2^1, O_2^2, O_4^2, O_4^4, O_6^2, O_6^4. On the other hand, Tb_α remains

D_{3d}, so we keep the same Stevens operators O_2^0, O_4^0, O_4^3, O_6^0, O_6^3, O_6^6 but adding extra field dependence to the original B_q^k. For simplicity, we approximate the dependence of the changes of CEF parameters to be linear on applied field, $\Delta B_q^k = c_q^k B$, where c_q^k is a coefficient of linear field dependence. Therefore, the modified B_q^k at finite field is sum of original B_q^k at zero field and field induced change ΔB_q^k. We fit the energy excitations to the refined model. The obtained linear field dependent parameters are listed in Tab. 4.2. With increasing the external field further, the spin of Tb gradually aligns with magnetic field, so eventually there is a threshold of magnetic field $\sim$ 6 T, above which the CEF doesn't change any more.

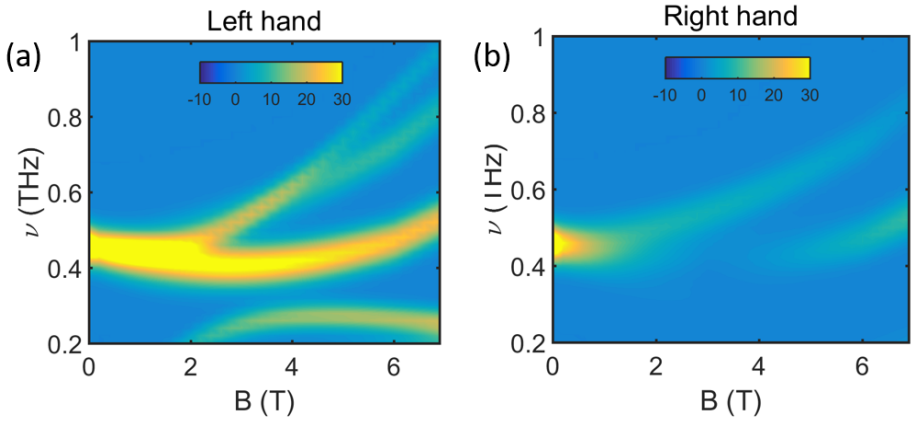

Figure 4.13: Colour plot of calculated intensity as function of energy and field for Tb_α and Tb_β in left (a) and right (b) channel.

As shown in Fig. 4.12, by including the field dependent CEF Hamiltonian, the experimental spectra can be reproduced essentially perfectly: the calculated energies of β_1 and β_2 for Tb_β are lower and match with data now; the

D_{3d}	c_0^2	c_0^4	c_3^4	c_0^6	c_3^6	c_6^6	C_1	c_1^2	c_2^2	c_2^4	c_4^4	c_2^6	c_4^6
Tb_α	-0.46	-1.5	0.9	0.1	1.4	-1.6	Tb_α	0	0	0	0	0	0
Tb_β	0.48	-3.1	-0.5	-1	-0.3	1.9	Tb_β	0.14	-0.21	-0.27	2.9	0.01	0.01

Table 4.2: The linear field coefficient c_q^k for Tb_α with D_{3d} and Tb_β with C_1 symmetry in unit of meV.

transition $G_1 \rightarrow G_2$ is suppressed to below the THz range. The total change of parameter ΔB_q^k is relatively small as compared to the original B_q^k in Tab. 4.1 and has negligible impact on the high energy excitations. Fig. 4.13 is the intensity plots for left and right basis and shows a good agreement with experiments.

There are a few things to note. (1) For better agreement with experiment, we use a slightly reduced g factor $\sim$1.3 for the calculation instead of the Landé $g_J = 1.5$. This small correction only modifies the results slightly and does not change the essential features. There are at least two possibilities for the reduced g factor. First, the Landé result assumes the LS coupling scheme (J=6) and ignores higher-order couplings that can reduce g. Moreover, the possibility of a dynamic Jahn-Teller effect has been reported [20, 122] that can lead to a reduced g factor due to quenching of the orbital moment [123]. (2) The coupling between magnetic field and the CEF changes the electron charge cloud and reduces the symmetry of Tb_β to C_1. This may lead to a displacement of atoms, e.g., O′′, but not necessarily. With the likely dynamic Jahn-Teller effect in $Tb_2Ti_2O_7$, atoms may vibrate around the original position without having finite displacement [20, 122].

4.3 Conclusion

We performed time domain terahertz spectroscopy on high quality single crystal $Tb_2Ti_2O_7$ and were able to obtain complex transmission in linear basis, which was further converted into circular basis, which is the eigen-polarization for transmission. We observed multiple excitations in our spectra and assigned the excitations to CEF excitations based on optical selection rules. Several CEF anomalies in our spectra can be well explained by low energy crystal field hybridization. In accord with our specific heat measurements, we believe there is no phase transition at 3 T in contrast to previous Raman scattering [24]. The high quality data and correct basis accessed by TDTS allow us to make a quantitative comparison between experiments and crystal field (field independent) calculations, which shows large discrepancy. This indicates an important effect is missed. After ruling out the possibility of magnetoelastic coupling and exchange interactions, we see that the crystal field environment can be affected by magnetic field significantly. Including this field dependent crystal field Hamiltonian, the agreement between experiments and calculations are excellent, highlighting important interplay among multiple degrees of freedom (spin-orbital-lattice) in $Tb_2Ti_2O_7$.

Chapter 5

A New Proximate Kitaev Spin Liquid $BaCo_2(AsO_4)_2$

I performed THz spectroscopy on a new version of cobalt based Kitaev spin liquid candidate $BaCo_2(AsO_4)_2$. A broad continuum that coexists with magnon excitations is observed below the Néel transition temperature. The continuum at Γ point is consistent with the excitations from the fractionalized Majorana fermions in the Kitaev model. The continuum is not sensitive to increasing temperatures, which is also consistent with the thermodynamics of the Kitaev model [26, 124]. In the relatively high temperature regime (Kitaev paramagnet), applying a magnetic field can suppress the continuum continuously, suggesting a smooth connection between the Kitaev paramagnetic state and the field polarized state. At low temperature, I found rich magnetic phases, char-

acterized by one and two magnon excitations. Remarkably, there is a narrow field range $\sim$ 0.5 T that suppresses the magnon excitations abruptly. The behaviour is very similar to what have been observed in α-$RuCl_3$. Therefore it is a possible field induced Kitaev spin liquid regime but with a much smaller critical field. Along with no stacking faults or coexisting domains detected in $BaCo_2(AsO_4)_2$, this work shows that this material may be an ideal material realization of the Kitaev spin liquid.

5.1 Introduction to $BaCo_2(AsO_4)_2$

A theoretical breakthrough in spin liquids was made in 2006 by Alexei Kitaev. Kitaev proposed a simple but novel model that is exactly solvable. Kitaev model shows a QSL ground state, where the spins fractionalize into emergent quasi-particles, well known as Majorana fermions [53].

The Kitaev model consists of S=1/2 spins on a honeycomb lattice with nearest neighbor ferromagnetic Ising interactions, which have bond dependence with easy axis along the x, y, z direction. The Kitaev spin Hamiltonian reads:

$$H_K = -J_K^x \sum_{<ij>_x} \sigma_i^x \sigma_j^x - J_K^y \sum_{<ij>_y} \sigma_i^y \sigma_j^y - J_K^z \sum_{<ij>_z} \sigma_i^z \sigma_j^z \tag{5.1}$$

where σ are Pauli matrices, and $< ij >_{x,y,z}$ denotes x, y, z bonds accordingly as shown in Fig.1.3.

5.1.1 Experimental Signatures of a Proximate Kitaev Spin liquid

The exactly solvable Kitaev model not only offers fundamental insights for spin liquid community, but also brings up the possibility of realizing quantum computation [53, 54]. Therefore, the realization of the Kitaev model in real materials is of intense interest. In order to fulfill the bond dependent spin interactions of the Kitaev model, materials with strong spin-orbit coupling are promising candidates. On the early stage, iridates such as Na_2IrO_3 were proposed and showed spin liquid features [125, 126]. However, iridates order at high temperature $\sim$ 15 K, which means iridates are not ideal quantum spin liquids. In addition, the unfavourable magnetic form factor and strong absorption cross-section of the Ir ions inhibit the means of inelastic neutron scattering, hence lack of definitive evidence of the Kitaev spin liquid.

More recently, van der Waals ruthenate α-$RuCl_3$ with $J_{eff} = 1/2$ $4d^5$ Ru^{3+} ions is synthesized and attracts intense attentions. Although this compound has a zigzag order transition $\sim$ 7 K, it is still considered as a proximate Kitaev spin liquid due to several unusual features above the magnetic ordering temperature in contrast to the honeycomb iridates as shown in Fig. 5.1 [25]. The magnetic excitation persists above transition temperature, which is in contrast to the conventional magnon behaviour. Remarkably, the continuum

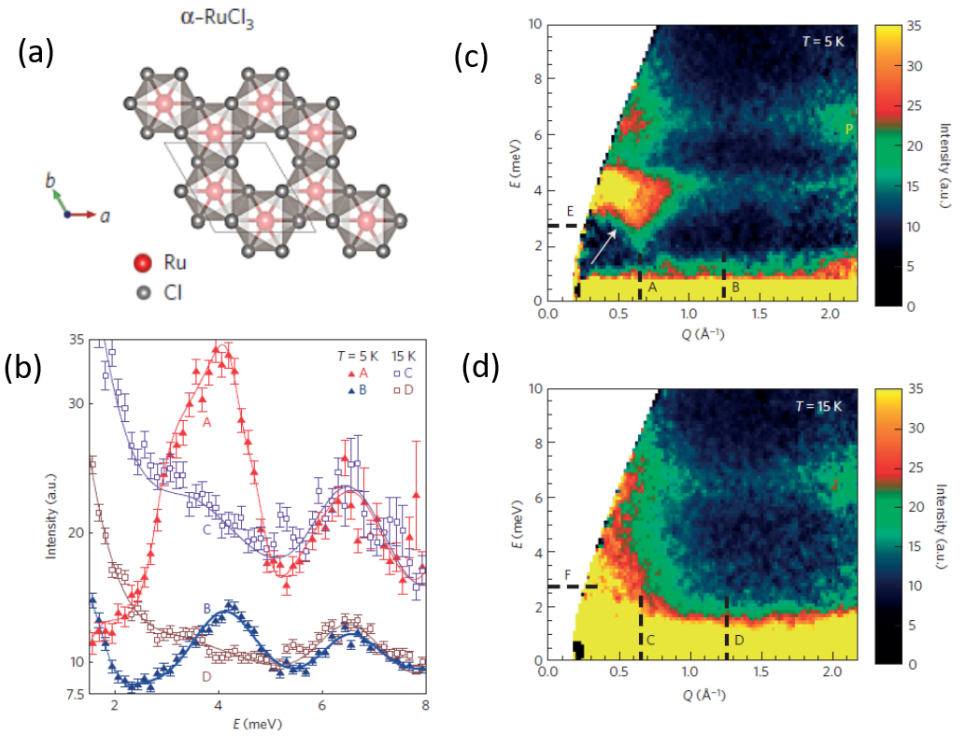

Figure 5.1: (a) In-plane honeycomb structure, showing edge sharing $RuCl_6$ octahedra. (b) Constant Q cut along the dashed lines in (c) and (d). (c) and (d) are image plots of data as a function of energy and momentum below and above the transition temperature, respectively. Figures are from Ref. [25]

centered at Γ point can be roughly reproduced by the pure Kitaev model. The small disagreement between the calculations and experiments originate from anisotropy terms in the Kitaev model or non-Kitaev interactions in real materials. The continuum at Γ point is very stable with temperature (persisting up to 120 K), which is consistent with the thermodynamics of the Kitaev model [26, 124]. More evidences for a Kitaev spin liquid comes from the continuum observed in Raman scattering, which follows the fermionic distribu-

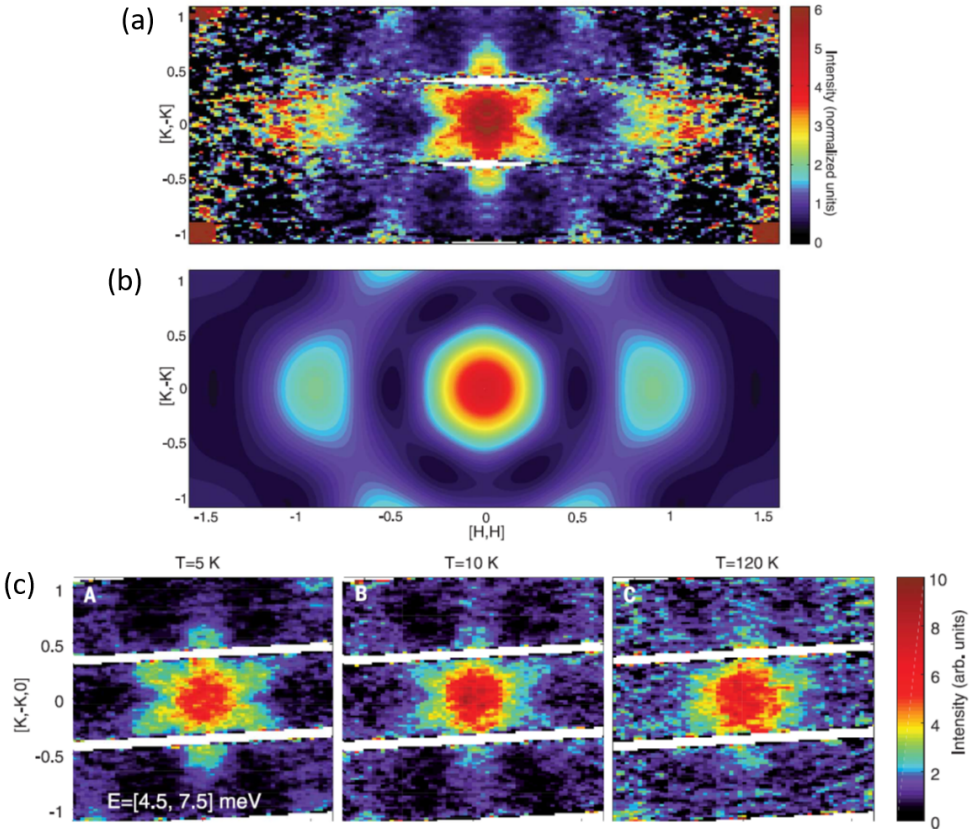

Figure 5.2: (a) Data at T = 5 K, integrated over the range E = [4.5, 7.5] meV and L = [–2.5, 2.5] and symmetrized along the (H, H) direction. (b) Calculations based on pure isotropic Kitaev model. (c) Momentum and temperature dependence of the magnetic continuum. Figures are from Ref. [26]

tion [27, 28]. The smoking gun evidence is the observation of the half-integer quantization of the thermal Hall conductance, which is a signature of topologically protected chiral edge currents of charge-neutral Majorana fermions [127]. However these experiments are currently controversial.

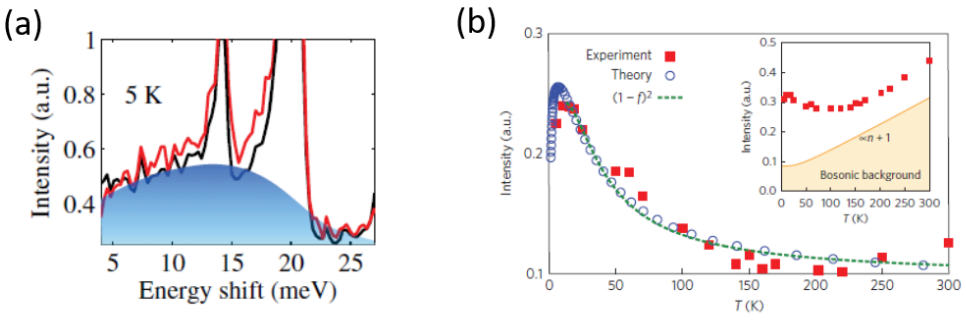

Figure 5.3: (a) The intensity of the continuum observed in Raman scattering at 5 K.(b) Comparison between the numerical results and the experimental data for α-$RuCl_3$. The data follows a two-fermionic distribution. Figures are from Ref. [27, 28]

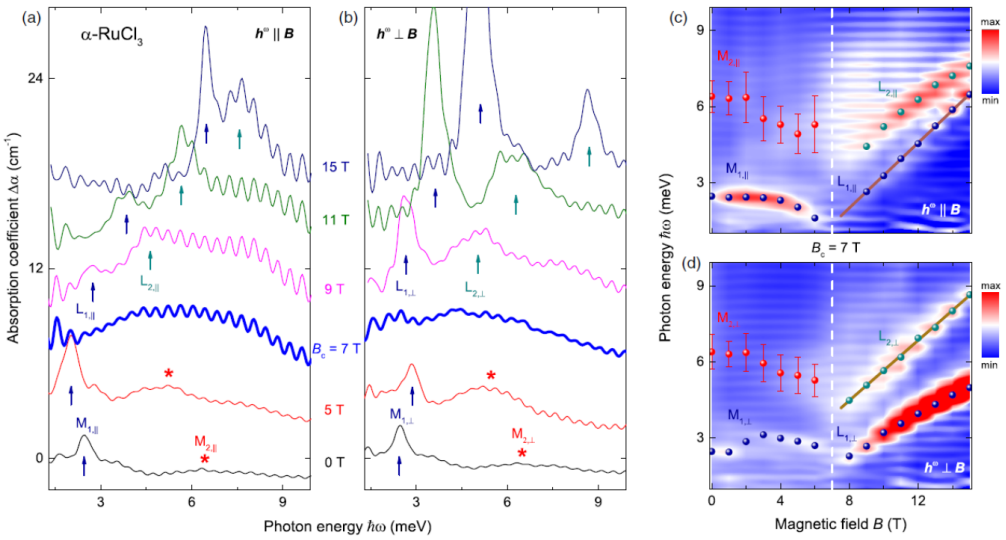

Figure 5.4: (a) The evolution of the magnetic excitations at different magnetic fields as $h_{ac} \parallel B$ by THz spectroscopy. (b) The evolution of the magnetic excitations at different magnetic fields as $h_{ac} \perp B$. (c) and (d) are contour plots of the absorptions as a function of magnetic field and energy for $h_{ac} \parallel B$ and $h_{ac} \perp B$, respectively. Figures are from Ref. [29]

5.1.2 A Field Induced Quantum Spin Liquid

The fact that α-$RuCl_3$ orders at 7 K indicates some non-Kitaev terms are present such as the Heisenberg or off-diagonal terms. It has been reported by many experiments that applying in-plane magnetic field can suppress the long range order and α-$RuCl_3$ experiences a quantum phase transition around 8 T, above which is considered as the field induced spin liquid regime. For example, in susceptibility and specific-heat measurements, the peaks associated with magnetic order are suppressed $\sim$ 8 T [128]. Furthermore, it has been shown that the spin wave excitations are suppressed at a field of 8 T by neutron scattering [129]. Since the lower energy prominent features lie around the Γ point, it is suitable to study this material by THz spectroscopy. It is indeed found that the magnetic peaks evolve into a broad continuum at $\sim$ 7 T [29], which is a signature for a quantum phase transition. As shown in Fig. 5.4, both the intensity and energy of the magnon peaks are reduced towards the critical field. Above the critical field, new peaks develop with increasing intensity and energy. Other THz measurements also supports an intermediate regime $\sim$ 8 T, which separate the low field zigzag order state and the high field polarized regime [130–133].

5.1.3 A Cobalt Based Kitaev Spin Liquid Candidate $BaCo_2(AsO_4)_2$

The current focus of Kitaev spin liquid candidates is on d^5 pseudospin-1/2 ions Ir^{4+} and Ru^{3+} with t_{2g}^5 (S = 1/2,L = 1) electronic configuration. However, all current materials seem to deviate from the pure Kitaev model due to the presence of significant non-Kitaev terms such as anti-ferromagnetic Heisenberg interactions. Hence, discovering a material that can minimize the non-Kitaev terms is in demand. It has been shown that the Kitaev model can be realized in materials based on d^7 ions with $t_{2g}^5 e_g^2$ (S = 3/2, L = 1) configuration such as Co^{2+}, which also hosts the pseudospin-1/2 magnetic moment just like the case for Ir^{4+} and Ru^{3+} [134, 135]. Interestingly, the presence of extra e_g^2 electrons introduces additional exchange hopping processes, which suppress the Heisenberg interactions. As a result, the Kitaev interaction is expected to be the dominant term and the Cobalt based honeycomb compounds may be better realizations of the Kitaev model.

$BaCo_2(AsO_4)_2$ is a promising Kitaev spin liquid candidate and was first studied 40 years ago by neutron scattering [136–138]. It has been revisited recently after realizing the possibility of the Kitaev spin liquids [30]. In $BaCo_2(AsO_4)_2$, the edge-sharing CoO_6 octahedra form a honeycomb lattice. In contrast to α-$RuCl_3$, no stacking faults or twin domains are detected, making this material

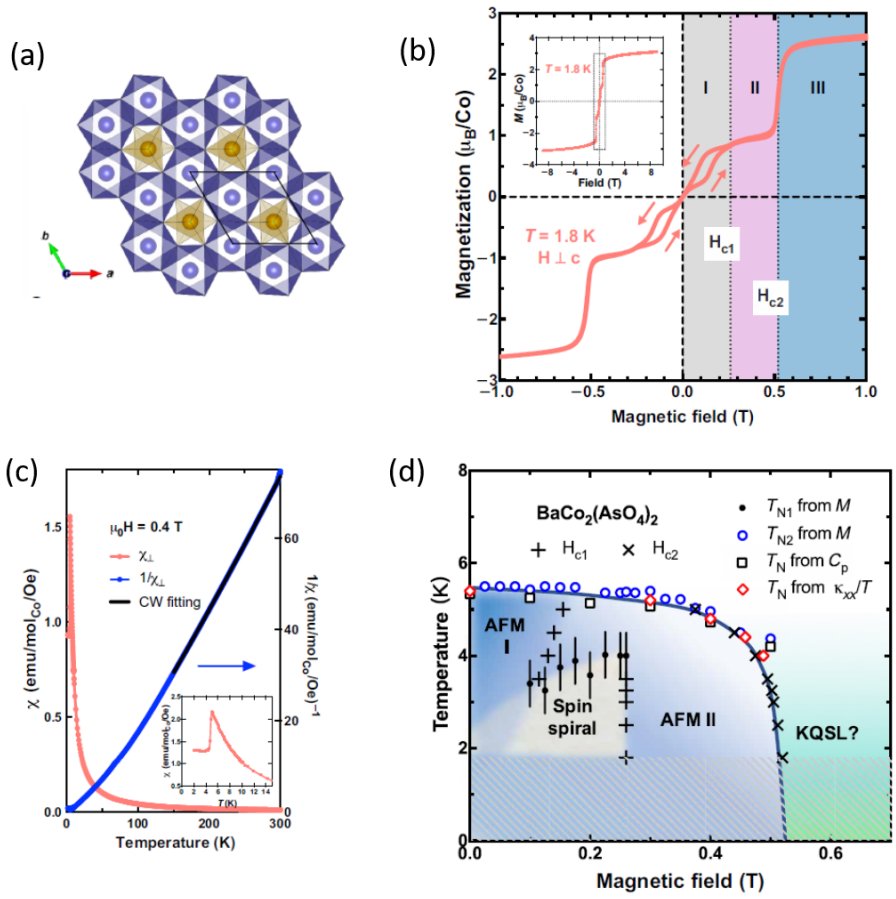

Figure 5.5: (a) Schematic of the $BaCo_2(AsO_4)_2$ crystal. (b) The magnetization as a function of magnetic field at 1.8 K. (c) Susceptibility measurements show the transition temperature around 5.5 K. (d) The phase diagram of the $BaCo_2(AsO_4)_2$ is obtained based on various experiments. Figures are from Ref. [30]

a better version of α-$RuCl_3$. The susceptibility measurement shows a phase transition around 5.5 K, which is smaller than α-$RuCl_3$. The magnetization curve as shown in Fig. 5.5 shows three magnetic phases at 2 K as applying in-plane magnetic field. Region 1 is a spiral magnetic ordered state, region 2 is a co-linear ordered state and region 3 is labelled as the field induced Ki-

taev spin liquid state. Although $BaCo_2(AsO_4)_2$ shows some features that resemble α-$RuCl_3$, so far more direct evidences of a Kitaev spin liquid such as the fractionalized continuum that can be probed by neutron scattering or THz spectroscopy is lacking.

5.2 Experimental Results

The experiments were performed in the Voigt ($k \perp B$) geometries, where k is the direction of light propagation perpendicular to sample surface and B is the external in-plane magnetic field. In principle, applying in-plane $B \parallel a^*$ should give different results than $B \parallel a$, but it turns out these two field directions give results that are essentially identical. In both cases, the THz pulse ac magnetic field, h, was applied either $h \perp B$ or $h \parallel B$, which will reveal different features according to the optical selection rules.

5.2.1 Observation of Nontrivial Continuum at Zero Magnetic Field

As shown in the preceding section, the observation of a broad continuum near the Brillouin zone center by neutron scattering is consistent with scattering from the Majorana quasi-particles in the Kitaev model [25, 26]. As shown

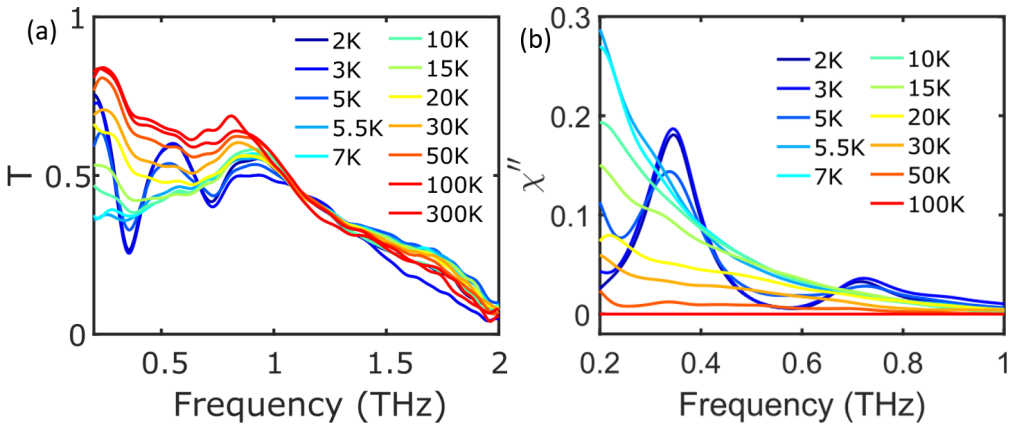

Figure 5.6: (a) The THz transmission magnitude as a function of frequency at different temperatures. (b) The calculated susceptibility from the complex transmission with reference temperature 100 K.

in Fig. 5.6 (a), the THz transmission spectrum also shows a broad absorption below 1 THz. In order to get rid of non-magnetic background and experimental noise, I calculated the image susceptibility discussed in chapter 2. The susceptibility χ'' is shown in Fig. 5.6 (b). It is clear that the continuum arises below 100 K and grows as decreasing temperatures. Immediately upon passing below the transition temperature $T_N \sim 5.5$ K, the remaining continuum is suppressed and one and two magnon excitations develop. The continuum coexisting with the magnon excitations at 5 K below T_N indicates the ordered state of $BaCo_2(AsO_4)_2$ is unconventional as all the spectral weight should transfer to the magnon or two magnon excitations in conventional magnets. Further decreasing the temperature down to 2 K, the continuum is almost suppressed completely in our experimental range. The continuous suppression of the con-

tinuum below T_N can be understood as the fractionalized Majorana quasiparticles in the Kitaev model being replaced by magnons in the long ranged order state. The significant decrease of the continuum in $BaCo_2(AsO_4)_2$ is different than α-$RuCl_3$, where the continuum is almost unaffected as entering the ordered state [25]. The continuum in α-$RuCl_3$ may come from magnon decay due to large anisotropic off-diagonal non-Kitaev terms or disorder in the material.

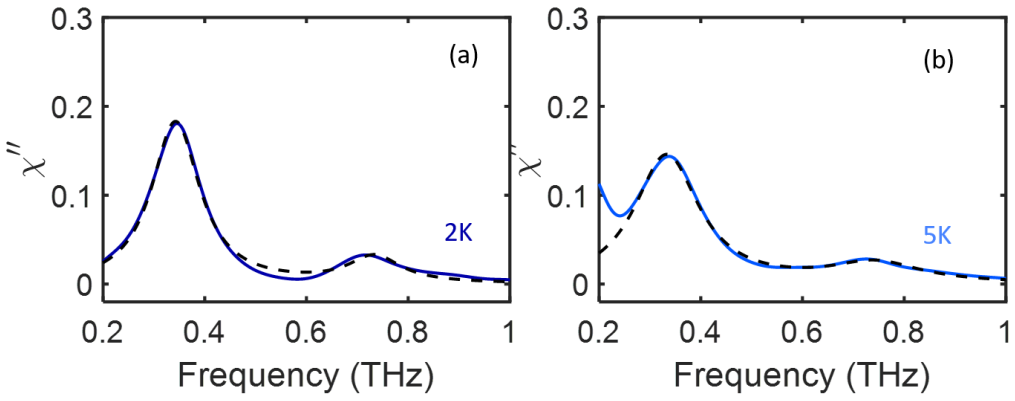

Figure 5.7: (a) Imaginary susceptibility at 2 and (b) 5 K with Lorentzian fitting represented by dashed lines.

In order to determine if the continuum at 2 K is completely gone below THz range, we first fit both the one and two magnon excitations with Lorentzian function

$$\chi''(\nu) = \frac{S\Gamma\nu}{(\nu^2 - \nu_0^2)^2 + \nu^2\Gamma^2} \tag{5.2}$$

where S parametrizes the amplitude, Γ is the THz linewidth and ν_0 is the cen-

tral frequency. Next we perform a sum rule analysis based on Kramers-Kronig relation to relate the $\chi^{''}(\nu)$ of one and two magnon excitations in Lorentzian form to the dc susceptibility $\chi^{'}(0)$. The sum rule is given by

$$\chi^{'}(0) = \frac{2}{\pi}\int_0^\infty \frac{\chi^{''}(\nu)}{\nu} d\nu. \tag{5.3}$$

The obtained dc contribution from the fits to the one and two magnon peaks is ~ 0.07, which is much smaller than the value ~ 0.2 from dc susceptibility measurement [30]. Hence, there must be some remaining continuum at low frequency even down to 2 K.

We can estimate the Kitaev interactions in this material based on the continuum. It has been shown that the continuum is supposed to extend up to $\omega \sim 2J_K$, where J_K is the Kitaev interaction constant [139, 140]. Therefore, J_K is around 2 meV in $BaCo_2(AsO_4)_2$.

Regarding the spectrum above transition temperature at 7 K, we use a Lorentzian form with a low frequency cutoff to roughly capture the trend. Performing the sum rule analysis and comparing with dc susceptibility, that with a cutoff of ~ 0.05 THz we can account for all the spectral weight needed to get the dc susceptibility as shown in Fig. 5.8. In another word, integrating from 0.05 to 1 THz can recover all dc susceptibility 0.34 at 7 K and there is likely a gap below 0.05 THz which is coincident with the flux gap predicted in Kitaev

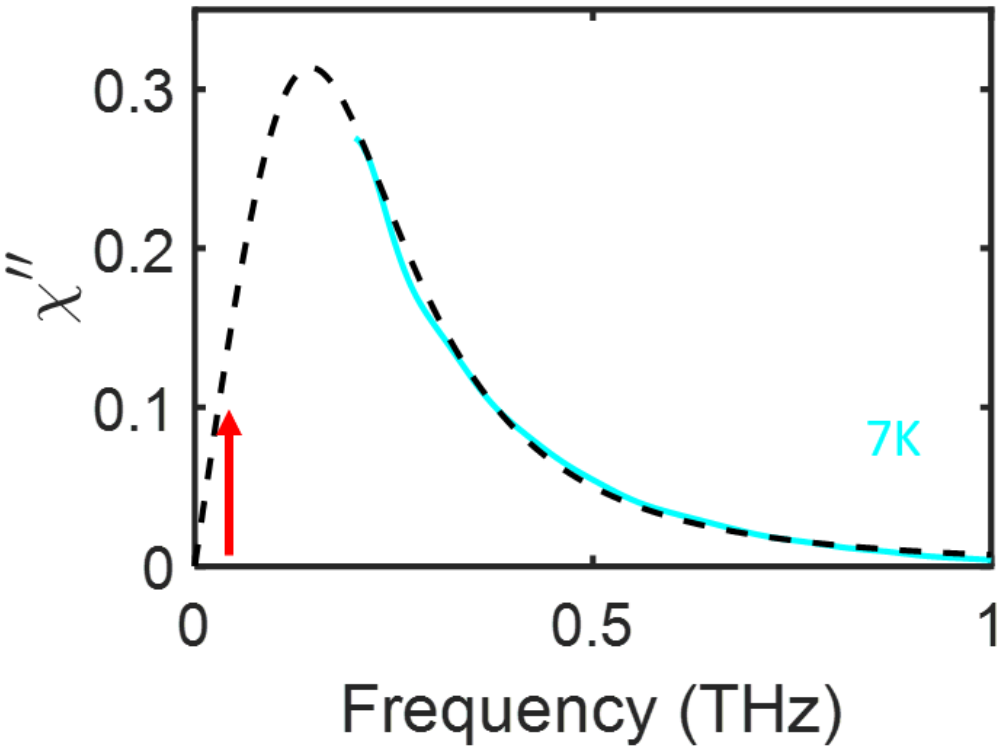

Figure 5.8: Imaginary susceptibility at 7 K and Lorentzian fitting represented by dashed line and a cutoff denoted by a red arrow.

model $\Delta \sim 0.1 J_K$ [139, 140].

5.2.2 Temperature and Field Effects on the Kitaev Paramagnetic Regime

The continuum is very stable with temperature and persists up to 50 K $\sim 10 T_N$, which is consistent with the thermodynamics of the Kitaev model [26, 124, 140, 141]. This was also observed previously in α-$RuCl_3$ [26, 124]. Despite the requirement of low temperature to realize Kitaev spin liquid, the Ki-

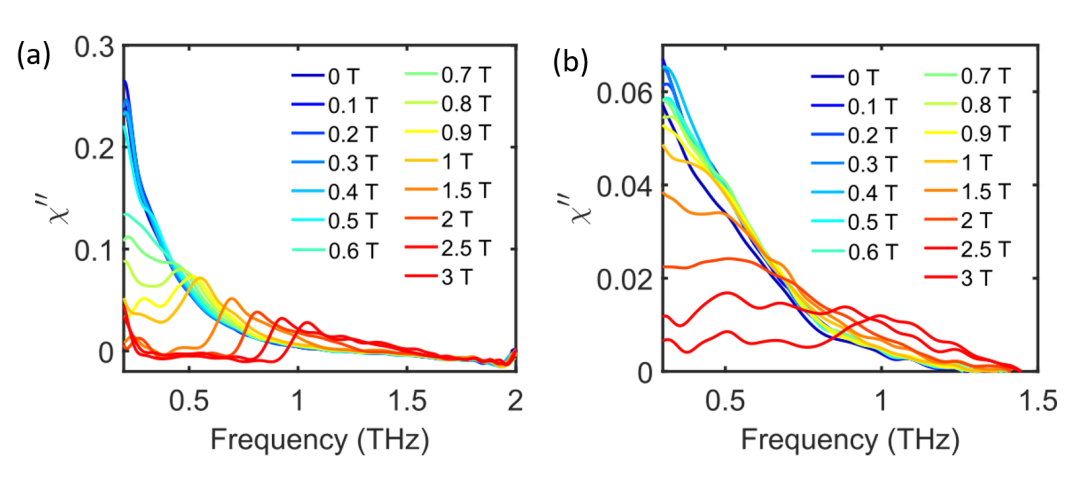

Figure 5.9: (a) The imaginary susceptibility at 7 K with different magnetic fields . (b) The imaginary susceptibility at 20 K. Here, B ∥ a with h ∥ B

taev physics can persist up to higher temperatures, where the Kitaev physics is not yet destroyed by thermal fluctuations. This is the Kitaev paramagnetic region, where both Majorana fermions and Z_2 fluxes can be thermally activated, hence the continuum persists even at high temperature [124, 142]. At low temperature, only the itinerant Majorana fermions can be activated and Z_2 fluxes are frozen. At even higher temperature, the Kitaev physics fades away eventually and the material becomes a conventional paramagnet around 100 K.

Applying magnetic field on the Kitaev paramagnetic state will destroy the Kitaev physics and turn the system into a field polarized regime. As shown in Figs. 5.9 (a) and (b) for 7 K and 20 K, applying an in-plane magnetic field reduces the intensity of the continuum. At certain fields, the continuum disappears and two magnon excitations form with peak positions moving to higher

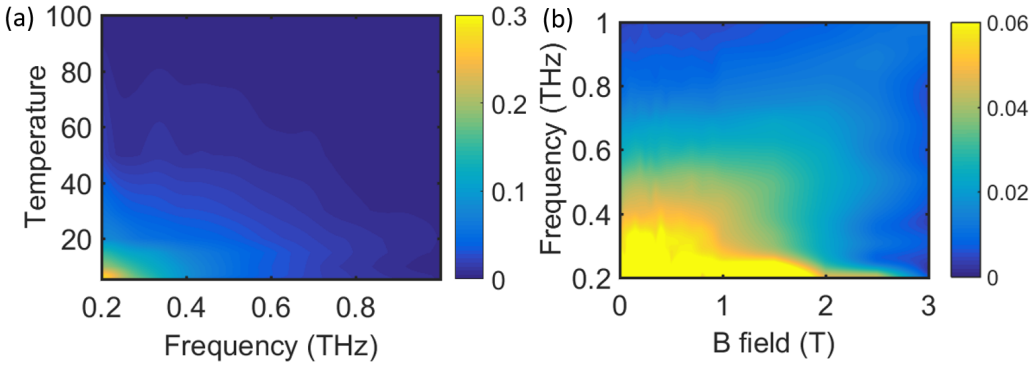

Figure 5.10: (a) The image plot of the imaginary susceptibility as a function of frequency and temperature at zero field. (b) The image plot of the imaginary susceptibility as a function of magnetic field and frequency at 20 K in the Kitaev paramagnetic regime with B ∥ a and h ∥ B.

frequencies with increasing fields. Because no discontinuity was observed in ac susceptibility measurements as a function of field above T_N, the Kitaev paramagnetic regime should be connected to the field polarized regime continuously.

Fig. 5.10 (a) and (b) show the temperature and field effects on the continuum, respectively. In the Kitaev paramagnetic regime, both increasing temperatures and magnetic fields diminish the continuum gradually. The continuum is suppressed once entering the conventional paramagnetic regime or field polarized regime.

5.2.3 A Possible Field Induced Kitaev Spin Liquid

Now, I will focus on the low temperature regime (2 K) with magnetic field. Fig. 5.11 shows the transmission as B applied along a with h $\parallel$ B and h $\perp$ B in (a)(c) and (b)(d), respectively. Fig. 5.11 (a) and (b) focus on low field regime, while (c) and (d) include higher fields. With h $\parallel$ B, the so-called "longitudinal" channel, THz mainly excites two magnon excitations unless the spins are not perfectly aligned with external magnetic field B. On the other hand, with h $\perp$ B, THz mainly excites one magnon excitations and is less sensitive to two magnon features. By comparing between Fig. 5.11 (a) and (b), one can identify three critical fields $B_{c1} \sim 0.2$ T, $B_{c2} \sim 0.5$ T and $B^{*}_{c2} \sim 0.55$ T.

As shown in Fig. 5.11 (a), the magnon excitation around 0.37 THz becomes weaker and almost disappears above 0.2 T. This is consistent with a transition from a spiral long range ordered state to a colinear ordered state around as reported previously [30, 136–138]. Below H_{c1}, the spins in the spiral ordered state have transverse component to THz magnetic field h, therefore the one magnon excitations can be observed with h $\parallel$ B. Above B_{c1} and below B_{c2}, the spins in the colinear ordered state are orientated along B field, hence no magnon peaks are observed. In Fig. 5.11 (b), the magnon excitation splits into two peaks upon entering the colinear phase as expected. The spin wave for the

two sublattices are degenerate in the spiral phase, while in the colinear phase the two spins in the unit cell point in opposite directions, giving rise to two different spin waves.

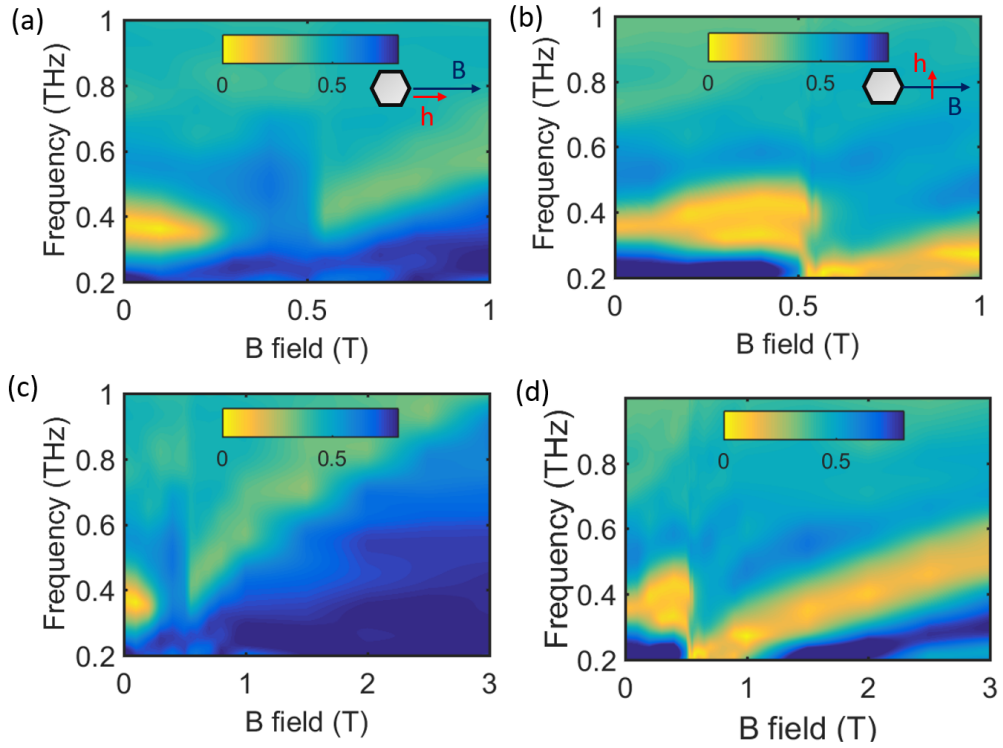

Figure 5.11: The image plot of the transmission as a function of magnetic field and frequency at 2 K. (a) h $\parallel$ B with B field from 0 to 1 T. (b) h $\perp$ B with B field from 0 to 1 T. (c) h $\parallel$ B with B field from 0 to 3 T. (d) h $\perp$ B with B field from 0 to 3 T.

Above B^*_{c2} 0.55 T, Fig. 5.11 (a) shows two magnon excitations starting at 0.4 THz and moving to higher frequency, while Fig. 5.11 (b) shows one magnon excitations with the half slope of the two magnon excitations, indicating the field polarized regime. Remarkably, in the region from 0.5 T to 0.55 T, the intensity of the upper one magnon peak branch is reduced abruptly with almost

unchanged energy, while the energy of the lower one magnon branch drops quickly below our THz range. The critical fields are consistent with previous magnetization and ac susceptibility measurements [30]. We believe the abrupt suppression of the magnon excitations implies a field induced spin liquid state in the 0.5 to 0.55 T field range. Similar features were interpreted as the signatures of field induced spin liquid state in α-$RuCl_3$ [128].

By combining the information from the two configurations $h \parallel B$ and $h \perp B$, the one magnon and two magnon energy versus magnetic field can be obtained as shown in Fig. 5.12. We find in addition to the interesting behaviour of one magnon excitations, two magnon excitations in the field induced spin liquid regime are also non-trivial. The two magnon energy in the field polarized regime has roughly the same energy as the one magnon energy in the ordered state and the slope of two magnon excitations around B^*_{c2} is obviously larger than the slope in field polarized regime, give a convex curvature.

It is worth mentioning that the critical field B_{c2}, B^*_{c2} in $BaCo_2(AsO_4)_2$ is 10 times smaller than α-$RuCl_3$, which means the non-Kitaev interactions are roughly 10 times smaller compared to α-$RuCl_3$. The Kitaev interaction is around 2 meV as estimated from the upper edge of the continuum, which is comparable to α-$RuCl_3$. Therefore, the relative portion of Kitaev term with respect to non-Kitaev term in $BaCo_2(AsO_4)_2$ is much larger compared with α-$RuCl_3$.

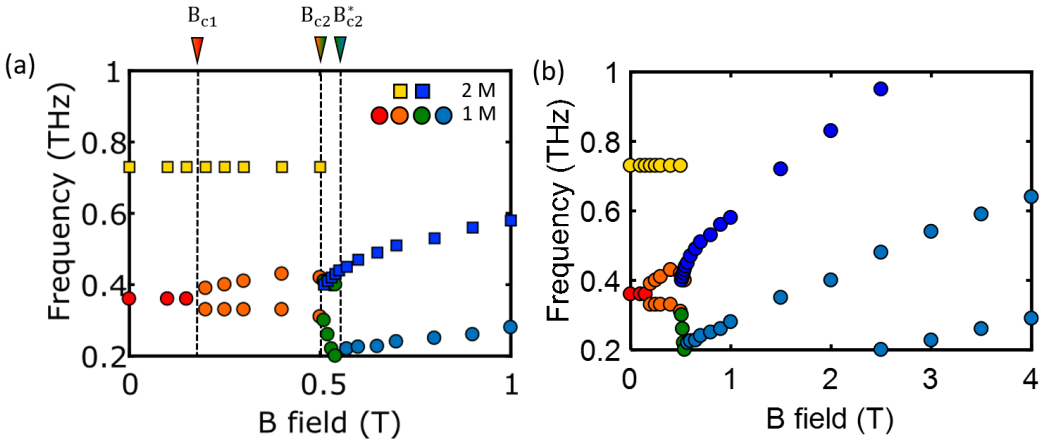

Figure 5.12: The energy of the one and two magnon exictations versus magnetic field (a) from 0 to 1 T. (b) from 0 to 4 T. Yellow squares represent two magnon excitations below B_{c2}. Red points are one magnon excitations in the spiral ordered state, which split into two branches in the colinear ordered state, represented by orange points. Green points represent the one magnon excitations in the possible field induced spin liquid regime. Dark blue squares represent the two magnon excitations above B_{c2} and light blue points represent one magnon excitations in the field polarized regime.

Applying B along a^* gives similar results to $a \parallel B$. Fig. 5.13(a) and (b) shows the results for $h \parallel B$ and $h \perp B$, respectively.

5.2.4 Depicting the Phase Diagram

The phase diagram of $BaCo_2(AsO_4)_2$ can then be obtained and is shown in Fig. 5.14. Below $T_N \sim 5.5$ K, upon applying field, $BaCo_2(AsO_4)_2$ will have a phase transition from the spiral ordered state (S) to colinear ordered state (C) at $B_{c1} \sim 0.2$ T, followed by a transition to the field induced Kitaev spin liquid regime (K) at $B_{c2} \sim 0.5$ T, and ultimately into the field polarized regime above

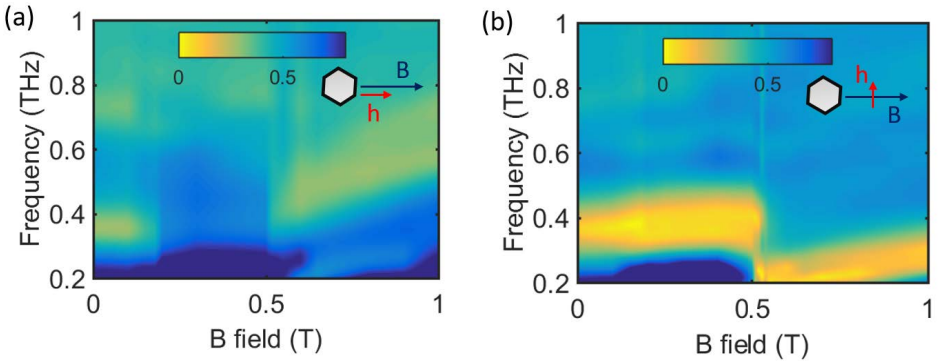

Figure 5.13: The image plot of the transmission as a function of magnetic field and frequency at 2 K for B along a^*. (a) $h \parallel B$ with B field from 0 to 1 T. (b) $h \perp B$ with B field from 0 to 1 T.

$B^*_{c2} \sim 0.55$ T. In the intermediate temperature regime, $BaCo_2(AsO_4)_2$ is a Kitaev paramagnet. It is connected continuously to the field polarized regime and conventional paramagnetic state with applying field and increasing temperature, respectively.

5.3 Conclusion

I performed THz spectroscopy on a Cobalt based Kitaev spin liquid candidate $BaCo_2(AsO_4)_2$. A broad continuum is observed in the transmission spectrum and susceptibility spectrum, extending up to 1 THz. The continuum has unusual temperature behaviours. It persists below the transition temperature despite a reduction of spectral weight, which is in contrast to conventional magnon excitations and is considered to originate from the fractional-

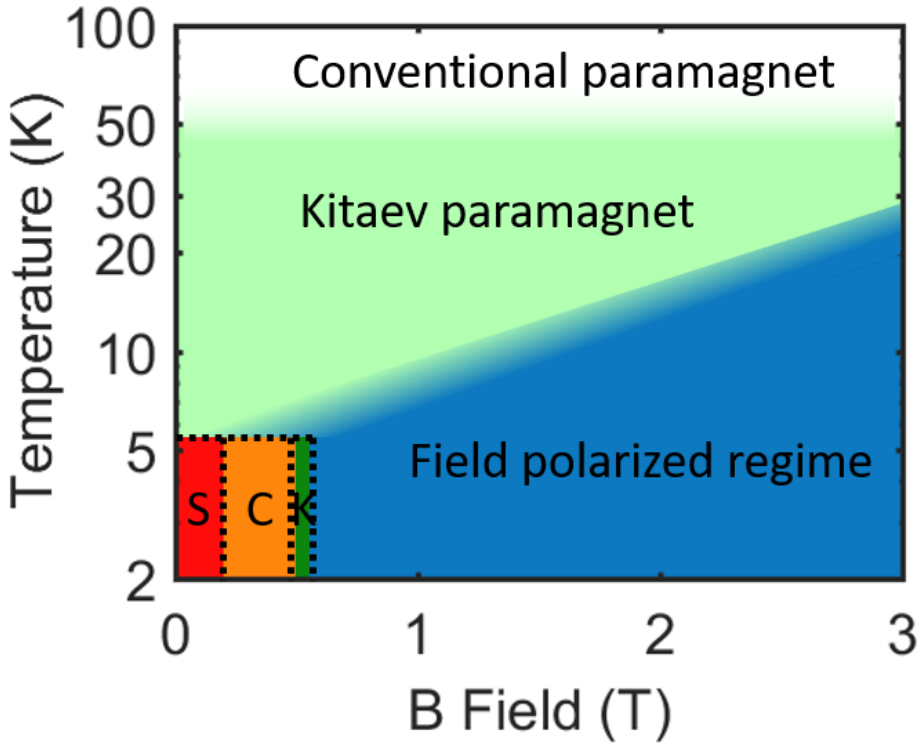

Figure 5.14: The phase diagram of $BaCo_2(AsO_4)_2$ with in-plane magnetic field. The spiral ordered state (S) is painted by red. The co-linear ordered state (C) is painted by orange. The field induced Kitaev spin liquid regime (K) is painted by dark green. The Kitaev paramagnet is in light green. The field polarized state is in blue. The conventional paramagentic state is in white.

ized Majorana excitations. The continuum is very stable upon increasing temperature consistent with the thermodynamics of the Kitaev model. I found in the so called Kitaev paramagnetic state, increasing temperature or applying magnetic field makes a smooth connection between such novel state and the conventional paramagnetic state and the field polarized state. The magnetic phases at low temperature are also studied and a potential field induced spin liquid state is found. The critical field to suppress the non-Kitaev terms is

much smaller compared with other Kitaev spin liquid candidates. The dominant Kitaev interactions along with absence of disorder makes $BaCo_2(AsO_4)_2$ a better realization of the Kitaev spin liquid among other compounds.

Chapter 6

Probing the Magnetic Excitations in $Yb_2Ti_2O_7$

The pyrochlore magnet $Yb_2Ti_2O_7$ shows exotic magnetic properties due to the highly frustrated structure and complicated exchange interactions. We study the evolution of its $\mathbf{q} = 0$ magnetic excitations as a function of magnetic field and temperature using time-domain THz spectroscopy (TDTS). We perform a thorough sum rule analysis of the low energy excitations and determine the spectral weight of magnetic excitations accurately by combining TDTS and dc susceptibility measurements. At high magnetic fields, well defined spin wave excitations are observed. At low magnetic fields, quantum fluctuations are enhanced and two magnon decay processes take place as evidenced by the distribution of spectral weight. We also show the very different

manifestation of thermal versus quantum fluctuations in this compound. Although an accurate quasi-particle residue is hard to evaluate, the ratio of the spectral weight has similar trend as quasi-particle residue and shows a new way forward in studying frustrated magnetism.

6.1 Introduction

6.1.1 Quantum Magnet $Yb_2Ti_2O_7$

The ground state of pyrochlore $Yb_2Ti_2O_7$ was disputed for many years .It was once believed to be quantum spin ice (QSI) based on the high field spin wave fit and proposed to host magnetic monopoles and Dirac strings in $Yb_2Ti_2O_7$ [32, 35, 91, 143–145]. Later people deemed $Yb_2Ti_2O_7$ as a canted ferromagnet but is very close to a phase boundary with the ψ_3 antiferromagnetic phase based on a re-evaluated spin Hamiltonian. [31, 106, 146–149]. However, recent experiments on high quality single crystals $Yb_2Ti_2O_7$ suggest the ground state is ferromagnetic long range order coexisting with short range anti-ferromagnetic correlation [33,34,107]. Instead of well defined spin wave excitations below the phase transition, a broad continuum was observed in neutron scattering, indicating strong quantum fluctuations and exotic magnetic excitations [31, 148, 150–156]. Hence, although $Yb_2Ti_2O_7$ may not be QSI or QSL, it still deserves

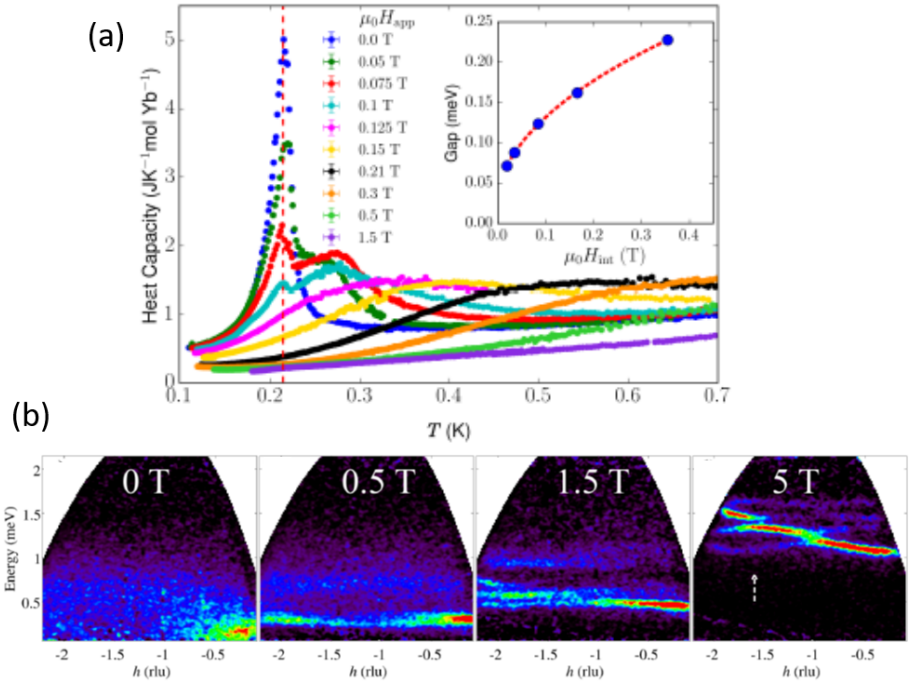

Figure 6.1: (a) The heat capacity of $Yb_2Ti_2O_7$ with different external magnetic fields. At zero field, there is a sharp peak slightly above 200 mK, indicating a phase transition to an ordered state. With applying magnetic field, the peak is suppressed and moving to higher temperature. (b) Evolution of magnetic excitations as a function of magnetic field at 0.15 K. At 5 T, the spin waves are clear in the field polarized regime. At zero field, neutron scattering shows a broad continuum in the ordered state. Figures are from Ref. [31].

further investigations.

6.1.2 Quasi-particle Residue

The idea of quasi-particle was developed by Landau in the context of interacting Fermi system known as Fermi liquid theory [157, 158]. With adiabatically switching on interactions between particles (electrons), this process

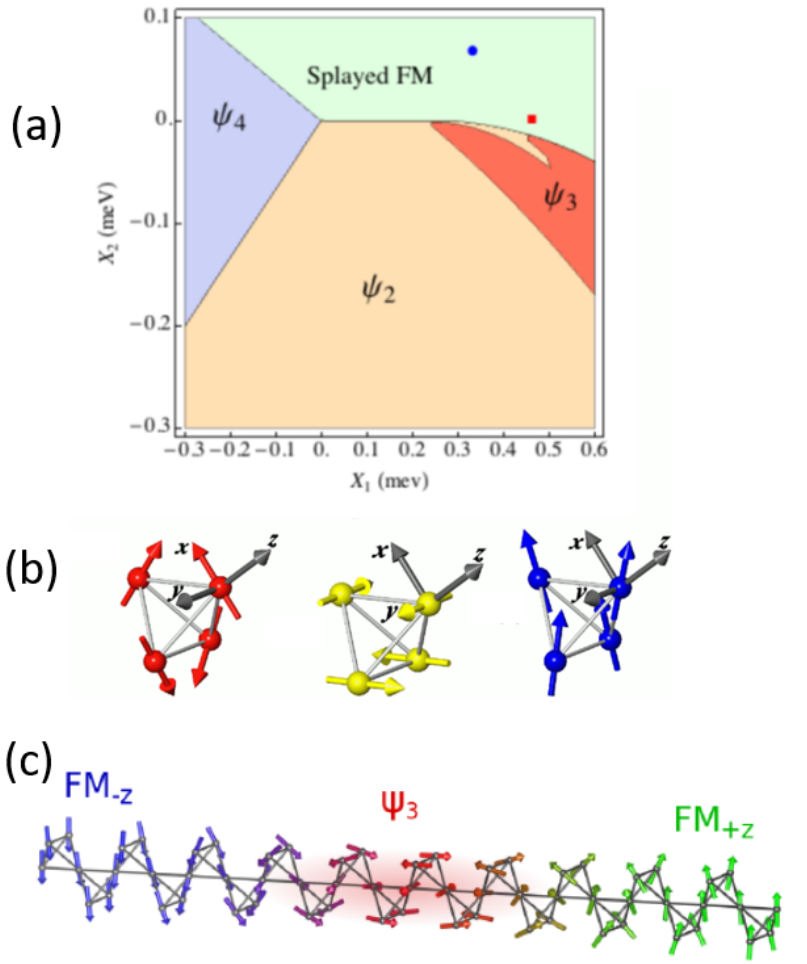

Figure 6.2: (a) The phase diagram for $Yb_2Ti_2O_7$ in the space of anisotropic interactions. The blue point represents the parameters obtained by K. Ross [32] and red square is by R. Coldea [31]. (b) The spins pointing along the local x axis in red are the ψ_2 phase. Spins in ψ_3 phase pointing along their local y axis are represented by yellow arrows. The spins of the splayed FM states are canted away from a global cubic axis by the same angle towards their local z axis. (c) The domain wall structure in $Yb_2Ti_2O_7$, suggesting the coexistence of ferro-magnetic and anti-ferromagnetic phases. Figures are from Ref. [31, 33, 34].

gives ”dressed” particles that have a finite quantum mechanical overlap amplitude with the non-interacting excitations and are hence in one-to-one correspondence with them. The degree of quantum mechanical overlap is called quasi-particle residue. Quasi-particle residue can be used as an indicator of quantum fluctuation. With no interactions present, the quasi-particle residue approaches 1 and the quasi-particles have infinite lifetime. If the interactions between particles are turned on, the quasi-particle residue decreases with renormalized mass and finite lifetime. The quasi-particle picture breaks down if the residue goes to zero.

The quasi-particle residue was originally introduced in metallic system with electrons and was discussed intensely in the context of angle-resolved photoemission [159]. Later this concept has been extended to magnetic systems with bosonic particles (magnons). One example would be the interacting transverse field Ising model: in the high magnetic field limit where the spins are fully polarized, the residue is 1, but it goes to zero as one approaches the critical point from above [160, 161]. Another example is the spontaneous magnon decay.

6.1.3 Magnon Decay

Magnon decay may occur if a cubic term in spin Hamiltonian that couples one magnon and two magnon is allowed [162–168]. In the case of a collinear antiferromagnet, the rotational symmetry about a local z axis prohibits the

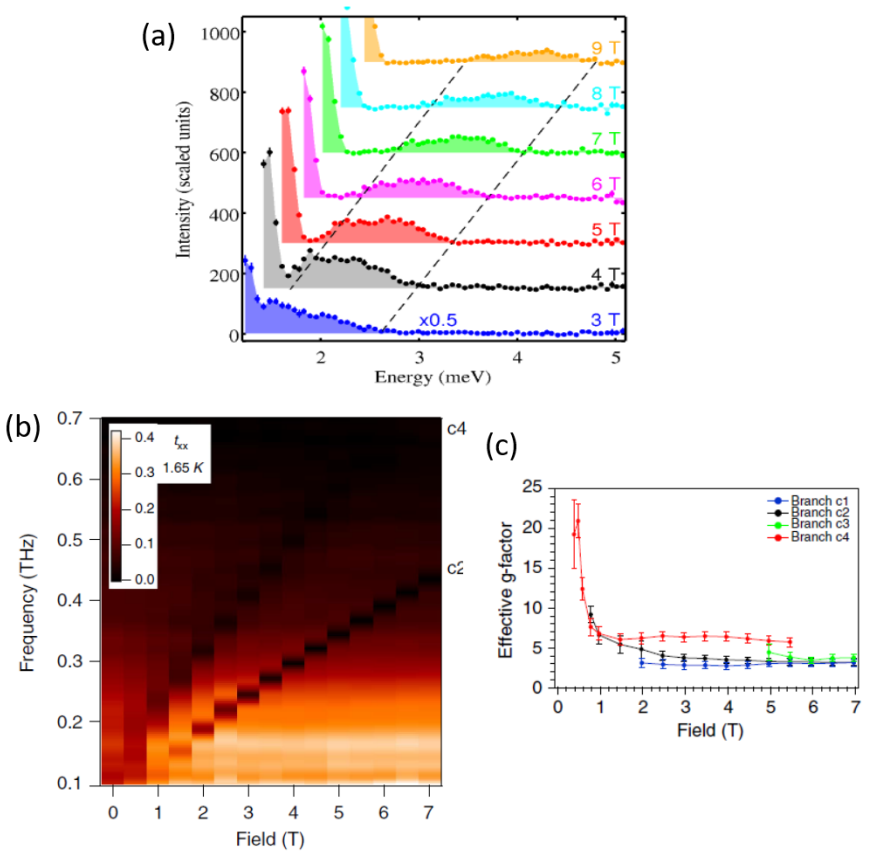

Figure 6.3: (a) The intensity and energy of one magnon and two magnon excitations with different magnetic fields in $Yb_2Ti_2O_7$. One and two magnon overlap at low fields and the spectral weight of one magnon transfers to two magnon continuum. (b) Field dependence of one magnon and two magnon excitations, showing a notable curvature at low fields. (c) Increase of g factor at low fields. Figures are from Ref. [31, 35].

cubic terms. A single magnon state preserves an odd parity under the π rotation about the z axis. On the other hand, the two-magnon states are invariant under this symmetry operation. Consequently, the coupling between one and two particle sectors is strictly forbidden in collinear antiferromagnets and the cubic terms do not occur in their effective bosonic description. Due to the lack

of this anharmonicity linear spin wave theory works well for collinear magnet because only smaller quartic terms are allowed. In contrast, the cubic terms can be present if the spin-rotational symmetry is broken, i.e., the magnetic structure becomes non-collinear. This can be realized with spin canting in an applied magnetic field or because of competing interactions in frustrated antiferromagnets. In the case of pyrochlore $Yb_2Ti_2O_7$, spins are non-collinear so the spontaneous magnon decays are allowed without magnetic fields. At high magnetic field the magnons are well defined, while at low magnetic field the single magnon can interact with two magnon, leading to a magnon decay. This can be seen as the overlap between the sharp single magnon excitations and the two magnon continuum at low field. A substantial increase of g factor with notable curvature at low fields was also observed, which was interpreted as the evidence of quantum strings [35]. However, this can also be explained in terms of magnon decays with renormalized effective magnon energies and spectral weight transferred from single magnon to the two magnon continuum. This will correspond to a decrease of the quasi-particle residue.

6.1.4 Quantifying the Quasi-particle Residue

In order to quantify the quasi-particle residue, we need to first introduce the spectral function $A(\omega)$, which is essentially the imaginary part of the single

particle Green's function

$$A(\omega) = -\frac{1}{\pi}\mathrm{Im}G(\omega), \tag{6.1}$$

where $G(\omega)$ is the Fourier transform of the retarded single particle defined as

$$G(x,t;x',t') = -i\Theta(t-t')\langle[\psi(x,t),\psi(x',t')]_{\pm}\rangle, \tag{6.2}$$

where the upper sign is for fermions and it is anticommutator, while the lower sign is for bosons and it is ordinary commutator. $\Theta(t-t')$ is the Heaviside step function with 1 and 0 for $t > t'$ and $t < t'$, respectively [169]. $\psi(x,t)$ is the field operator in many body physics.

$A(\omega)$ can be interpreted as a probability density. $A(\omega)$ is the probability that a particle will be found at an energy in an infinitesimal energy window $d\omega$ at ω. Therefore, the spectral function has a sum rule as

$$\int_0^\infty A(\omega)d\omega = 1. \tag{6.3}$$

In general, the spectral function is energy and momentum dependent, but here we only deal with optics with q=0, so we neglect the momentum dependence and only take into account the energy.

The quasi-particle appears as a pole in the analytic continuation of the Green function with quasi-particle residue. For simplicity, we can describe the

quasi-particle Green function with a coherent Lorentian peak and incoherent broad background as

$$G(\omega) = \frac{Z}{\omega - \omega_0 + i\Gamma} + G_{incoh}, \tag{6.4}$$

where the Z is quasi-particle residue, Γ is the width of the peak and G_{incoh} represents incoherent background. In non-interacting system at low temperature, there is only coherent part and $A(\omega)$ is a pure $\delta(\omega - \omega_0)$ function with Z = 1. As we introduce interactions or increase temperatures, the quasi-particle peak becomes broader with decreasing quasi-particle residue, which is transferred to the incoherent part. The integral of the coherent part of the spectral function gives Z.

As shown above, in order to obtain the quasi-particle residue we need to integrate the spectral function over whole frequency range. The Green function is just a response function, which is proportional to the magnetic susceptibility in the context of linear response formalism for magnetic systems. Hence, by integrating the absorption peaks in Imχ we can compute the quasi-particle residue. However, there are two main difficulties in reality.

First, any integration should cover a frequency range from zero to infinity, which is impossible to realize for experiments. However, as we will show, we can use a sum rule analysis with a combination of complex susceptibility in THz and dc susceptibility to overcome this frequency limitation. The excitations in Im$\chi(\omega)$ at low frequency, which is inaccessible by THz, can be related

to Re$\chi(\omega = 0)$ by the Kramers-Kronig relation. Re$\chi(\omega = 0)$ can be obtained in regular dc susceptibility measurements. Thus by combining THz spectroscopy and dc susceptibility measurements, we can determine the spectral weight of quasi-particles (one magnon) and incoherent background (two magnon continuum and incoherent thermal background).

Second, the spectral function $A(\omega)$ is discussed with respect to the local spin frame, while the observed quantity Imχ is with respect to the global laboratory frame [162, 166, 168]. As a result, the experimental spectra in global reference for the non-collinear spins in $Yb_2Ti_2O_7$ inevitably contain a mixture of transverse component (one magnon) and longitudinal component (two magnon) in local reference. The proportionality between the spectral function $A(\omega)$ and Imχ is different for transverse component and longitudinal component. For collinear spins with pure transverse or longitudinal component in the spectra (the local and global reference frame are the same), the quasi-particle residue Z is just the renormalized the spectral weight of one magnon. In contrast, for non-collinear spins as the case in $Yb_2Ti_2O_7$, we can not renormalize the spectral weights for one magnon and two magnon since they have different proportionalities (i.e. the pre-facors can not be divided out) [162, 166, 168]. Solving this problem is non-trivial.

One way is to calculate the spin orientations and ground state using Monte Carlo simulation based on exchange parameters, then we can decompose the

Imχ in our spectra into local transverse and longitudinal component in the local spin frame, and relate them to spectral function with different pre-factors. From the discussion with Chernyshev the author of Ref. [162, 166, 168], we understand it it not an easy task especially for pyrochlores and decide not to pursue it. Although we may not be able to determine the quasi-particle residue accurately, the obtained spectral weight can still be useful and provide important information for $Yb_2Ti_2O_7$. Our analysis still allows an assessment of the relative amount of spectral weight in one and multi-magnon features.

6.2 Experimental Methods

6.2.1 High Quality Single Crystals

One of the greatest obstructions to probe the true nature of the ground state in $Yb_2Ti_2O_7$ has originated in the difficulty of growing pure single crystals [170, 171]. Crystals grown by traditional floating zone method suffered from non-stoichiometry and various defects including stuffing (i.e. Yb point defects) and extended defects (e.g., dissociated superdislocations) resulting in distortions of Yb tetrahedron [172]. Recent advances have been made with regards to high quality crystal growth of this material. All single crystals used in this work were grown under identical conditions with the new developed

traveling-solvent floating zone method [108]. A cylindrical $Yb_2Ti_2O_7$ single crystal ($5 \times 4 \times 0.45$ mm^3) was used in TDTS measurements and a small cubic $Yb_2Ti_2O_7$ single crystal was measured in the PPMS. The same external magnetic field can result in different internal magnetic fields for different shapes of samples due to demagnetization effect. Hence, we need to do demagnetization corrections to obtain the internal magnetic field if we would like to combine THz spectroscopy and dc susceptibility measurements.

Steffen Säubert in Technische Universität München measured magnetization $M(H_{ex})$ of a large spherical crystal in vibrating coil magnetometer (VCM) to correct demagnetization effects. The internal field is obtained by

$$H_{in} = H_{ex} - NM(H_{ex}), \tag{6.5}$$

where the demagnetization factor N for a sphere is 1/3. Then we get the $M(H_{in})$, which is sample/shape independent because χ_{in} only depends on the material itself. Once we have the sample independent $M(H_{in})$, we can now solve the equation

$$H_{in} = H_{ex} - NM(H_{in}) \tag{6.6}$$

for H_{in} numerically at each H_{ex}. Then corresponding $B_{in} = \mu_0 H_{in}$ for different shapes of samples can be obtained in PPMS and TDTS measurement [106]. The demagnetization factor N for a $5 \times 4 \times 0.45$ mm^3 single crystal used in

TDTS with in-plane field ≈ 0.1 [173–175]. Although the actual demagnetizing factor varies from the edge to the center of the sample, this inhomogeneity can be neglected considering the small demagnetization factor. In fact the demagnetization corrections have only small impact to our results. For instance, the difference between B_{ex} and B_{in} at 7 T is around 0.1-0.2 T in TDTS measurements.

6.2.2 THz Spectropscopy and dc Susceptibility Measurements

TDTS measurements were performed with temperature down to 2 K with external magnetic fields up to $\mathbf{H_{dc}}$=7 T in Voigt geometry (k $\perp$ $\mathbf{H_{dc}}$), where k is the direction of light propagation. The external magnetic field was applied in-plane with $\mathbf{H_{dc}} \parallel \mathbf{h_{ac}}$, where $\mathbf{h_{ac}}$ is the THz pulse ac magnetic field. The advantages in performing TDTS in such a Voigt geometry are twofold. First, in this particular orientation of $\mathbf{H_{dc}}$ and $\mathbf{h_{ac}}$, only one out of four one-mangon excitations is excited due to selection rules, which makes the interaction between one-magnon and two-magnon excitations much more straightforward than cases where more than one one-magnon is excited [35]. This simplifies the analysis for the spectral weight. Second, this geometry is compatible with dc susceptibility taken in the PPMS, where $\mathbf{h_{ac}} \parallel \mathbf{H_{dc}}$, which makes the sum

rule analysis legitimate. The low frequency susceptibility $\mathrm{Re}\tilde{\chi}(0_+)$ in Quantum Design PPMS was measured at 1 KHz up to 7 T. It can be considered as dc susceptibility $\mathrm{Re}\tilde{\chi}(0)$ as the frequency is much lower than THz.

6.3 Experimental Results

6.3.1 Real and Imaginary Susceptibility in THz and dc Susceptibility in PPMS

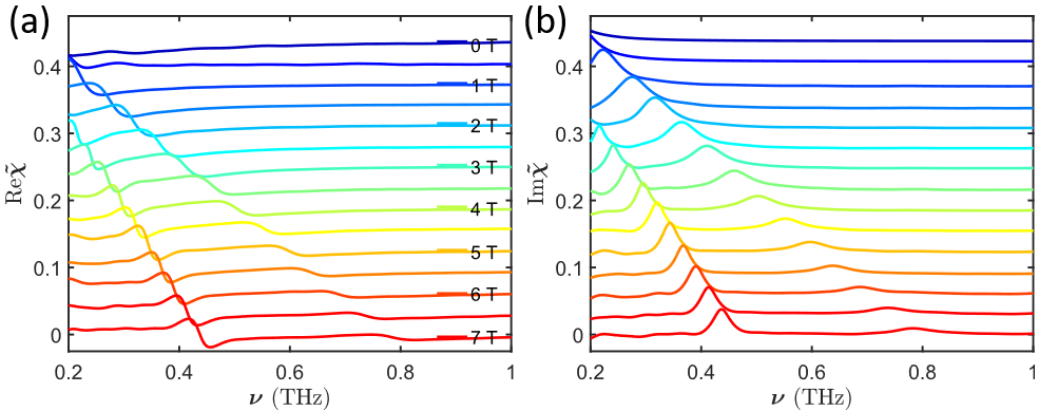

Figure 6.4: (a) Real part of the magnetic susceptibility $\tilde{\chi}(\nu)$ at different fields in Voigt geometry at 2 K. $\tilde{\chi}(\nu)$ is obtained by referencing the TDTS data to the spectra at 60 K. (b) Imaginary part of the magnetic susceptibility $\tilde{\chi}(\nu)$. Spectra are offset vertically by 0.03 for clarity.

The real and imaginary parts of the magnetic susceptibility can be calculated from the complex transmission with the method mentioned in the preceding chapter. Fig. 6.4 (a) and (b) show the real and imaginary parts of $\tilde{\chi}(\nu)$

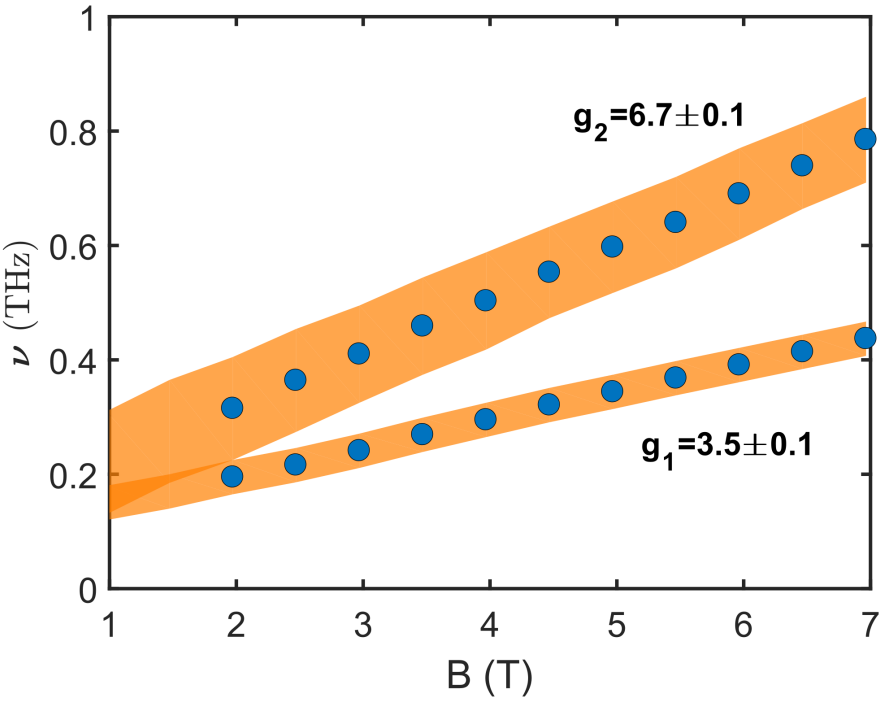

Figure 6.5: The central frequency and FWHM of one and two magnon excitations at 2 K. Blue points represent central frequency and half wdith of orange region represents the FWHM of the peaks. Both the central frequency and FWHM are obtained by fitting the excitations in real and imaginary part of susceptibility to Lorentzian functions simultaneously. Error bars are smaller than marker size.

at different fields at 2 K in the Voigt geometry, respectively. $\mathrm{Re}\tilde{\chi}(\nu)$ and $\mathrm{Im}\tilde{\chi}(\nu)$ are related by Kramers-Kronig relation. We observe two regions of excitations in $\mathrm{Im}\tilde{\chi}(\nu)$ and $\mathrm{Re}\tilde{\chi}(\nu)$. At high fields, they are well separated. As one lowers the field, the central frequencies of both shift to lower frequency, but with different rates and the two peaks merge at low frequency. The effective g-factor of the excitation with higher frequency is twice larger than the g-factor of the excitation with lower frequency as shown in Fig. 6.5. Therefore, the excitation with

lower and higher central frequency likely correspond to spin wave excitations (i.e. one magnon) and two magnon excitations in the q=0 limit, respectively.

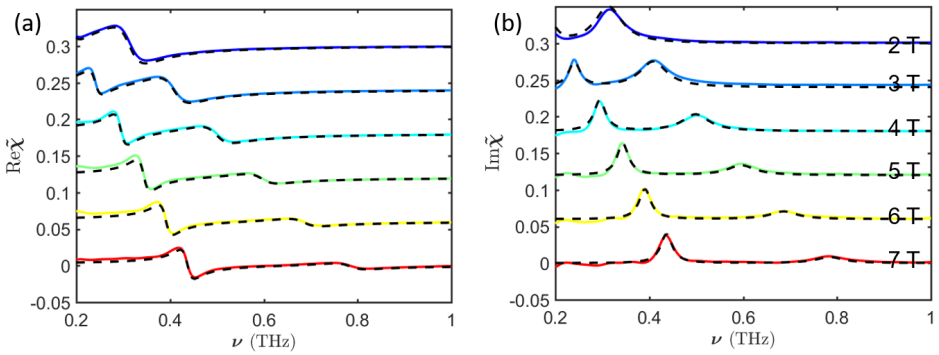

Figure 6.6: Representative Lorentzian fits to real (a) and imaginary (b) parts of the magnetic susceptibility $\tilde{\chi}(\nu)$ at different fields at 2 K. Spectra are offset vertically for clarity. Black dashed lines are Lorentzian fits.

In order to parameterize the complex susceptibility data, the excitations can be well fit by Lorentzian functions

$$\tilde{\chi}(\nu) = \frac{A(\nu_0^2 - \nu^2)}{(\nu_0^2 - \nu^2)^2 + \nu^2\Gamma^2} + i\frac{A\Gamma\nu}{(\nu_0^2 - \nu^2)^2 + \nu^2\Gamma^2}, \tag{6.7}$$

where A parametrizes the overall amplitude, ν_0 is the central frequency and Γ is the linewidth, i.e. the full width at half maximum (FWHM). The two magnon continuum can also be well fit by a Lorentzian form, but in that case the parameters like width and center frequency should be considered only parameterizations to describe the complex conductivity in a Kramers-Kronig consistent fashion. Note that the unique advantage of fitting both components of the sus-

ceptibility simultaneously is that due to the non-local nature of the Kramers-Kronig (KK) transform we are able to extract parameters more precisely over a larger field range compared to fitting the dissipative part alone [99, 130, 176]. e.g., we are sensitive to parameters like the total spectral weight of features even if their distribution in $\mathrm{Im}\tilde{\chi}$ is out of the spectral range being measured. A representative fitting plot is shown as in Fig. 6.6. The fitting parameters will be used for later calculation of $\mathrm{Re}\tilde{\chi}(0)$ and spectral weight.

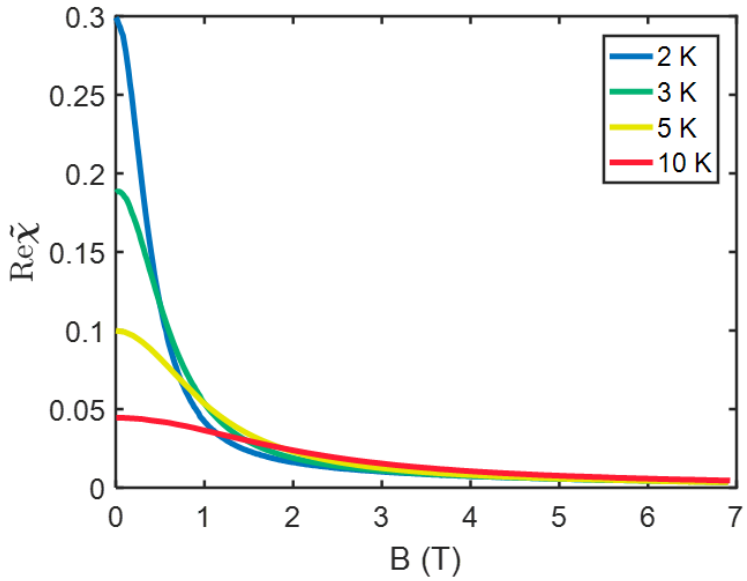

Figure 6.7: Low frequency susceptibility $\mathrm{Re}\tilde{\chi}(\nu = 1kHz)$ as function of fields at different temperatures measured in PPMS. The frequency 1 kHz in PPMS measurements is very small compared with THz frequency and can be treated as $\mathrm{Re}\tilde{\chi}(0)$ in sum rule analysis.

We measured the low frequency susceptibility $\mathrm{Re}\tilde{\chi}(0)$ in Quantum Design PPMS at 1 kHz up to 7 T as shown in Fig. 6.7. This low frequency susceptibility $\mathrm{Re}\tilde{\chi}(0)$ can be compared to various contributions from THz measurements

given by a sum rule analysis of $\mathrm{Im}\tilde{\chi}(\nu)$ weighted by $1/\nu$.

6.3.2 Sum Rule Analysis

The excellent signal to noise in THz data with very high accuracy allows us to obtain response function in absolute units and compare the THz range $\mathrm{Im}\tilde{\chi}(\nu)$ to $\mathrm{Re}\tilde{\chi}(0)$ through a sum rule derived from the KK relations. The expression

$$\mathrm{Re}\tilde{\chi}(0) = \frac{2}{\pi}\int_0^\infty \frac{\mathrm{Im}\tilde{\chi}(\nu)}{\nu}d\nu, \tag{6.8}$$

allows us to quantify the various contributions to the dc susceptibility $\mathrm{Re}\tilde{\chi}(0)$.

Through Eq. 6.8, the sum of the one and two magnon features in the TDTS spectra give the principle contributions to $\mathrm{Re}\tilde{\chi}(0)$. Fig. 6.8 (a)-(d) show the dc susceptibility along with various contributions to it as a function of magnetic field from 1 to 7 T at different temperatures from 2 to 10 K. The red curve represents the total dc susceptibility, which should be equal to the sum of all contributions. The blue points represent the one magnon ($1M$) contribution, which are only shown down to certain fields below which the one magnon excitations cannot be well resolved by TDTS due to the merging between one and two magnon excitations and moving below our measurement range. Green points represent the sum of one and two magnon ($1M + 2M$) contributions.

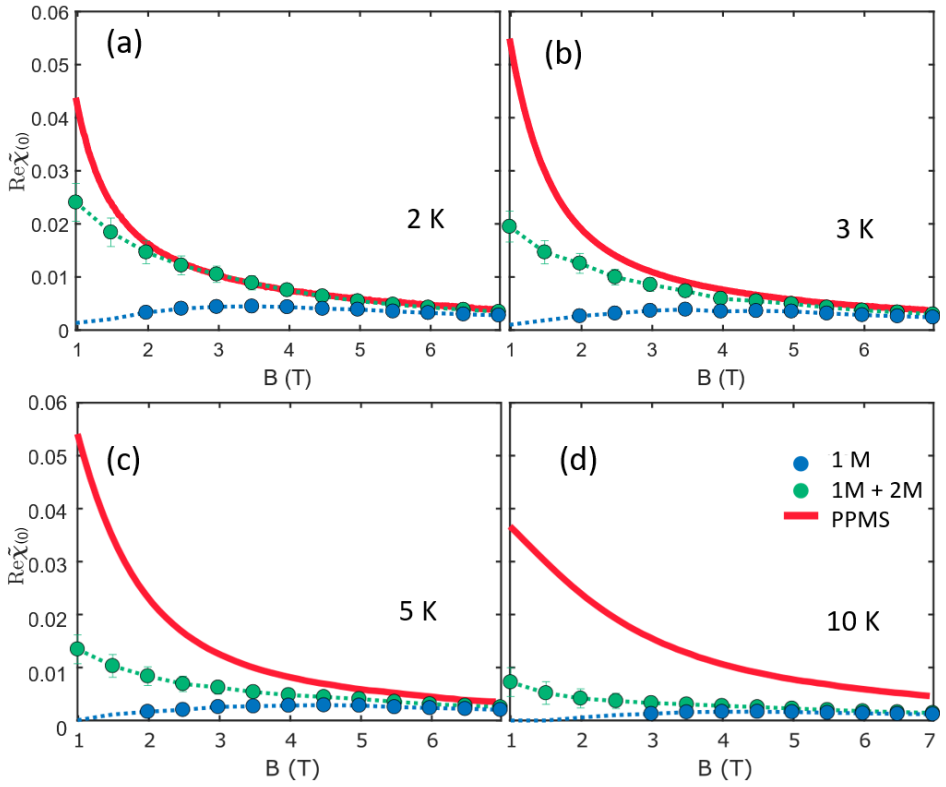

Figure 6.8: (a)-(d) Contribution of one magnon ($1M$), contribution of the sum of sum of one and two magnon ($1M + 2M$) to $\mathrm{Re}\tilde{\chi}(0)$ and total dc susceptibility (PPMS) as a function of [001] field from 1 to 7 T at different temperatures. The red curves are dc susceptibility measured from PPMS. The blue points represent the $1M$ contribution. The green points represent the $1M + 2M$ contribution and are determined precisely down to 1 T. The error bars represent one standard deviation (1 s.d.). The $1M$ error bars are smaller than the marker size.

Although we can not get one and two magnon contributions individually at low field and low frequency, notably we can resolve their total spectral weight down to lower fields than we can resolve them separately. This again is due to the KK interrelation between the complex components of $\tilde{\chi}(\nu)$, following from the fact that the high frequencies of $\mathrm{Re}\tilde{\chi}(\nu)$ is governed largely by the spectral

weight in $\mathrm{Im}\tilde{\chi}(\nu)$ at lower frequencies. Hence, by the simultaneous fitting to real and imaginary susceptibility, we can obtain the $1M$ contribution and the $1M + 2M$ contribution to dc susceptibility denoted by the blue and green color, respectively. As shown in Fig. 6.8 (a)-(d) both the one and two magnon contributions decrease with increasing temperature. At low temperature (2 K) and high fields (above 2 T), the green points overlap with the red curve well, suggesting that the $1M$ and $2M$ excitations are the dominant contributions to $\mathrm{Re}\tilde{\chi}(0)$. We expect there is only weak temperature dependence below 2 K but above the transition temperature 270 mK, which is accordance with other experiments and calculated mean field transition temperature [32, 91, 149]. However, at higher temperatures and lower fields the $1M + 2M$ contribution starts to deviate from the dc value showing that there is finite frequency spectral weight due to fluctuations not captured by the fitting discussed above.

Increasing temperature and decreasing magnetic field induce thermal and quantum fluctuations, respectively. Both deplete magnetic features and transfer spectral weight into a broad featureless background, which is not captured by the sharp Lorentzian functions. The broad background of fluctuations superimposed on sharp magnetic peaks in $\mathrm{Im}\tilde{\chi}(\nu)$ cannot be determined by TDTS alone, but their existence can be revealed by combining TDTS and dc susceptibility measurements using this sum rule analysis.

6.3.3 Quantum and Thermal Fluctuations

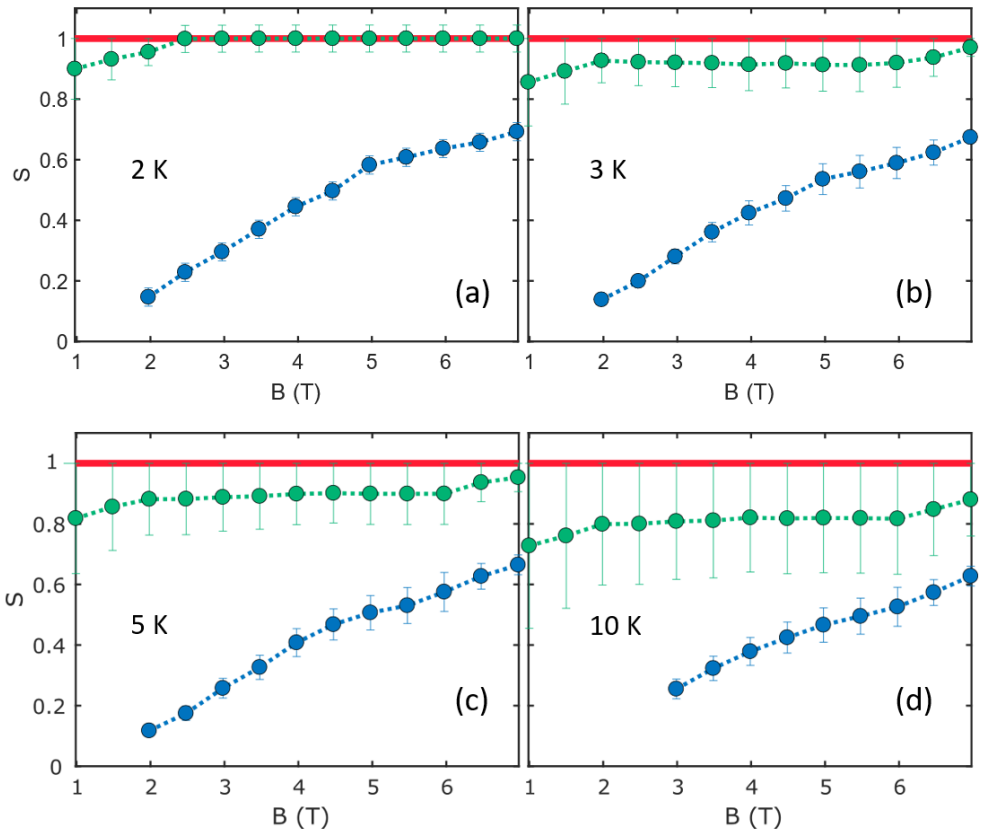

Figure 6.9: (a)-(d) Normalized spectral weight of each component as a function of [001] field from 1 to 7 T at different temperatures. The blue points and green points represent the S_1 and $S_{12} = S_1 + S_2$, respectively. The spectral weight is normalized to 1 denoted by a red horizontal line. The large error bars in (d) are due to the fact that the spectral weight of fluctuation is hard to determine as a range of parameters can reconcile with the broad background.

Now we try to estimate the spectral weight of this fluctuation contribution, which we define as the spectral contribution which is in neither the magnon or two magnon features. We use the two Lorentzian functions to model the $1M$ and $2M$ excitations as in Eq. 6.7 and a third broad Lorentzian function

to model the fluctuations contribution. In principle even higher order multi-magnon peaks can appear, but there is no evidence for them up to energies of 10 times the single magnon energies. In the fits we set a constraint that the sum of central frequency and width of the fluctuation is less than six times the one magnon energy. This is a reasonable assumption since we expect the tail of this fluctuation can not extend up to that high energy. The energy scale that corresponds to temperature (10 K $\sim$ 0.2 THz) is also less than this bound. Under this constraint, we fit these three Lorentzian functions to the real, imaginary and dc susceptibility simultaneously. The parameters obtained for one and two magnon are essentially same as before. We obtain a range of parameters on the fluctuation contribution to the susceptibility, all of which give reasonable fits. Then we are able to determine the spectral weight for each contribution. An extension to the analysis above allows us to determine the normalized spectral weight, which is defined as

$$S_1 = \int_0^\infty \mathrm{Im}\tilde{\chi}_{1M}(\nu)d\nu / \int_0^\infty \mathrm{Im}\tilde{\chi}(\nu)d\nu \tag{6.9}$$

for the normalized spectral weight of the $1M$ peak and

$$S_2 = \int_0^\infty \mathrm{Im}\tilde{\chi}_{2M}(\nu)d\nu / \int_0^\infty \mathrm{Im}\tilde{\chi}(\nu)d\nu \tag{6.10}$$

for the normalized spectral weight of the $2M$ continuum. $\mathrm{Im}\tilde{\chi}_{1M}(\nu)$ and $\mathrm{Im}\tilde{\chi}_{2M}(\nu)$

can be obtained from the parameters determined from the complex fitting procedure described above. The denominator is the total spectral weight, including not only the spectral weight of well defined magnetic excitations, but also the fluctuation contribution given by the third Lorentzian.

Fig. 6.9 (a)-(d) show the normalized spectral weight of the $1M$ component and the sum of $1M + 2M$ as a function of [001] field at different temperatures. Upon increasing temperature, the thermal fluctuations become stronger and both one and two magnon spectral weights decrease. At a given temperature, as one decreases the magnetic field, the one magnon spectral weight is suppressed and both the two magnon and fluctuation contributions gain more spectral weights. The renormalized one magnon spectral weight S_1 should bear similar physical implications as the quasi-particle residue Z despite being not exactly the same. The decreasing of S_1 at low field reflects the strong quantum fluctuations and interactions between one magnon and two magnon excitations (i.e. magnon decays). Temperature effectively induces interactions and might also renormalize magnon energies and broaden the linewidth, which gives similar effects as to lowering magnetic field as shown in Fig. 6.10.

Then one may ask what's the difference between quantum and thermal fluctuations? Here we show the different manifestations between quantum (i.e. decreasing fields) and thermal (i.e. increasing temperatures) fluctuations shown in the distribution of spectral weight. By lowering the field, one magnon peaks

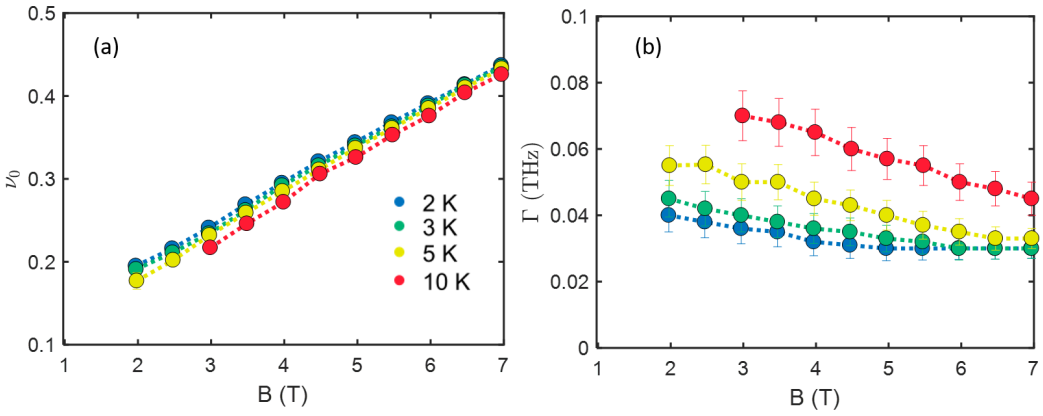

Figure 6.10: (a) The one magnon peak position and (b) FWHM as a function of magnetic field at different temperatures.

are suppressed and the two magnon features are enhanced. The quantum fluctuations transfer the one magnon spectral weight to the two magnon. On the other hand, with increasing temperature, both the one and two magnon peaks are suppressed, whose spectral weights are transferred to an incoherent thermal background. In Fig. 6.10, I plot the ratio of S_1/S_{12} as a function of field at different temperatures, where $S_{12} = S_1 + S_2$. This shows distinct behaviours of the distribution of spectral weight with respect to temperatures and fields. Temperatures do not change the ratio, while fields impact the ratio significantly. This is in contrast to the widths and energies.

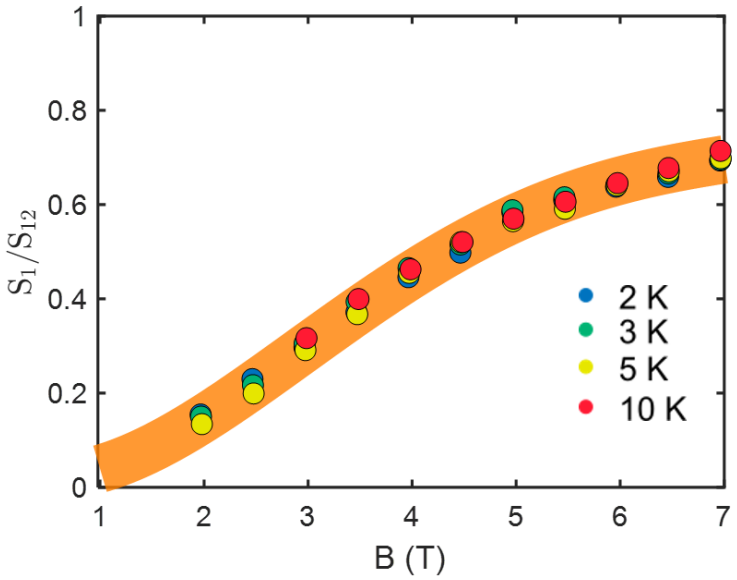

Figure 6.11: The ratio of S_1/S_{12} as a function of field at different temperatures. The orange curve is a guide to eyes. Temperatures do not change the ratio, while fields impact the ratio significantly.

6.4 Conclusion

I performed a comprehensive sum rule analysis using a combination of TDTS and dc susceptibility measurements in high quality $Yb_2Ti_2O_7$ single crystals. We have showed the evolution of magnetic excitations and fluctuations as a function of temperature and magnetic field. At low temperature and high magnetic field, one and two magnon excitations are the primary contributions to the dc susceptibility. As one lowers the magnetic field, the interactions between one and two magnon features are enhanced, thereby the magnon decay process occurs as evidenced by the renormalized energies, broadened linewidths and reduced one magnon spectral weights, suggesting strong

quantum fluctuations. As one increases the temperature, although the energies and linewidths still change, surprisingly the ratio of S_1/S_{12} remains unchanged, showing that thermal fluctuations affect the coherence of both excitations equally. In contrast, quantum fluctuations evidence themselves as a transfer of spectral weight from the single magnon peak to the two magnon continuum. This ratio has distinct responses to thermal and quantum fluctuations.

Chapter 7

Summary

In this thesis, I used time domain terahertz spectroscopy (TDTS) to study various frustrated magnetic systems and show that TDTS becomes an even more powerful technique when combined with other techniques. In chapter 2, I introduced our technique and data analysis. In chapter 3, I showed my work on a triangular spin liquid candidate $YbMgGaO_4$. The previous sets of exchange parameters were controversial due to certain limitations of the techniques used. By combining TDTS and neutron scattering, I fit both THz and neutron scattering data to the linear spin wave simultaneously and further constrain the parameters by a linewidth analysis. As a result, I am able to determine the exchange constants and g-factors accurately. Our work places the $YbMgGaO_4$ closer to the spin liquid regime than previously thought.

In chapter 4, I studied the low energy crystal field excitations of a 3 di-

mensional spin liquid candidate $Tb_2Ti_2O_7$. Upon applying [111] magnetic field, several crystal field excitations were observed in left and right circular basis according to optical selection rules. Several crystal field anomalies were observed, which were interpreted as a structural phase transition. With crystal field calculations based on the single ion physics, I can reproduce the general features of our data and explain the anomalies by the low energy crystal field hybridization. However, the quantitative disagreement between calculations and data is obvious and can only be explained by considering a field dependent crystal field Hamiltonian. This field induced change of crystal field environment indicates the strong spin-lattice coupling in $Tb_2Ti_2O_7$.

In chapter 5, I demonstrated a new proximate Kitaev spin liquid candidate $BaCo_2(AsO_4)_2$. A broad continuum near Γ point, which is predicted by the Kitaev model, was observed by THz spectroscopy. The continuum is consistent with the excitations from fractionalized Majorana fermions in the Kitaev model. In addition, the continuum persists up to very high temperatures, again consistent with the thermodynamics of the Kitaev model. Increasing temperature or applying magnetic field can turn the Kitaev paramagnet into conventional paramagnetic state or the field polarized regime smoothly. The one and two magnon excitations below the transition temperature show interesting behaviours with applying magnetic field. This material exhibits a rich phase diagram at low temperatures under magnetic fields and within a narrow field

range a field induced spin liquid phase is observed. Because $BaCo_2(AsO_4)_2$ has relatively large Kitaev interactions and less disorder, we believe it is an excellent candidate for a Kitaev spin liquid.

In chapter 6, I combined dc susceptibility measurements and THz spectroscopy to study the evolution of the $q = 0$ magnetic excitations in a pyrochlore compound $Yb_2Ti_2O_7$. At high field, the magnon excitations are well defined and separate, while at low field, one and two magnon excitations tend to overlap, indicating a magnon decay process. I performed a sum rule analysis to determine the spectral weight of magnetic excitations accurately. The normalized quasi-particle spectral weight is considered to be a quantity similar to the quasi-particle residue, which can be used to evaluate the strength of quantum fluctuations.

In future, I think the candidate $BaCo_2(AsO_4)_2$ deserves more attentions and various experiments such as neutron scattering and thermal Hall measurements may be helpful to probe this material. Other perturbations such as pressure or light may also suppress the non-Kitaev terms and give rise to the true Kitaev spin liquid. For instance, a tunable pump laser with particular energy may destroy the non-Kitaev term and leave the Kitaev terms intact, leading to a light induced Kitaev spin liquid.

Bibliography

[1] J. A. M. Paddison, M. Daum, Z. Dun, G. Ehlers, Y. Liu, M. B. Stone, H. Zhou, and M. Mourigal, "Continuous excitations of the triangular-lattice quantum spin liquid $YbMgGaO_4$," *Nature Physics*, vol. 13, no. 2, pp. 117–122, dec 2016. [Online]. Available: https://doi.org/10.1038%2Fnphys3971

[2] Y.-D. Li, Y. Shen, Y. Li, J. Zhao, and G. Chen, "The effect of spin-orbit coupling on the effective-spin correlation in $YbMgGaO_4$," *Physical Review B*, vol. 97, no. 12, p. 125105, 2018.

[3] M. Ruminy, E. Pomjakushina, K. Iida, K. Kamazawa, D. T. Adroja, U. Stuhr, and T. Fennell, "Crystal-field parameters of the rare-earth pyrochlores $R_2Ti_2O_7$ (R = Tb, Dy, and Ho)," *Phys. Rev. B*, vol. 94, p. 024430, Jul 2016. [Online]. Available: https://link.aps.org/doi/10.1103/PhysRevB.94.024430

[4] L. Balents, "Spin liquids in frustrated magnets," *Nature*, vol. 464, no.

7286, pp. 199–208, 2010.

[5] H. Takagi, T. Takayama, G. Jackeli, G. Khaliullin, and S. E. Nagler, "Concept and realization of Kitaev quantum spin liquids," *Nature Reviews Physics*, vol. 1, no. 4, pp. 264–280, 2019.

[6] S. T. Bramwell and M. J. Gingras, "Spin ice state in frustrated magnetic pyrochlore materials," *Science*, vol. 294, no. 5546, pp. 1495–1501, 2001.

[7] T. Fennell, P. Deen, A. Wildes, K. Schmalzl, D. Prabhakaran, A. Boothroyd, R. Aldus, D. McMorrow, and S. Bramwell, "Magnetic Coulomb phase in the spin ice $Ho_2Ti_2O_7$," *Science*, vol. 326, no. 5951, pp. 415–417, 2009.

[8] L. S. Bilbro, "Fluctuations of superconductivity in $La_{2-x}Sr_xCuO_4$ measured with terahertz time-domain spectroscopy," *Ph.D. dissertation, Johns Hopkins University*, 2012.

[9] N. J. Laurita, "Low energy electrodynamics of quantum magnets," *Ph.D. dissertation, Johns Hopkins University*, 2017.

[10] L. Wu, M. Salehi, N. Koirala, J. Moon, S. Oh, and N. Armitage, "Quantized Faraday and Kerr rotation and axion electrodynamics of a 3D topological insulator," *Science*, vol. 354, no. 6316, pp. 1124–1127, 2016.

[11] C. M. Morris, R. V. Aguilar, A. V. Stier, and N. P. Armitage, "Polarization

modulation time-domain terahertz polarimetry," *Optics express*, vol. 20, no. 11, pp. 12 303–12 317, 2012.

[12] Y. Iqbal, W.-J. Hu, R. Thomale, D. Poilblanc, and F. Becca, "Spin liquid nature in the Heisenberg $J_1 - J_2$ triangular antiferromagnet," *Phys. Rev. B*, vol. 93, p. 144411, Apr 2016. [Online]. Available: https://link.aps.org/doi/10.1103/PhysRevB.93.144411

[13] Y.-D. Li, X. Wang, and G. Chen, "Anisotropic spin model of strong spin-orbit-coupled triangular antiferromagnets," *Phys. Rev. B*, vol. 94, p. 035107, Jul 2016. [Online]. Available: https://link.aps.org/doi/10.1103/PhysRevB.94.035107

[14] Y. Li, H. Liao, Z. Zhang, S. Li, F. Jin, L. Ling, L. Zhang, Y. Zou, L. Pi, Z. Yang, J. Wang, Z. Wu, and Q. Zhang, "Gapless quantum spin liquid ground state in the two-dimensional spin-1/2 triangular antiferromagnet $YbMgGaO_4$," *Sci. Rep.*, vol. 5, no. 1, nov 2015. [Online]. Available: https://doi.org/10.1038%2Fsrep16419

[15] Y. Shen, Y.-D. Li, H. Wo, Y. Li, S. Shen, B. Pan, Q. Wang, H. C. Walker, P. Steffens, M. Boehm, Y. Hao, D. L. Quintero-Castro, L. W. Harriger, M. D. Frontzek, L. Hao, S. Meng, Q. Zhang, G. Chen, and J. Zhao, "Evidence for a spinon Fermi surface in a triangular-lattice

quantum-spin-liquid candidate," *Nature*, vol. 540, no. 7634, pp. 559–562, dec 2016. [Online]. Available: https://doi.org/10.1038%2Fnature20614

[16] Y. Li, G. Chen, W. Tong, L. Pi, J. Liu, Z. Yang, X. Wang, and Q. Zhang, "Rare-Earth Triangular Lattice Spin Liquid: A Single-Crystal Study of $YbMgGaO_4$," *Phys. Rev. Lett.*, vol. 115, p. 167203, Oct 2015. [Online]. Available: https://link.aps.org/doi/10.1103/PhysRevLett.115.167203

[17] Z. Zhu, P. A. Maksimov, S. R. White, and A. L. Chernyshev, "Topography of Spin Liquids on a Triangular Lattice," *Phys. Rev. Lett.*, vol. 120, p. 207203, May 2018. [Online]. Available: https://link.aps.org/doi/10.1103/PhysRevLett.120.207203

[18] M. J. P. Gingras, B. C. den Hertog, M. Faucher, J. S. Gardner, S. R. Dunsiger, L. J. Chang, B. D. Gaulin, N. P. Raju, and J. E. Greedan, "Thermodynamic and single-ion properties of Tb^{3+} within the collective paramagnetic-spin liquid state of the frustrated pyrochlore antiferromagnet $Tb_2Ti_2O_7$," *Phys. Rev. B*, vol. 62, pp. 6496–6511, Sep 2000. [Online]. Available: https://link.aps.org/doi/10.1103/PhysRevB.62.6496

[19] J. S. Gardner, S. R. Dunsiger, B. D. Gaulin, M. J. P. Gingras, J. E. Greedan, R. F. Kiefl, M. D. Lumsden, W. A. MacFarlane, N. P. Raju, J. E. Sonier, I. Swainson, and Z. Tun, "Cooperative Paramagnetism

in the Geometrically Frustrated Pyrochlore Antiferromagnet $Tb_2Ti_2O_7$," *Phys. Rev. Lett.*, vol. 82, pp. 1012–1015, Feb 1999. [Online]. Available: https://link.aps.org/doi/10.1103/PhysRevLett.82.1012

[20] J. P. C. Ruff, B. D. Gaulin, J. P. Castellan, K. C. Rule, J. P. Clancy, J. Rodriguez, and H. A. Dabkowska, "Structural Fluctuations in the Spin-Liquid State of $Tb_2Ti_2O_7$," *Phys. Rev. Lett.*, vol. 99, p. 237202, Dec 2007. [Online]. Available: https://link.aps.org/doi/10.1103/PhysRevLett.99.237202

[21] J. P. C. Ruff, Z. Islam, J. P. Clancy, K. A. Ross, H. Nojiri, Y. H. Matsuda, H. A. Dabkowska, A. D. Dabkowski, and B. D. Gaulin, "Magnetoelastics of a Spin Liquid: X-Ray Diffraction Studies of $Tb_2Ti_2O_7$ in Pulsed Magnetic Fields," *Phys. Rev. Lett.*, vol. 105, p. 077203, Aug 2010. [Online]. Available: https://link.aps.org/doi/10.1103/PhysRevLett.105.077203

[22] V. Klekovkina and B. Malkin, "Crystal field and magnetoelastic interactions in $Tb_2Ti_2O_7$," *Optics and Spectroscopy*, vol. 116, no. 6, pp. 849–857, 2014.

[23] T. Fennell, M. Kenzelmann, B. Roessli, H. Mutka, J. Ollivier, M. Ruminy, U. Stuhr, O. Zaharko, L. Bovo, A. Cervellino *et al.*, "Magnetoelastic ex-

citations in the pyrochlore spin liquid $Tb_2Ti_2O_7$," *Physical review letters*, vol. 112, no. 1, p. 017203, 2014.

[24] F. Jin, C. Liu, Y. Chang, A. Zhang, Y. Wang, W. Liu, X. Wang, Y. Sun, G. Chen, X. Sun, and Q. Zhang, "Experimental Identification of Electric Dipoles Induced by Magnetic Monopoles in $Tb_2Ti_2O_7$," *Phys. Rev. Lett.*, vol. 124, p. 087601, Feb 2020. [Online]. Available: https://link.aps.org/doi/10.1103/PhysRevLett.124.087601

[25] A. Banerjee, C. Bridges, J.-Q. Yan, A. Aczel, L. Li, M. Stone, G. Granroth, M. Lumsden, Y. Yiu, J. Knolle *et al.*, "Proximate Kitaev quantum spin liquid behaviour in a honeycomb magnet," *Nature materials*, vol. 15, no. 7, pp. 733–740, 2016.

[26] A. Banerjee, J. Yan, J. Knolle, C. A. Bridges, M. B. Stone, M. D. Lumsden, D. G. Mandrus, D. A. Tennant, R. Moessner, and S. E. Nagler, "Neutron scattering in the proximate quantum spin liquid α-$RuCl_3$," *Science*, vol. 356, no. 6342, pp. 1055–1059, 2017.

[27] J. Nasu, J. Knolle, D. L. Kovrizhin, Y. Motome, and R. Moessner, "Fermionic response from fractionalization in an insulating two-dimensional magnet," *Nature Physics*, vol. 12, no. 10, pp. 912–915, 2016.

[28] L. J. Sandilands, Y. Tian, K. W. Plumb, Y.-J. Kim, and K. S. Burch, "Scat-

tering Continuum and Possible Fractionalized Excitations in α-$RuCl_3$," *Physical review letters*, vol. 114, no. 14, p. 147201, 2015.

[29] Z. Wang, S. Reschke, D. Hüvonen, S.-H. Do, K.-Y. Choi, M. Gensch, U. Nagel, T. Rõõm, and A. Loidl, "Magnetic Excitations and Continuum of a Possibly Field-Induced Quantum Spin Liquid in α-$RuCl_3$," *Physical review letters*, vol. 119, no. 22, p. 227202, 2017.

[30] R. Zhong, T. Gao, N. P. Ong, and R. J. Cava, "Weak-field induced nonmagnetic state in a Co-based honeycomb," *Science advances*, vol. 6, no. 4, p. eaay6953, 2020.

[31] J. D. Thompson, P. A. McClarty, D. Prabhakaran, I. Cabrera, T. Guidi, and R. Coldea, "Quasiparticle Breakdown and Spin Hamiltonian of the Frustrated Quantum Pyrochlore $Yb_2Ti_2O_7$ in a Magnetic Field," *Phys. Rev. Lett.*, vol. 119, p. 057203, Aug 2017. [Online]. Available: https://link.aps.org/doi/10.1103/PhysRevLett.119.057203

[32] K. A. Ross, L. Savary, B. D. Gaulin, and L. Balents, "Quantum excitations in quantum spin ice," *Physical Review X*, vol. 1, no. 2, p. 021002, 2011.

[33] A. Scheie, J. Kindervater, S. Zhang, H. J. Changlani, G. Sala, G. Ehlers, A. Heinemann, G. S. Tucker, S. M. Koohpayeh, and C. Broholm, "Multiphase Magnetism in $Yb_2Ti_2O_7$," *Proceedings of the National Academy of Sciences*, vol. 117, no. 44, pp. 27 245–27 254, 2020.

[34] L. D. C. Jaubert, O. Benton, J. G. Rau, J. Oitmaa, R. R. P. Singh, N. Shannon, and M. J. P. Gingras, "Are Multiphase Competition and Order by Disorder the Keys to Understanding $Yb_2Ti_2O_7$?" *Phys. Rev. Lett.*, vol. 115, p. 267208, Dec 2015. [Online]. Available: https://link.aps.org/doi/10.1103/PhysRevLett.115.267208

[35] L. Pan, S. K. Kim, A. Ghosh, C. M. Morris, K. A. Ross, E. Kermarrec, B. D. Gaulin, S. M. Koohpayeh, O. Tchernyshyov, and N. P. Armitage, "Low-energy electrodynamics of novel spin excitations in the quantum spin ice $Yb_2Ti_2O_7$," *Nature Communications*, vol. 5, p. 4970, sep 2014. [Online]. Available: https://doi.org/10.1038%2Fncomms5970

[36] M. Dressel and G. Grüner, *Electrodynamics of solids: optical properties of electrons in matter*. Cambridge University Press, 2002.

[37] D. Jiles, *"Introduction to magnetism and magnetic materials"*. CRC press, 2015.

[38] P. Weiss, "Hypothesis of the molecular field and ferromagnetic properties," *J. phys*, vol. 6, no. 4, pp. 661–690, 1907.

[39] C. Kittel, "Introduction to solid state physics," *Wiley*, 1976.

[40] C. Broholm, R. Cava, S. Kivelson, D. Nocera, M. Norman, and T. Senthil, "Quantum spin liquids," *Science*, vol. 367, no. 6475, 2020.

[41] G. Wannier, "Antiferromagnetism in the triangular Ising net," *Physical Review*, vol. 79, no. 2, p. 357, 1950.

[42] C. Lacroix, P. Mendels, and F. Mila, *Introduction to frustrated magnetism: materials, experiments, theory*. Springer Science & Business Media, 2011, vol. 164.

[43] L. D. Landau, "On the theory of phase transitions. I." *Zh. Eksp. Teor. Fiz.*, vol. 11, p. 19, 1937.

[44] V. L. Ginzburg and L. D. Landau, "On the theory of superconductivity." Springer, 2009, pp. 113–137.

[45] D. C. Tsui, H. L. Stormer, and A. C. Gossard, "Two-dimensional magnetotransport in the extreme quantum limit," *Physical Review Letters*, vol. 48, no. 22, p. 1559, 1982.

[46] R. B. Laughlin, "Anomalous quantum Hall effect: an incompressible quantum fluid with fractionally charged excitations," *Physical Review Letters*, vol. 50, no. 18, p. 1395, 1983.

[47] X.-G. Wen, "Topological orders in rigid states," *International Journal of Modern Physics B*, vol. 4, no. 02, pp. 239–271, 1990.

[48] Y. Zhou, K. Kanoda, and T.-K. Ng, "Quantum spin liquid states," *Reviews of Modern Physics*, vol. 89, no. 2, p. 025003, 2017.

[49] X.-G. Wen, "Quantum orders and symmetric spin liquids," *Physical Review B*, vol. 65, no. 16, p. 165113, 2002.

[50] L. Savary and L. Balents, "Quantum spin liquids: a review," *Reports on Progress in Physics*, vol. 80, no. 1, p. 016502, 2016.

[51] P. W. Anderson, "Resonating valence bonds: A new kind of insulator?" *Materials Research Bulletin*, vol. 8, no. 2, pp. 153–160, 1973.

[52] P. W. Anderson, "The resonating valence bond state in La_2CuO_4 and superconductivity," *Science*, vol. 235, no. 4793, pp. 1196–1198, 1987.

[53] A. Kitaev, "Anyons in an exactly solved model and beyond," *Annals of Physics*, vol. 321, no. 1, pp. 2–111, 2006.

[54] A. Y. Kitaev, "Fault-tolerant quantum computation by anyons," *Annals of Physics*, vol. 303, no. 1, pp. 2–30, 2003.

[55] J. S. Gardner, M. J. Gingras, and J. E. Greedan, "Magnetic pyrochlore oxides," *Reviews of Modern Physics*, vol. 82, no. 1, p. 53, 2010.

[56] L. Pauling, "The structure and entropy of ice and of other crystals with some randomness of atomic arrangement," *Journal of the American Chemical Society*, vol. 57, no. 12, pp. 2680–2684, 1935.

[57] W. Giauque and J. Stout, "The Entropy of Water and the Third Law of

Thermodynamics. The Heat Capacity of Ice from 15 to 273 K," *Journal of the American Chemical Society*, vol. 58, no. 7, pp. 1144–1150, 1936.

[58] A. P. Ramirez, A. Hayashi, R. J. Cava, R. Siddharthan, and B. Shastry, "Zero-point entropy in 'spin ice'," *Nature*, vol. 399, no. 6734, pp. 333–335, 1999.

[59] C. Castelnovo, R. Moessner, and S. L. Sondhi, "Magnetic monopoles in spin ice," *Nature*, vol. 451, no. 7174, pp. 42–45, 2008.

[60] N. P. Armitage, "Electrodynamics of correlated electron systems: Based on 2008 Boulder School for Condensed Matter and Materials Physics Lectures," *arXiv:0908.1126*.

[61] P. R. Smith, D. H. Auston, and M. C. Nuss, "Subpicosecond photoconducting dipole antennas," *IEEE Journal of Quantum Electronics*, vol. 24, no. 2, pp. 255–260, 1988.

[62] C. A. Werley, S. M. Teo, and K. A. Nelson, "Pulsed laser noise analysis and pump-probe signal detection with a data acquisition card," *Review of Scientific Instruments*, vol. 82, no. 12, p. 123108, 2011.

[63] N. P. Armitage, "Constraints on Jones transmission matrices from time-reversal invariance and discrete spatial symmetries," *Phys.*

Rev. B, vol. 90, p. 035135, Jul 2014. [Online]. Available: https://link.aps.org/doi/10.1103/PhysRevB.90.035135

[64] B. Cheng, "Magneto terahertz response of topological materials," *Ph.D. dissertation, Johns Hopkins University*, 2019.

[65] Z. Zhu, P. A. Maksimov, S. R. White, and A. L. Chernyshev, "Disorder-Induced Mimicry of a Spin Liquid in $YbMgGaO_4$," *Phys. Rev. Lett.*, vol. 119, p. 157201, Oct 2017. [Online]. Available: https://link.aps.org/doi/10.1103/PhysRevLett.119.157201

[66] P. A. Maksimov, Z. Zhu, S. R. White, and A. L. Chernyshev, "Anisotropic-Exchange Magnets on a Triangular Lattice: Spin Waves, Accidental Degeneracies, and Dual Spin Liquids," *Phys. Rev. X*, vol. 9, p. 021017, Apr 2019. [Online]. Available: https://link.aps.org/doi/10.1103/PhysRevX.9.021017

[67] R. R. P. Singh and D. A. Huse, "Three-sublattice order in triangular- and Kagomé-lattice spin-half antiferromagnets," *Phys. Rev. Lett.*, vol. 68, pp. 1766–1769, Mar 1992. [Online]. Available: https://link.aps.org/doi/10.1103/PhysRevLett.68.1766

[68] P. Azaria, B. Delamotte, and D. Mouhanna, "Spontaneous symmetry breaking in quantum frustrated antiferromagnets," *Phys. Rev. Lett.*,

vol. 70, pp. 2483–2486, Apr 1993. [Online]. Available: https://link.aps.org/doi/10.1103/PhysRevLett.70.2483

[69] L. Capriotti, A. E. Trumper, and S. Sorella, "Long-Range Néel Order in the Triangular Heisenberg Model," *Phys. Rev. Lett.*, vol. 82, no. 19, pp. 3899–3902, may 1999. [Online]. Available: https://doi.org/10.1103%2Fphysrevlett.82.3899

[70] M. Poienar, F. Damay, C. Martin, J. Robert, and S. Petit, "Spin dynamics in the geometrically frustrated multiferroic $CuCrO_2$," *Phys. Rev. B*, vol. 81, p. 104411, Mar 2010. [Online]. Available: https://link.aps.org/doi/10.1103/PhysRevB.81.104411

[71] S. E. Dutton, E. Climent-Pascual, P. W. Stephens, J. P. Hodges, A. Huq, C. L. Broholm, and R. J. Cava, "Helical magnetism and structural anomalies in triangular lattice $\alpha - SrCr_2O_4$," *J. Phys.: Condens. Matter*, vol. 23, no. 24, p. 246005, 2011. [Online]. Available: http://stacks.iop.org/0953-8984/23/i=24/a=246005

[72] S. Toth, B. Lake, K. Hradil, T. Guidi, K. C. Rule, M. B. Stone, and A. T. M. N. Islam, "Magnetic Soft Modes in the Distorted Triangular Antiferromagnet $\alpha - CaCr_2O_4$," *Phys. Rev. Lett.*, vol. 109, p. 127203, Sep 2012. [Online]. Available: https://link.aps.org/doi/10.1103/PhysRevLett.109.127203

[73] J. Ma, Y. Kamiya, T. Hong, H. B. Cao, G. Ehlers, W. Tian, C. D. Batista, Z. L. Dun, H. D. Zhou, and M. Matsuda, "Static and Dynamical Properties of the Spin-$1/2$ Equilateral Triangular-Lattice Antiferromagnet $Ba_3CoSb_2O_9$," *Phys. Rev. Lett.*, vol. 116, p. 087201, Feb 2016.

[74] S. Nakatsuji, Y. Nambu, H. Tonomura, O. Sakai, S. Jonas, C. Broholm, H. Tsunetsugu, Y. Qiu, and Y. Maeno, "Spin Disorder on a Triangular Lattice," *Science*, vol. 309, no. 5741, pp. 1697–1700, 2005.

[75] J. P. Sheckelton, J. R. Neilson, D. G. Soltan, and T. M. McQueen, "Possible valence-bond condensation in the frustrated cluster magnet $LiZn_2Mo_3O_8$," *Nature Materials*, vol. 11, no. 6, pp. 493–496, Jun 2012. [Online]. Available: http://dx.doi.org/10.1038/nmat3329

[76] B. Fåk, S. Bieri, E. Canévet, L. Messio, C. Payen, M. Viaud, C. Guillot-Deudon, C. Darie, J. Ollivier, and P. Mendels, "Evidence for a spinon Fermi surface in the triangular $S = 1$ quantum spin liquid $Ba_3NiSb_2O_9$," *Phys. Rev. B*, vol. 95, p. 060402, Feb 2017.

[77] T. Jolicoeur, E. Dagotto, E. Gagliano, and S. Bacci, "Ground-state properties of the S=1/2 Heisenberg antiferromagnet on a triangular lattice," *Phys. Rev. B*, vol. 42, pp. 4800–4803, Sep 1990. [Online]. Available: https://link.aps.org/doi/10.1103/PhysRevB.42.4800

[78] L. O. Manuel and H. A. Ceccatto, "Magnetic and quantum disordered

phases in triangular-lattice Heisenberg antiferromagnets," *Phys. Rev. B*, vol. 60, pp. 9489–9493, Oct 1999. [Online]. Available: https://link.aps.org/doi/10.1103/PhysRevB.60.9489

[79] Y. L. P. H, R. F. Bishop, and C. E. Campbell, "Quasiclassical magnetic order and its loss in a spin-1/2 Heisenberg antiferromagnet on a triangular lattice with competing bonds," *Phys. Rev. B*, vol. 91, no. 1, jan 2015. [Online]. Available: https://doi.org/10.1103%2Fphysrevb.91.014426

[80] Z. Zhu and S. R. White, "Spin liquid phase of the $S = \frac{1}{2}$ $J_1 - J_2$ Heisenberg model on the triangular lattice," *Phys. Rev. B*, vol. 92, p. 041105, Jul 2015. [Online]. Available: https://link.aps.org/doi/10.1103/PhysRevB.92.041105

[81] G. Misguich, C. Lhuillier, B. Bernu, and C. Waldtmann, "Spin-liquid phase of the multiple-spin exchange Hamiltonian on the triangular lattice," *Phys. Rev. B*, vol. 60, pp. 1064–1074, Jul 1999. [Online]. Available: https://link.aps.org/doi/10.1103/PhysRevB.60.1064

[82] R. V. Mishmash, J. R. Garrison, S. Bieri, and C. Xu, "Theory of a Competitive Spin Liquid State for Weak Mott Insulators on the Triangular Lattice," *Phys. Rev. Lett.*, vol. 111, p. 157203, Oct 2013.

[Online]. Available: https://link.aps.org/doi/10.1103/PhysRevLett.111.157203

[83] Y.-D. Li, Y.-M. Lu, and G. Chen, "The Spinon Fermi Surface U(1) Spin Liquid in a Spin-Orbit-Coupled Triangular Lattice Mott Insulator $YbMgGaO_4$," *Physical Review B*, vol. 96, no. 5, p. 054445, 2017.

[84] Y.-D. Li and G. Chen, "Detecting spin fractionalization in a spinon Fermi surface spin liquid," *Phys. Rev. B*, vol. 96, p. 075105, Aug 2017. [Online]. Available: https://link.aps.org/doi/10.1103/PhysRevB.96.075105

[85] T.-H. Han, J. S. Helton, S. Chu, D. G. Nocera, J. A. Rodriguez-Rivera, C. Broholm, and Y. S. Lee, "Fractionalized excitations in the spin-liquid state of a kagome-lattice antiferromagnet," *Nature*, vol. 492, no. 7429, pp. 406–410, Dec 2012.

[86] A. Zorko, S. Nellutla, J. van Tol, L. C. Brunel, F. Bert, F. Duc, J.-C. Trombe, M. A. de Vries, A. Harrison, and P. Mendels, "Dzyaloshinsky-Moriya Anisotropy in the Spin-1/2 Kagome Compound $ZnCu_3(OH)_6Cl_2$," *Phys. Rev. Lett.*, vol. 101, p. 026405, Jul 2008. [Online]. Available: https://link.aps.org/doi/10.1103/PhysRevLett.101.026405

[87] M. R. Norman, "Colloquium: Herbertsmithite and the search for the quantum spin liquid," *Rev. Mod. Phys.*, vol. 88, p. 041002, Dec

2016. [Online]. Available: https://link.aps.org/doi/10.1103/RevModPhys.88.041002

[88] C. Liu, R. Yu, and X. Wang, "Semiclassical ground-state phase diagram and multi-Q phase of a spin-orbit-coupled model on triangular lattice," *Phys. Rev. B*, vol. 94, p. 174424, Nov 2016. [Online]. Available: https://link.aps.org/doi/10.1103/PhysRevB.94.174424

[89] Q. Luo, S. Hu, B. Xi, J. Zhao, and X. Wang, "Ground-state phase diagram of an anisotropic spin-$\frac{1}{2}$ model on the triangular lattice," *Phys. Rev. B*, vol. 95, p. 165110, Apr 2017. [Online]. Available: https://link.aps.org/doi/10.1103/PhysRevB.95.165110

[90] K. A. Ross, L. Savary, B. D. Gaulin, and L. Balents, "Quantum Excitations in Quantum Spin Ice," *Phys. Rev. X*, vol. 1, p. 021002, Oct 2011. [Online]. Available: https://link.aps.org/doi/10.1103/PhysRevX.1.021002

[91] L. Pan, N. J. Laurita, K. A. Ross, B. D. Gaulin, and N. P. Armitage, "A measure of monopole inertia in the quantum spin ice $Yb_2Ti_2O_7$," *Nature Physics*, vol. 12, no. 4, pp. 361–366, dec 2015. [Online]. Available: https://doi.org/10.1038%2Fnphys3608

[92] Y. Li, D. Adroja, P. K. Biswas, P. J. Baker, Q. Zhang, J. Liu, A. A. Tsirlin, P. Gegenwart, and Q. Zhang, "Muon Spin Relaxation Evidence

for the U(1) Quantum Spin-Liquid Ground State in the Triangular Antiferromagnet $YbMgGaO_4$," *Physical Review Letters*, vol. 117, no. 9, aug 2016. [Online]. Available: https://doi.org/10.1103%2Fphysrevlett.117.097201

[93] Y. Xu, J. Zhang, Y. S. Li, Y. J. Yu, X. C. Hong, Q. M. Zhang, and S. Y. Li, "Absence of Magnetic Thermal Conductivity in the Quantum Spin-Liquid Candidate $YbMgGaO_4$," *Phys. Rev. Lett.*, vol. 117, p. 267202, Dec 2016. [Online]. Available: https://link.aps.org/doi/10.1103/PhysRevLett.117.267202

[94] Y. Li, D. Adroja, D. Voneshen, R. I. Bewley, Q. Zhang, A. A. Tsirlin, and P. Gegenwart, "Nearest-neighbour resonating valence bonds in $YbMgGaO_4$," *Nature Commun.*, vol. 8, p. 15814, Jun 2017. [Online]. Available: http://dx.doi.org/10.1038/ncomms15814

[95] Y. Li, D. Adroja, R. I. Bewley, D. Voneshen, A. A. Tsirlin, P. Gegenwart, and Q. Zhang, "Crystalline Electric-Field Randomness in the Triangular Lattice Spin-Liquid $YbMgGaO_4$," *Phys. Rev. Lett.*, vol. 118, p. 107202, Mar 2017. [Online]. Available: https://link.aps.org/doi/10.1103/PhysRevLett.118.107202

[96] S. Tóth, K. Rolfs, A. R. Wildes, and C. Rüegg, "Strong ex-

change anisotropy in $YbMgGaO_4$ from polarized neutron diffraction," *arXiv:1705.05699*, 2017.

[97] G. Ehlers, A. A. Podlesnyak, J. L. Niedziela, E. B. Iverson, and P. E. Sokol, "The new cold neutron chopper spectrometer at the Spallation Neutron Source: Design and performance," *Rev. Sci. Instrum.*, vol. 82, no. 8, p. 085108, 2011. [Online]. Available: http://dx.doi.org/10.1063/1.3626935

[98] N. P. Armitage, "Constraints on Jones transmission matrices from time-reversal invariance and discrete spatial symmetries," *Phys. Rev. B*, vol. 90, p. 035135, Jul 2014. [Online]. Available: https://link.aps.org/doi/10.1103/PhysRevB.90.035135

[99] X. Zhang, F. Mahmood, M. Daum, Z. Dun, J. A. M. Paddison, N. J. Laurita, T. Hong, H. Zhou, N. P. Armitage, and M. Mourigal, "Hierarchy of Exchange Interactions in the Triangular-Lattice Spin Liquid $YbMgGa_4$," *Phys. Rev. X*, vol. 8, p. 031001, Jul 2018. [Online]. Available: https://link.aps.org/doi/10.1103/PhysRevX.8.031001

[100] D. Huber, "Effect of the pseudodipolar interaction on critical spin dynamics in cubic ferromagnets," *Solid State Communications*, vol. 48, no. 9, pp. 831–833, dec 1983. [Online]. Available: https://doi.org/10.1016/0038-1098(83)91029-3

[101] J. H. van Vleck, "On the anisotropy of cubic ferromagnetic crystals," *Physical Review*, vol. 52, no. 11, pp. 1178–1198, dec 1937. [Online]. Available: https://doi.org/10.1103/physrev.52.1178

[102] R. Kubo and K. Tomita, "A general theory of magnetic resonance absorption," *J. Phys. Soc. Jpn.*, vol. 9, no. 6, pp. 888–919, 1954.

[103] T. G. Castner and M. S. Seehra, "Antisymmetric exchange and exchange-narrowed electron-paramagnetic-resonance linewidths," *Phys. Rev. B*, vol. 4, pp. 38–45, Jul 1971. [Online]. Available: https://link.aps.org/doi/10.1103/PhysRevB.4.38

[104] J. S. Gardner, M. J. P. Gingras, and J. E. Greedan, "Magnetic pyrochlore oxides," *Rev. Mod. Phys.*, vol. 82, pp. 53–107, Jan 2010. [Online]. Available: https://link.aps.org/doi/10.1103/RevModPhys.82.53

[105] D. J. P. Morris, D. Tennant, S. Grigera, B. Klemke, C. Castelnovo, R. Moessner, C. Czternasty, M. Meissner, K. Rule, J.-U. Hoffmann *et al.*, "Dirac strings and magnetic monopoles in the spin ice $Dy_2Ti_2O_7$," *Science*, vol. 326, no. 5951, pp. 411–414, 2009.

[106] A. Scheie, J. Kindervater, S. Säubert, C. Duvinage, C. Pfleiderer, H. J. Changlani, S. Zhang, L. Harriger, K. Arpino, S. M. Koohpayeh, O. Tchernyshyov, and C. Broholm, "Reentrant Phase Diagram of $Yb_2Ti_2O_7$ in a $<111>$ Magnetic Field," *Phys. Rev. Lett.*, vol. 119, p.

127201, Sep 2017. [Online]. Available: https://link.aps.org/doi/10.1103/PhysRevLett.119.127201

[107] J. Robert, E. Lhotel, G. Remenyi, S. Sahling, I. Mirebeau, C. Decorse, B. Canals, and S. Petit, "Spin dynamics in the presence of competing ferromagnetic and antiferromagnetic correlations in $Yb_2Ti_2O_7$," *Phys. Rev. B*, vol. 92, p. 064425, Aug 2015. [Online]. Available: https://link.aps.org/doi/10.1103/PhysRevB.92.064425

[108] K. Arpino, B. Trump, A. Scheie, T. McQueen, and S. Koohpayeh, "Impact of stoichiometry of $Yb_2Ti_2O_7$ on its physical properties," *Physical Review B*, vol. 95, no. 9, p. 094407, 2017.

[109] T. Fennell, M. Kenzelmann, B. Roessli, M. K. Haas, and R. J. Cava, "Power-Law Spin Correlations in the Pyrochlore Antiferromagnet $Tb_2Ti_2O_7$," *Phys. Rev. Lett.*, vol. 109, p. 017201, Jul 2012. [Online]. Available: https://link.aps.org/doi/10.1103/PhysRevLett.109.017201

[110] J. Zhang, K. Fritsch, Z. Hao, B. V. Bagheri, M. J. P. Gingras, G. E. Granroth, P. Jiramongkolchai, R. J. Cava, and B. D. Gaulin, "Neutron spectroscopic study of crystal field excitations in $Tb_2Ti_2O_7$ and $Tb_2Sn_2O_7$," *Phys. Rev. B*, vol. 89, p. 134410, Apr 2014. [Online]. Available: https://link.aps.org/doi/10.1103/PhysRevB.89.134410

[111] A. J. Princep, H. C. Walker, D. T. Adroja, D. Prabhakaran, and

A. T. Boothroyd, “Crystal field states of Tb^{3+} in the pyrochlore spin liquid $Tb_2Ti_2O_7$ from neutron spectroscopy,” *Phys. Rev. B*, vol. 91, p. 224430, Jun 2015. [Online]. Available: https://link.aps.org/doi/10.1103/PhysRevB.91.224430

[112] T. T. A. Lummen, I. P. Handayani, M. C. Donker, D. Fausti, G. Dhalenne, P. Berthet, A. Revcolevschi, and P. H. M. van Loosdrecht, “Phonon and crystal field excitations in geometrically frustrated rare earth titanates,” *Phys. Rev. B*, vol. 77, p. 214310, Jun 2008. [Online]. Available: https://link.aps.org/doi/10.1103/PhysRevB.77.214310

[113] H. R. Molavian, M. J. P. Gingras, and B. Canals, “Dynamically Induced Frustration as a Route to a Quantum Spin Ice State in $Tb_2Ti_2O_7$ via Virtual Crystal Field Excitations and Quantum Many-Body Effects,” *Phys. Rev. Lett.*, vol. 98, p. 157204, Apr 2007. [Online]. Available: https://link.aps.org/doi/10.1103/PhysRevLett.98.157204

[114] C. Liu, F.-Y. Li, and G. Chen, “Upper branch magnetism in quantum magnets: Collapses of excited levels and emergent selection rules,” *Phys. Rev. B*, vol. 99, p. 224407, Jun 2019. [Online]. Available: https://link.aps.org/doi/10.1103/PhysRevB.99.224407

[115] B. D. Gaulin, J. S. Gardner, P. A. McClarty, and M. J. P. Gingras, “Lack of evidence for a singlet crystal-field ground state in the magnetic

pyrochlore $Tb_2Ti_2O_7$," *Phys. Rev. B*, vol. 84, p. 140402, Oct 2011. [Online]. Available: https://link.aps.org/doi/10.1103/PhysRevB.84.140402

[116] P. Bonville, I. Mirebeau, A. Gukasov, S. Petit, and J. Robert, "Tetragonal distortion yielding a two-singlet spin liquid in pyrochlore $Tb_2Ti_2O_7$," *Phys. Rev. B*, vol. 84, p. 184409, Nov 2011. [Online]. Available: https://link.aps.org/doi/10.1103/PhysRevB.84.184409

[117] S. H. Curnoe, "Structural distortion and the spin liquid state in $Tb_2Ti_2O_7$," *Phys. Rev. B*, vol. 78, p. 094418, Sep 2008. [Online]. Available: https://link.aps.org/doi/10.1103/PhysRevB.78.094418

[118] K. Rule and P. Bonville, "Tetragonal distortion in $Tb_2Ti_2O_7$ seen by neutron scattering," in *Journal of Physics: Conference Series*, vol. 145, no. 1. IOP Publishing, 2009, p. 012027.

[119] E. Constable, R. Ballou, J. Robert, C. Decorse, J.-B. Brubach, P. Roy, E. Lhotel, L. Del-Rey, V. Simonet, S. Petit *et al.*, "Double vibronic process in the quantum spin ice candidate $Tb_2Ti_2O_7$ revealed by terahertz spectroscopy," *Physical Review B*, vol. 95, no. 2, p. 020415, 2017.

[120] M. Ruminy, S. Guitteny, J. Robert, L.-P. Regnault, M. Boehm, P. Steffens, H. Mutka, J. Ollivier, U. Stuhr, J. S. White, B. Roessli, L. Bovo, C. Decorse, M. K. Haas, R. J. Cava, I. Mirebeau, M. Kenzelmann, S. Petit, and T. Fennell, "Magnetoelastic excitation spectrum in the rare-earth

pyrochlore $Tb_2Ti_2O_7$," *Phys. Rev. B*, vol. 99, p. 224431, Jun 2019. [Online]. Available: https://link.aps.org/doi/10.1103/PhysRevB.99.224431

[121] K. Amelin, Y. Alexanian, U. Nagel, T. Rõ om, J. Robert, J. Debray, V. Simonet, C. Decorse, Z. Wang, R. Ballou, E. Constable, and S. de Brion, "Terahertz magneto-optical investigation of quadrupolar spin-lattice effects in magnetically frustrated $Tb_2Ti_2O_7$," *Phys. Rev. B*, vol. 102, p. 134428, Oct 2020. [Online]. Available: https://link.aps.org/doi/10.1103/PhysRevB.102.134428

[122] P. Bonville, A. Gukasov, I. Mirebeau, and S. Petit, "Towards a model of a dynamical Jahn-Teller coupling at very low temperatures in $Tb_2Ti_2O_7$," *Phys. Rev. B*, vol. 89, p. 085115, Feb 2014. [Online]. Available: https://link.aps.org/doi/10.1103/PhysRevB.89.085115

[123] F. S. Ham, "Dynamical Jahn-Teller Effect in Paramagnetic Resonance Spectra: Orbital Reduction Factors and Partial Quenching of Spin-Orbit Interaction," *Phys. Rev.*, vol. 138, pp. A1727–A1740, Jun 1965. [Online]. Available: https://link.aps.org/doi/10.1103/PhysRev.138.A1727

[124] S.-H. Do, S.-Y. Park, J. Yoshitake, J. Nasu, Y. Motome, Y. S. Kwon, D. Adroja, D. Voneshen, K. Kim, T.-H. Jang *et al.*, "Majorana fermions in the Kitaev quantum spin system α-$RuCl_3$," *Nature Physics*, vol. 13, no. 11, pp. 1079–1084, 2017.

[125] S. Choi, R. Coldea, A. Kolmogorov, T. Lancaster, I. Mazin, S. Blundell, P. Radaelli, Y. Singh, P. Gegenwart, K. Choi *et al.*, "Spin waves and revised crystal structure of honeycomb iridate Na_2IrO_3," *Physical review letters*, vol. 108, no. 12, p. 127204, 2012.

[126] S. H. Chun, J.-W. Kim, J. Kim, H. Zheng, C. C. Stoumpos, C. Malliakas, J. Mitchell, K. Mehlawat, Y. Singh, Y. Choi *et al.*, "Direct evidence for dominant bond-directional interactions in a honeycomb lattice iridate $Na_2IrO_3$3," *Nature Physics*, vol. 11, no. 6, pp. 462–466, 2015.

[127] Y. Kasahara, T. Ohnishi, Y. Mizukami, O. Tanaka, S. Ma, K. Sugii, N. Kurita, H. Tanaka, J. Nasu, Y. Motome *et al.*, "Majorana quantization and half-integer thermal quantum Hall effect in a Kitaev spin liquid," *Nature*, vol. 559, no. 7713, pp. 227–231, 2018.

[128] J. Zheng, K. Ran, T. Li, J. Wang, P. Wang, B. Liu, Z.-X. Liu, B. Normand, J. Wen, and W. Yu, "Gapless Spin Excitations in the Field-Induced Quantum Spin Liquid Phase of $\alpha-\mathrm{RuCl_3}$," *Phys. Rev. Lett.*, vol. 119, p. 227208, Dec 2017. [Online]. Available: https://link.aps.org/doi/10.1103/PhysRevLett.119.227208

[129] A. Banerjee, P. Lampen-Kelley, J. Knolle, C. Balz, A. A. Aczel, B. Winn, Y. Liu, D. Pajerowski, J. Yan, C. A. Bridges *et al.*, "Excitations in the field-

induced quantum spin liquid state of α-$RuCl_3$," *npj Quantum Materials*, vol. 3, no. 1, pp. 1–7, 2018.

[130] A. Little, L. Wu, P. Lampen-Kelley, A. Banerjee, S. Patankar, D. Rees, C. A. Bridges, J.-Q. Yan, D. Mandrus, S. E. Nagler, and J. Orenstein, "Antiferromagnetic Resonance and Terahertz Continuum in α-$RuCl_3$," *Phys. Rev. Lett.*, vol. 119, p. 227201, Nov 2017. [Online]. Available: https://link.aps.org/doi/10.1103/PhysRevLett.119.227201

[131] D. Wulferding, Y. Choi, S.-H. Do, C. H. Lee, P. Lemmens, C. Faugeras, Y. Gallais, and K.-Y. Choi, "Magnon bound states versus anyonic Majorana excitations in the Kitaev honeycomb magnet α-$RuCl_3$," *Nature communications*, vol. 11, no. 1, pp. 1–7, 2020.

[132] A. Ponomaryov, L. Zviagina, J. Wosnitza, P. Lampen-Kelley, A. Banerjee, J.-Q. Yan, C. Bridges, D. Mandrus, S. Nagler, and S. Zvyagin, "Nature of Magnetic Excitations in the High-Field Phase of α-$RuCl_3$," *Physical Review Letters*, vol. 125, no. 3, p. 037202, 2020.

[133] L. Wu, A. Little, E. E. Aldape, D. Rees, E. Thewalt, P. Lampen-Kelley, A. Banerjee, C. A. Bridges, J.-Q. Yan, D. Boone, S. Patankar, D. Goldhaber-Gordon, D. Mandrus, S. E. Nagler, E. Altman, and J. Orenstein, "Field evolution of magnons in $\alpha-\mathrm{RuCl_3}$ by high-resolution polarized terahertz spectroscopy," *Phys. Rev. B*, vol. 98, p. 094425, Sep

2018. [Online]. Available: https://link.aps.org/doi/10.1103/PhysRevB.98.094425

[134] "Kitaev-Heisenberg Hamiltonian for high-spin d^7 Mott insulators, author=Sano, Ryoya and Kato, Yasuyuki and Motome, Yukitoshi," *Physical Review B*, vol. 97, no. 1, p. 014408, 2018.

[135] H. Liu and G. Khaliullin, "Pseudospin exchange interactions in d^7 cobalt compounds: Possible realization of the Kitaev model," *Physical Review B*, vol. 97, no. 1, p. 014407, 2018.

[136] L. Regnault, P. Burlet, and J. Rossat-Mignod, "Magnetic ordering in a planar X-Y model: $BaCo_2(AsO_4)_2$," *Physica B+ C*, vol. 86, pp. 660–662, 1977.

[137] L.-P. Regnault, C. Boullier, and J. Lorenzo, "Polarized-neutron investigation of magnetic ordering and spin dynamics in $BaCo_2(AsO_4)_2$ frustrated honeycomb-lattice magnet," *Heliyon*, vol. 4, no. 1, p. e00507, 2018.

[138] L. Regnault and J. Rossat-Mignod, "Effect of a magnetic field on the magnetic ordering of $BaCo_2(AsO_4)_2$," *Journal of Magnetism and Magnetic Materials*, vol. 14, no. 2-3, pp. 194–196, 1979.

[139] J. Yoshitake, J. Nasu, and Y. Motome, "Fractional spin fluctuations as a precursor of quantum spin liquids: Majorana dynamical mean-field

study for the Kitaev model," *Physical review letters*, vol. 117, no. 15, p. 157203, 2016.

[140] J. Knolle, D. Kovrizhin, J. Chalker, and R. Moessner, "Dynamics of a two-dimensional quantum spin liquid: Signatures of emergent Majorana fermions and fluxes," *Physical Review Letters*, vol. 112, no. 20, p. 207203, 2014.

[141] S. M. Winter, K. Riedl, D. Kaib, R. Coldea, and R. Valentí, "Probing α-$RuCl_3$ Beyond Magnetic Order: Effects of Temperature and Magnetic Field," *Physical review letters*, vol. 120, no. 7, p. 077203, 2018.

[142] N. Janša, A. Zorko, M. Gomilšek, M. Pregelj, K. W. Krämer, D. Biner, A. Biffin, C. Rüegg, and M. Klanjšek, "Observation of two types of fractional excitation in the Kitaev honeycomb magnet," *Nature physics*, vol. 14, no. 8, pp. 786–790, 2018.

[143] R. Applegate, N. Hayre, R. Singh, T. Lin, A. Day, and M. Gingras, "Vindication of $Yb_2Ti_2O_7$ as a model exchange quantum spin ice," *Physical review letters*, vol. 109, no. 9, p. 097205, 2012.

[144] Y. Wan and O. Tchernyshyov, "Quantum strings in quantum spin ice," *Physical review letters*, vol. 108, no. 24, p. 247210, 2012.

[145] Y. Tokiwa, T. Yamashita, M. Udagawa, S. Kittaka, T. Sakakibara, D. Ter-

azawa, Y. Shimoyama, T. Terashima, Y. Yasui, T. Shibauchi *et al.*, "Possible observation of highly itinerant quantum magnetic monopoles in the frustrated pyrochlore $Yb_2Ti_2O_7$," *Nature communications*, vol. 7, p. 10807, 2016.

[146] A. Yaouanc, P. D. de Réotier, L. Keller, B. Roessli, and A. Forget, "A novel type of splayed ferromagnetic order observed in $Yb_2Ti_2O_7$," *Journal of Physics: Condensed Matter*, vol. 28, no. 42, p. 426002, 2016.

[147] H. Yan, O. Benton, L. Jaubert, and N. Shannon, "Theory of multiple-phase competition in pyrochlore magnets with anisotropic exchange with application to $Yb_2Ti_2O_7$, $Er_2Ti_2O_7$, and $Er_2Sn_2O_7$," *Phys. Rev. B*, vol. 95, p. 094422, Mar 2017. [Online]. Available: https://link.aps.org/doi/10.1103/PhysRevB.95.094422

[148] L.-J. Chang, S. Onoda, Y. Su, Y.-J. Kao, K.-D. Tsuei, Y. Yasui, K. Kakurai, and M. R. Lees, "Higgs transition from a magnetic Coulomb liquid to a ferromagnet in $Yb_2Ti_2O_7$," *Nature communications*, vol. 3, p. 992, 2012.

[149] J. Gaudet, K. Ross, E. Kermarrec, N. P. Butch, G. Ehlers, H. Dabkowska, and B. Gaulin, "Gapless quantum excitations from an icelike splayed ferromagnetic ground state in stoichiometric $Yb_2Ti_2O_7$," *Physical Review B*, vol. 93, no. 6, p. 064406, 2016.

[150] J. A. Hodges, P. Bonville, A. Forget, A. Yaouanc, P. Dalmas de

Réotier, G. André, M. Rams, K. Królas, C. Ritter, P. C. M. Gubbens, C. T. Kaiser, P. J. C. King, and C. Baines, "First-Order Transition in the Spin Dynamics of Geometrically Frustrated $Yb_2Ti_2O_7$," *Phys. Rev. Lett.*, vol. 88, p. 077204, Feb 2002. [Online]. Available: https://link.aps.org/doi/10.1103/PhysRevLett.88.077204

[151] K. Ross, L. Yaraskavitch, M. Laver, J. S. Gardner, J. Quilliam, S. Meng, J. Kycia, D. Singh, T. Proffen, H. Dabkowska *et al.*, "Dimensional evolution of spin correlations in the magnetic pyrochlore $Yb_2Ti_2O_7$," *Physical Review B*, vol. 84, no. 17, p. 174442, 2011.

[152] K. Ross, J. Ruff, C. Adams, J. Gardner, H. Dabkowska, Y. Qiu, J. Copley, and B. Gaulin, "Two-Dimensional Kagome Correlations and Field Induced Order in the Ferromagnetic X-Y Pyrochlore $Yb_2Ti_2O_7$," *Physical review letters*, vol. 103, no. 22, p. 227202, 2009.

[153] J. D. Thompson, P. A. McClarty, H. M. Rønnow, L. P. Regnault, A. Sorge, and M. J. P. Gingras, "Rods of Neutron Scattering Intensity in $Yb_2Ti_2O_7$: Compelling Evidence for Significant Anisotropic Exchange in a Magnetic Pyrochlore Oxide," *Phys. Rev. Lett.*, vol. 106, p. 187202, May 2011. [Online]. Available: https://link.aps.org/doi/10.1103/PhysRevLett.106.187202

[154] R. M. D'Ortenzio, H. A. Dabkowska, S. R. Dunsiger, B. D. Gaulin,

M. J. P. Gingras, T. Goko, J. B. Kycia, L. Liu, T. Medina, T. J. Munsie, D. Pomaranski, K. A. Ross, Y. J. Uemura, T. J. Williams, and G. M. Luke, "Unconventional magnetic ground state in $Yb_2Ti_2O_7$," *Phys. Rev. B*, vol. 88, p. 134428, Oct 2013. [Online]. Available: https://link.aps.org/doi/10.1103/PhysRevB.88.134428

[155] J. S. Gardner, G. Ehlers, N. Rosov, R. W. Erwin, and C. Petrovic, "Spin-spin correlations in $Yb_2Ti_2O_7$: A polarized neutron scattering study," *Phys. Rev. B*, vol. 70, p. 180404, Nov 2004. [Online]. Available: https://link.aps.org/doi/10.1103/PhysRevB.70.180404

[156] V. Pe çanha Antonio, E. Feng, Y. Su, V. Pomjakushin, F. Demmel, L.-J. Chang, R. J. Aldus, Y. Xiao, M. R. Lees, and T. Brückel, "Magnetic excitations in the ground state of $Yb_2Ti_2O_7$," *Phys. Rev. B*, vol. 96, p. 214415, Dec 2017. [Online]. Available: https://link.aps.org/doi/10.1103/PhysRevB.96.214415

[157] L. D. Landau, "The therory of a fermi liquid," *J. Exp. Theor. Phys*, vol. 3, p. 920, 1957.

[158] L. D. Landau, "One the therory of the fermi liquid," *J. Exp. Theor. Phys*, vol. 8, p. 70, 1959.

[159] A. Damascelli, Z. Hussain, and Z.-X. Shen, "Angle-resolved photoemission studies of the cuprate superconductors," *Rev. Mod.*

Phys., vol. 75, pp. 473–541, Apr 2003. [Online]. Available: https://link.aps.org/doi/10.1103/RevModPhys.75.473

[160] S. Sachdev, "Quantum Phase Transitions," 2000. [Online]. Available: https://doi.org/10.1017/cbo9780511622540

[161] P. Pfeuty, "The one-dimensional Ising model with a transverse field," *ANNALS of Physics*, vol. 57, no. 1, pp. 79–90, 1970.

[162] M. E. Zhitomirsky and A. L. Chernyshev, "Colloquium: Spontaneous magnon decays," *Rev. Mod. Phys.*, vol. 85, pp. 219–242, Jan 2013. [Online]. Available: https://link.aps.org/doi/10.1103/RevModPhys.85.219

[163] S. R. White and A. L. Chernyshev, "Neél Order in Square and Triangular Lattice Heisenberg Models," *Phys. Rev. Lett.*, vol. 99, p. 127004, Sep 2007. [Online]. Available: https://link.aps.org/doi/10.1103/PhysRevLett.99.127004

[164] A. L. Chernyshev and M. E. Zhitomirsky, "Spin waves in a triangular lattice antiferromagnet: Decays, spectrum renormalization, and singularities," *Phys. Rev. B*, vol. 79, p. 144416, Apr 2009. [Online]. Available: https://link.aps.org/doi/10.1103/PhysRevB.79.144416

[165] A. L. Chernyshev and M. E. Zhitomirsky, "Magnon Decay in Noncollinear Quantum Antiferromagnets," *Phys. Rev. Lett.*, vol. 97, p.

207202, Nov 2006. [Online]. Available: https://link.aps.org/doi/10.1103/PhysRevLett.97.207202

[166] M. Mourigal, M. E. Zhitomirsky, and A. L. Chernyshev, "Field-induced decay dynamics in square-lattice antiferromagnets," *Phys. Rev. B*, vol. 82, p. 144402, Oct 2010. [Online]. Available: https://link.aps.org/doi/10.1103/PhysRevB.82.144402

[167] W. T. Fuhrman, M. Mourigal, M. E. Zhitomirsky, and A. L. Chernyshev, "Dynamical structure factor of quasi-two-dimensional antiferromagnet in high fields," *Phys. Rev. B*, vol. 85, p. 184405, May 2012. [Online]. Available: https://link.aps.org/doi/10.1103/PhysRevB.85.184405

[168] M. Mourigal, W. T. Fuhrman, A. L. Chernyshev, and M. E. Zhitomirsky, "Dynamical structure factor of the triangular-lattice antiferromagnet," *Phys. Rev. B*, vol. 88, p. 094407, Sep 2013. [Online]. Available: https://link.aps.org/doi/10.1103/PhysRevB.88.094407

[169] P. Coleman, *Introduction to many-body physics*. Cambridge University Press, 2015.

[170] K. Ross, T. Proffen, H. Dabkowska, J. Quilliam, L. Yaraskavitch, J. Kycia, and B. Gaulin, "Lightly stuffed pyrochlore structure of single-crystalline $Yb_2Ti_2O_7$ grown by the optical floating zone technique," *Physical Review B*, vol. 86, no. 17, p. 174424, 2012.

[171] A. Yaouanc, P. D. de Réotier, C. Marin, and V. Glazkov, "Single-crystal versus polycrystalline samples of magnetically frustrated $Yb_2Ti_2O_7$: specific heat results," *Physical Review B*, vol. 84, no. 17, p. 172408, 2011.

[172] Z. Shafieizadeh, Y. Xin, S. M. Koohpayeh, Q. Huang, and H. Zhou, "Superdislocations and point defects in pyrochlore $Yb_2Ti_2O_7$ single crystals and implication on magnetic ground states," *Scientific reports*, vol. 8, no. 1, p. 17202, 2018.

[173] D.-X. Chen, E. Pardo, and A. Sanchez, "Demagnetizing factors of rectangular prisms and ellipsoids," *IEEE Transactions on Magnetics*, vol. 38, no. 4, pp. 1742–1752, 2002.

[174] D.-X. Chen, J. A. Brug, and R. B. Goldfarb, "Demagnetizing factors for cylinders," *IEEE Transactions on magnetics*, vol. 27, no. 4, pp. 3601–3619, 1991.

[175] A. Aharoni, "Demagnetizing factors for rectangular ferromagnetic prisms," *Journal of applied physics*, vol. 83, no. 6, pp. 3432–3434, 1998.

[176] A. Kuzmenko, "Kramers-Kronig constrained variational analysis of optical spectra," *Review of scientific instruments*, vol. 76, no. 8, p. 083108, 2005.

Vita

Xinshu Zhang was born in Shenyang, China. He attended Nanjing University and received a B.S. degree from department of Physics in 2015. He enrolled in the physics Ph.D. program at Johns Hopkins University where his research focused on the low energy magneto-optics of frustrated magnetism by time-domain terahertz spectroscopy. He has published multiple papers in peer-reviewed journals, including: Physical Review X and Nano Letters. Beginning in May of 2021, Xinshu will be joining Anshul Kogar's group at University of California, Los Angeles as a postdoctoral fellow.